

Rockefeller University

Digital Commons @ RU

---

Student Theses and Dissertations

---

2020

## Genetic Functional Dissection of the Synaptic Output of a Dual-Function Integrating Neuron

Ayless Sordillo

Follow this and additional works at: [https://digitalcommons.rockefeller.edu/student\\_theses\\_and\\_dissertations](https://digitalcommons.rockefeller.edu/student_theses_and_dissertations)



Part of the Life Sciences Commons

---



GENETIC AND FUNCTIONAL DISSECTION OF THE SYNAPTIC OUTPUT OF A  
DUAL-FUNCTION INTEGRATING NEURON

A Thesis Presented to the Faculty of  
The Rockefeller University  
in Partial Fulfillment of the Requirements for  
the degree of Doctor of Philosophy

by  
Aylesse Sordillo  
June 2020



# GENETIC AND FUNCTIONAL DISSECTION OF THE SYNAPTIC OUTPUT OF A DUAL-FUNCTION INTEGRATING NEURON

Ayellese Sordillo, Ph.D.  
The Rockefeller University 2020

Animals must vary their behavior in response to changes in their environment, but behavior also remains consistent over time. This thesis focuses on a single interneuron, RIM, and a single behavior, the reversal, to better understand how the circuits driving motor outputs accomplish the seemingly contradictory tasks of generating appropriate and variable behaviors.

In the compact and well-defined nervous system of *C. elegans*, the interneuron RIM is an important part of the reversal behavior circuit that contributes to sensory integration, behavioral variability, generation of behavioral states, and learning. RIM releases both glutamate and the biogenic amine tyramine (~noradrenaline) and forms gap junctions with neurons that govern various aspects of *C. elegans* locomotion.

RIM is the major source of tyramine in *C. elegans*, and this output is known to extend reversal length of spontaneous and evoked reversals and to sharpen turns during escape response. However, the roles of RIM glutamate and RIM gap junctions in organizing reversal behavior have remained nebulous.

I combine cell-specific genetic manipulations, behavioral analyses, and both manipulations and observations of neural activity to dissect the diverse synaptic outputs of the interneuron RIM. I reveal a role for RIM glutamate in spontaneous reversal behavior and show that RIM glutamate and RIM tyramine differentially regulate spontaneous reversals. Through comparative analysis of the exo- and endocytosis dynamics of RIM glutamate and tyramine, I provide evidence that they are released from RIM under the same conditions and with similar dynamics, and that tyramine may also be released from a distinct, slower vesicle class.

I also find that both RIM chemical synapses and electrical synapses are bidirectional regulators of *C. elegans* locomotion, stabilizing both the forward state and reversal state. I conclude that RIM is a dual-function neuron, able to both promote and inhibit reversal behavior.



*For my parents, to whom I will never be able to express the extent of my love and appreciation. Thank you for your ceaseless love, support, and acceptance.*

## ACKNOWLEDGMENTS

Thank you to my advisor and mentor, Cori Bargmann. This thesis would not exist without your remarkable insight and guidance but writing this thesis at the time I did I have to say it was truly a labor of love. Thank you for your kindness and support over the past few months and the past seven years.

Thank you to everyone in Bargmann Lab, past and present, for filling my time at Rockefeller with such joy and laughter and for always being so generous with your time when I needed help. I would especially like to thank past lab members Donovan Ventimiglia, Andrew Gordus, and Navin Pokala for the incredible work on which this thesis was built and for answering my many questions over the years. Thanks to Alejandro López for the amazing collaboration that led to some of my best results. There's no one I would rather CRISPR with. Thanks to Phil Kidd for all of the technical and coding support, particularly for all the circuit-building and trouble-shooting and for being my oldest friend at the Rock. Thanks to Elias Scheer for being so generous with your code, your behavioral set up, and your time, and for driving through the mountains of Puerto Rico. Thank you Priscilla, Hernán, and Manoush for always keeping everything in lab running smoothly. I could not have done this without you. To Javier and Phil, thanks for helping out in the lab while I ducked out to write.

Thank you to Ana Domingos and Jeffrey Friedman for introducing me to Rockefeller, for your great mentorship, and for helping me stay here for my PhD. Thanks to all my old Friedman Lab labmates for showing me that scientists know how to have fun!

I'd also like to thank my committee members Leslie Vosshall and Vanessa Ruta for all of the intellectual and professional guidance over the years. Your critiques and encouragements have pushed me to grow as a scientist and as a person.

To Jeremy Dittman, thanks for agreeing to be my external examiner, for always being a joy to run into at a conference or after a talk, and for the great feedback on this thesis.

Thanks to everyone in the Dean's Office for making my PhD easier and for being so kind! Special thanks to Cris for your help and support during the quarantine.

Thanks to my dear friends and family near and far who have been there for me over the past years and supported me over the last months. I love you all.

Lastly, thank you to Catherine O'Keeffe for being my light in a crisis and for all of your help and love. You're too good to me.

## TABLE OF CONTENTS

<b>CHAPTER 1: Introduction</b> .....	1
Thesis Overview.....	14
<b><u>PART I</u></b>	
<b>CHAPTER 2: Co-transmitted neurotransmitters separately modulate reversals</b> ...	16
Introduction.....	16
Results.....	20
Discussion.....	40
Future Directions.....	42
<b>CHAPTER 3: RIM gap junctions are bidirectional regulators of reversal frequency</b> .....	44
Introduction.....	44
Results.....	46
Discussion.....	72
Future Directions.....	75
<b><u>PART II</u></b>	
<b>CHAPTER 4: Comparative analysis of RIM glutamate and RIM tyramine exocytosis and endocytosis dynamics in intact <i>C. elegans</i></b> .....	79
Introduction.....	79
Results.....	81
Discussion.....	96
Future Directions.....	97
<b>CHAPTER 5: Perspectives</b> .....	98

<b>METHODS.....</b>	<b>100</b>
<b>APPENDIX A: Effects of RIM chemical synapses during on-food foraging.....</b>	<b>105</b>
<b>REFERENCES.....</b>	<b>113</b>

## LIST OF FIGURES

### CHAPTER 1

Figure 1-1. The synaptic partners of RIM.....4

### CHAPTER 2

Figure 2-1. A CRISPR-Cas9 generated, cell-specific glutamate knockout enables the elucidation of the role of RIM glutamate on reversal behavior.....18

Figure 2-2. RIM glutamate and tyramine do not affect the local search - global search transition or reversal frequency during global search.....21

Figure 2-3. RIM glutamate decreases reversal frequency during off-food foraging; tyramine decreases reversal frequency in parallel by increasing reversal length and speed.....23

Figure 2-4. Edited *eat-4* locus, nFLP expression, or co-injection marker alone do not account for changes in behavior in a RIM-specific glutamate knockout. Supplement to Figure 2-2.....25

Figure 2-5. Octopamine deficient *tbh-1* mutants exhibit normal reversal behavior during off-food foraging.....28

Figure 2-6. Expressing Tetanus toxin in RIM causes defects similar to the combined RIM glutamate KO; *tdc-1* mutant. ....30

Figure 2-7. RIM chemical synapses increase forward and reverse speed.....32

Figure 2-8. RIM tyramine promotes long reversals coupled to omega turns; RIM glutamate inhibits coupling to omega turns.....34

Figure 2-9. Effects of RIM chemical synapses on reversal omegas at various reversal lengths. Supplement to Figure 2-8.....36

Figure 2-10. RIM chemical synapses do not shape uncoupled, short reversals.....39

Figure 2-11. Effects of RIM chemical synapses on reversal behavior.....41

### CHAPTER 3

Figure 3-1. Direct stimulation of RIM evokes reversals throughout the light pulse across off-food foraging states regardless of pulse time.....	47
Figure 3-2. Long reversal omegas are evoked upon RIM activation. Supplement to Figures 3-1 & 3-3.....	50
Figure 3-3. RIM stimulation evokes long reversals of characteristic duration, followed by coupled omega turns.....	51
Figure 3-4. Effects of stimulus strength and behavioral state on optogenetically-induced reversals.....	55
Figure 3-5. Effects of stimulus strength and behavioral state on optogenetically-induced reversal omegas. Supplement to Figure 3-4.....	57
Figure 3-6. RIM chemical synapses do not inhibit RIM-evoked reversals during off-food foraging but do increase their length and speed.....	60
Figure 3-7. RIM chemical synapses do not affect the fraction of RIM-evoked long reversal omegas during off-food foraging. Supplement to Figure 3-6.....	62
Figure 3-8. RIM gap junctions decrease spontaneous reversal frequency during local search.....	65
Figure 3-9. RIM gap junctions do not affect the local search - global search transition but moderately inhibit reversal frequency during global search.....	67
Figure 3-10. RIM gap junctions support optogenetically-evoked reversals during global search.....	69
Figure 3-11. RIM gap junctions do not affect optogenetically-evoked long reversal omegas. Supplement to Figure 3-10.....	70
Figure 3-12. Effects of RIM chemical synapses and gap junctions on reversal behavior..	73
Figure 3-13. Locations of relevant RIM chemical synapses and RIM gap junctions.....	78

## CHAPTER 4

Figure 4-1. Vesicular transporter-pHluorin fusions fluoresce upon exposure to the extracellular space.....	80
Figure 4-2. RIM::VGLUT-pH and RIM::VMAT-pH exhibit spontaneous fluorescence changes, inferred to be exo- and endocytosis events, in immobilized animals .....	83
Figure 4-3. Reversal behavior is unaltered in RIM::VGLUT-pH and RIM::VMAT-pH animals. Supplement to Figure 4-2.....	85
Figure 4-4. RIM pHluorin dynamics reflect RIM axonal calcium dynamics. Supplement to Figure 4-2, Figure 4-7, & Figure 4-10.....	87
Figure 4-5. Representative inferred exocytosis events extracted from spontaneous pHluorin dynamics. Supplement to Figure 4-2 and Figure 4-7.....	89
Figure 4-6. Representative inferred exocytosis events fitted to single and double exponentials. Supplement to Figure 4-7.....	90
Figure 4-7. VGLUT-pH and VMAT-pH may share fast exocytosis dynamics but may differ in a class of slower exocytosis events.....	91
Figure 4-8. Representative inferred endocytosis events extracted from spontaneous pHluorin dynamics. Supplement to Figure 4-2 and 4-10.....	93
Figure 4-9. Representative inferred endocytosis events fitted to single and double exponentials. Supplement to Figure 4-7.....	94
Figure 4-10. VGLUT-pH and VMAT-pH may share endocytosis dynamics.....	95
<b>APPENDIX</b>	
Figure A-1. RIM chemical outputs may modulate on-food foraging states and reversals.....	106

**LIST OF TABLES**

Table 3-1. Quantification of evoked reversal omega parameters: All Tracks.....53

APPENDIX B. n of distributions and scatter plots.....109

APPENDIX C. p-Values of statistically significant data.....110

APPENDIX D. List of Strains.....112



## CHAPTER 1: Introduction

In order for organisms to survive in an unpredictable world, behavior must be both pliable and stable over time. What are the sources of behavioral variation, and how do nervous systems simultaneously maintain variable and cohesive motor outputs? Variation in behavior can be a consequence of random noise (Faisal et al., 2008). Considering a behavioral response to an external stimulus, noise can influence the ultimate motor output at any step from perception to behavior. Noise exists in the environment, at the level of sensory perception, at the level of cells and synapses, and at the level of biochemicals and electrical impulses. Motor noise is created as electrical signals are converted into mechanical force to generate behavioral output. Despite this, not all variation in behavior is explained by randomness; it can be deterministic. Behavior varies with fluctuations in the environment and with internal states, such as behavioral states and network states. While these influences are not random, they can be difficult to delineate and observe, particularly those that are internally generated. The mechanisms by which organisms integrate external and internal state to generate behavioral variation are poorly understood.

Though it may be challenging to pin down sources of variation, variability can be beneficial—even necessary—to perfecting a motor output. Variation during learning is thought to allow an organism to explore a range of motor outputs and select those that are optimal. In songbirds, a subregion of the basal ganglia is required for behavioral variability during learning, and lesioning this region disrupts the ability of juvenile songbirds to properly learn a song from their tutor (Ölveczky et al., 2005). In humans, increased behavioral variability associated with a drawing task correlates with faster learning of the task (Wu et al., 2014).

### Deterministic sources of behavioral variation

Organisms need to respond appropriately to external stimuli, but how variations in stimuli lead to behavioral tuning is unclear. Recent work has shown that particular populations of integrating neurons can generate different behaviors depending on their degree of activity. Vertebrates integrate cues pertaining to mating and aggression in the hypothalamus. Male mice exhibit scalable motor outputs with increasing stimuli to estrogen-receptor positive neurons in this region (Lee et al., 2014). Low levels of optogenetic activation of these neurons lead to mating behaviors, namely investigation of conspecifics and mounting. High levels of optogenetic activation of the same population leads to aggression and attack. In *Drosophila melanogaster*, P1 neurons control courtship behavior. A subpopulation of P1 neurons has been found to also control aggression in males, inducing lunging, an aggressive behavior, upon low optogenetic stimulation and wing extension, a courtship behavior, upon high stimulation (Hoopfer et al., 2015). Robust induction of lunging behavior by low optogenetic stimulation requires olfactory cues from conspecific males, indicating that the behavior is influenced by sensory context. Additionally, flies enter a persistent aggressive state at

the offset of strong P1 subset stimulation. Strong activation of the P1 subset acts as a mating command, while offset of P1 activity triggers persistent activity of their indirect targets, the pCD neurons, leading to a persistent aggressive state (Jung et al., 2020). The alternation of P1 and pCD activity is thought to be a mechanism by which males remember recent mating encounters and increase mating success by fending off other males that may pursue the same female. Interestingly, *Drosophila* aggression is modular (Duistermars et al., 2018). Three neurons that control threat displays, but not further aggressive behaviors, have been identified. Providing variable thermogenetic and optogenetic stimuli to these neurons evoked variations in threat display behavior, indicating that variable stimuli can evoke variable behavior at the level of locomotor circuitry.

Many organisms experience behavioral states that modulate motor outputs, and evidence of how this modulation occurs has been found across species. For example, state-dependent modulation of neural activity is observed in multiple neural populations of the dorsal raphe in mice. The activity of serotonergic neurons in the dorsal raphe decreases as mice move to complete approach and avoidance tasks under low stress, during which mice respond to an aural cue and cross an operant chamber to receive a reward or avoid a shock (Seo et al., 2019). In contrast, these neurons become more active as movement increases in the high threat state of the tail suspension test. Optogenetic stimulation of these serotonergic neurons increased movement when animals are in a low stress state and decreased movement while animals were in a high stress state. GABA-releasing neurons in the dorsal raphe were found to increase activity only during movement associated with negative valence, regardless of stress state. Stimulating these neurons during both the avoidance task and the tail suspension task increases movement, but these neurons do not promote neutral and positive-valence movement. This study indicates that specific circuitry upstream of the motor circuitry, in this case the dorsal raphe, can differentially affect behavior depending on behavioral state.

Another example of state dependent circuit function from *Drosophila* illustrates how motor circuitry that responds to a looming stimulus is influenced by behavioral state (Ache et al, 2019). Descending neurons that generate landing behavior in response to looming do not respond to visual looming stimuli when flies are not in flight. This system implements two separate gating mechanisms; one descending neuron type is gated by the neuromodulator octopamine, which is released during flight, while the other type is thought to be gated by direct feedback from motor outputs.

In addition to behavioral states, overall network states influence variability in standardized behavioral tasks. Attentiveness during a task is known to change average electrical activity of local networks, and these changes in network activity are positively correlated with performance of tasks that require focused attention (Fontanini and Katz, 2008). Visual cortex synchronization and parietal cortex baseline activity correlate with speed and accuracy of visual fixation tasks in non-human primates, respectively, and in rat gustatory cortex a 7-12 Hertz rhythm was found to be associated with periods of

disengagement during a licking task (Fontanini and Katz, 2004, Womelsdorf et al., 2006, Zhang et al., 2014). Stimulus-induced changes to firing in the olfactory bulb of mice decrease when pre-stimulus firing is high (Li et al., 2017). Mice were trained in an odorant-cued reward task in which they were rewarded for licking in association with one odorant but not another. While learning the task, pre-stimulus firing rates in the olfactory bulb were lower for the condition in which the mouse falsely licked for the non-reward odorant than for the condition in which the mouse refrained from licking the non-reward odorant, suggesting that the pre-stimulus firing rate may reflect anticipatory status. While it is clear that network states influence behavior, how these networks evolve over time and the mechanism through which they affect behavioral output is nebulous.

### ***C. elegans* as a model for understanding behavioral variation.**

The nematode *Caenorhabditis elegans* has a compact, well-defined nervous system and an easily studied behavioral repertoire, making it an ideal candidate organism to elucidate mechanisms that underlie behavioral variation. The connectome of *C. elegans* is mapped, and its nervous system is easily manipulated with genetic tools that allow individual neural types to be interrogated. It is optically transparent, allowing easy visualization of neural activity. *C. elegans* changes its behavior as stimuli change and as the context of stimuli is manipulated. It exhibits behavioral states that modulate its locomotion, and network states have been found to influence its behavioral output. This thesis focuses on a single interneuron, RIM, and a single behavior, the reversal, to better understand how the circuits driving motor outputs accomplish the seemingly contradictory tasks of generating appropriate and variable behaviors.

RIM is multifunctional. According to the *C. elegans* wiring diagram it receives inputs from ~10 neurons and forms synapses onto ~14 interneurons and motor neurons, as well as neuromuscular junctions (Figure 1-1). RIM releases two neurotransmitters, the biogenic amine tyramine (~noradrenaline) and glutamate. Each of these neurotransmitters modulate multiple targets, with tyramine signaling both synaptically and extrasynaptically. Finally, RIM makes gap junctions with 5 classes of integrating neurons. RIM is implicated in regulating *C. elegans* behavior across stimuli, behavioral states, and network states. It is thus an ideal candidate for the study of how motor outputs are both varied and cohesive.

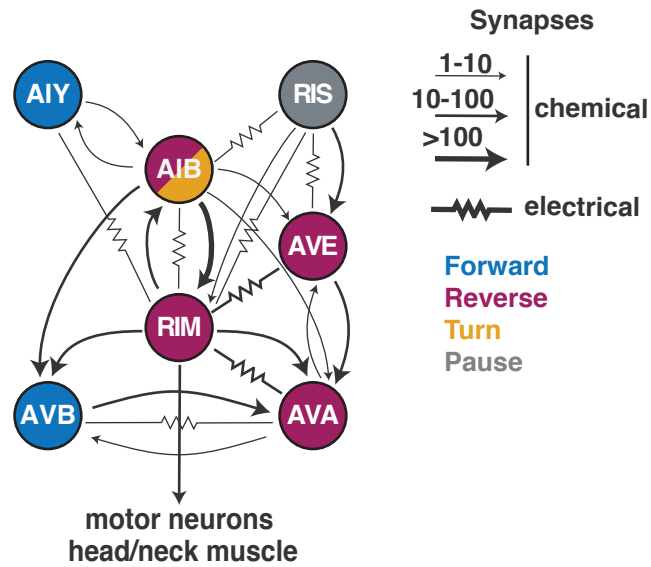


**Figure 1-1. The synaptic partners of RIM.**

RIM synapses onto interneurons, motor neurons, and muscle. Previous work has implicated RIM and its synaptic partners in various aspects of *C. elegans* locomotion, indicated by color. Postsynaptic motor neurons are: RMF, RMD, and SMD. AVK, AVJ, SAA, ADA, RIA, RIB, & RIC are also postsynaptic to RIM. AIZ, SAA, RIC, ADA, RIF, AVK, ALN, ASH, HSN, RIB, AVL, RIA, PVP, & AVH are also presynaptic to RIM. Modified from Gordus et al., 2015. Synaptic connections based on electron microscopy; data from [www.wormwiring.org](http://www.wormwiring.org) and [www.wormweb.org](http://www.wormweb.org) (Cook et al., 2009, White et al., 1986).

### **Locomotion and Reversals in *C. elegans***

*C. elegans* locomotion consists of forward movement, gradual steering, reversals, and high amplitude turns. The animal moves forward and backward by propagating a sinusoidal dorsoventral wave against its direction of motion, generated by alternate contraction and relaxation of the dorsal and ventral body wall muscles (Croll 1975, Gjorgjieva et al., 2014, Zhao et al., 2003). *C. elegans* generates sharp turns known as omega turns in which the nose of the worm touches the tail and, less frequently, executes shallower turns (Croll 1975, Gjorgjieva et al., 2014). These turns usually occur immediately after a reversal but can also be generated on their own (Gray et al, 2005, Huang et al., 2006). Reversals are a major component of *C. elegans* locomotion, and are used during escape response, taxis, foraging, and mating. *C. elegans* executes taxis behaviors to navigate toward appetitive stimuli, including chemotaxis, aerotaxis, and thermotaxis, among others.

### *Reversals and turns during escape*

*C. elegans* responds to gentle touch on the anterior body through the touch neuron ALM, and to gentle touch on the nose through the sensory neurons ASH, FLP, and OLQ, in each case initiating a reversal that is typically followed by an omega turn (Alkema et al., 2005, Chalfie et al., 1985, Kaplan and Horvitz, 1992). It responds to harsh touch on the anterior body via BDU and SDQR sensory neurons and initiates a much longer reversal (Li et al., 2011). AVA, AVD, and perhaps AVE are the reversal command interneurons that drive the initiation of reversals. In order to abolish reversals in response to gentle anterior touch, both AVA and AVD must be ablated (Chalfie et al., 1985). Similarly, harsh anterior touch response persists unless all three reversal neurons are ablated, indicating that behavioral fidelity is enforced through redundant pathways.

RIM is implicated in multiple aspects of the *C. elegans* escape response. Gentle anterior touch normally suppresses head oscillations during reversals, which requires tyramine signaling from RIM to head motor neurons and neck muscles (Alkema et al., 2005, Pirri et al., 2009). RIM tyramine also signals through the G-alpha-coupled GPCR SER-2 to VD motor neurons in the ventral nerve cord to promote efficient omega turning (Donnelly et al., 2013). Moreover, tyramine from RIM is required for the extension of reversal length in response to gentle touch that allows for coupling of reversals to omega turns (Alkema et al., 2005). RIM extends reversals by depolarizing the forward command neuron AVB through the tyramine-gated chloride channel LGC-55, the same channel that inhibits head oscillations through the head motor neurons (Pirri et al., 2009). RIM promotes efficient escape response by coordinating all of these motor programs.

### *Reversals and turns during taxis behaviors*

During chemotaxis, *C. elegans* uses two locomotor strategies in parallel: steering and a biased random walk. Steering involves a gradual turning toward higher concentrations of a chemical, such as an appetitive odor associated with a food source (Iino and Yoshida, 2009). In contrast, the biased random walk is implemented by sharp changes in orientation, where animals decrease their probability of reversals and omega turns as they move up an odor gradient and increase their probability of reversals and omega turns as they move down an odor gradient (Pierce-Shimomura, et al., 1999). The role of RIM in these behaviors is not defined.

### *Reversals and turns during foraging*

*C. elegans* modifies its locomotion depending on whether it is in the presence or absence of food. When entering a bacterial lawn, *C. elegans* slows its forward speed, which is accomplished through the signaling of mechanosensitive dopamine neurons (Sawin et al., 2000). In addition, *C. elegans* executes different frequencies and forms of reversal behaviors on and off of food (Gray et al., 2005, Chalasani et al., 2007). While

on food *C. elegans* mostly executes short reversals, consisting of 1-2 sinusoidal head swings. When removed from food, reversal frequency remains approximately the same, but reversal length extends so that reversals include at least 3 head swings, a distance that corresponds to about half of a body length. Reversals consisting of at least 3 head swings increase 10- to 20-fold upon removal from food (Gray et al., 2005). This switch to longer reversals persists throughout the time animals are off food, but the overall frequency of reversals falls over time off food, in a behavioral state transition described below (Calhoun et al., 2014, Chalasani et al., 2007, Gray et al., 2005, Hills et al., 2004, López-Cruz et al., 2019, Wakabayashi et al., 2004). The mechanism by which food alters reversal lengths is not understood.

*C. elegans* executes omega turns as it terminates most long reversals, and the coupling of reversals to omega turns increases as reversal length increases (Gray et al., 2005). Almost all omega turns off of food occur after reversals of 3 head swings or more. During foraging, laser ablation of RIM leads to an increase in spontaneous short reversals on and off of food. Moreover, tyramine from RIM regulates spontaneous reversal behavior, as tyramine mutants increase reversal frequency and decrease reversal length during off-food foraging (Alkema et al., 2005, Pirri et al., 2009).

### ***C. elegans* modulates its behavior in response to stimulus strength and context**

The strength of sensory stimulus affects the probability and strength of the resulting behavioral response. *C. elegans* avoids noxious thermal stimuli by executing an escape response, which includes a reversal and an omega turn (Ghosh et al., 2012, Stephens et al., 2008, Wittenburg and Baumeister, 1999). As animals encounter a stimulus of increasing temperature, certain parameters of the escape behavior change, while others remain constant (Ghosh et al., 2012). Probability of response, time spent executing a reversal, and peak reversal speed all increase as temperature increases, while time spent pausing prior to a reversal and time to respond decrease. However, time spent executing an omega turn remains constant. Thus, *C. elegans* modulates aspects of the escape response as noxious thermal stimuli vary but maintains stereotyped omega turns across thermal stimuli.

*C. elegans* also modulates its behavior in response to other types of aversive stimuli. The sensory neuron ASH detects noxious chemical and mechanosensory stimuli, and its activation elicits an escape response (Bargmann et al., 1990, Hart et al., 1999, Kaplan and Horvitz, 1992). The degree of this escape response has been shown to increase as the concentration of osmotic stimuli increases; higher concentrations evoke reversals in a larger fraction of animals and produce longer reversals, which are eventually followed by omega turns (Hori et al., 2018, Zou et al., 2018). Efficient escape from highly noxious stimuli requires the interneuron AIB, which receives glutamatergic input from ASH, promotes turning, and has bidirectional chemical synapses and electrical connections with RIM. AIB expresses two glutamate receptors, GLR-1 and GLR-5, which are activated by glutamate from synaptic vesicles and required for response to weak and strong activation of ASH, respectively, generating a thresholding

mechanism in AIB (Zou et al., 2018). Activation of GLR-5 is thought to evoke signaling to RIM through an unknown AIB neuropeptide, and this pathway may lead to feeding suppression. In addition, another study found that AIB's gap junctions, but not its chemical synapses, are necessary for optimizing turn probability in escape behavior in response to increasing noxious osmotic stimuli (Hori et al., 2018). Thus, AIB and RIM work within the greater reversal circuitry to both promote escape and inhibit feeding in response to different stimulus levels.

RIM has also been shown to integrate sensory inputs to inform foraging decisions. RIM is required to integrate appetitive olfactory cues from food with noxious osmotic stimuli to inform decision making depending on satiety (Ghosh et al., 2016). Starving worms are more likely to cross a highly noxious barrier to chemotax toward an attractive odor. In well-fed worms RIM signals to the osmosensory ASH neuron extrasynaptically via tyramine, sensitizing animals to the noxious stimulus. This pathway is inhibited in starved worms, allowing them to cross a noxious barrier in search of food. RIM also inhibits feeding in the presence of aversive odors by inhibiting NSM, a neuron in the pharynx (Li et al., 2012). In the presence of appetitive odors, NSM is activated and inhibits RIM, promoting feeding. This cross inhibitory circuit may produce bistable feeding states regulated by sensory cues.

More broadly, *C. elegans* is more responsive to noxious osmotic and olfactory stimuli in the presence of food rather than in the absence of food. Latency to reversal in response to an osmotic stimulus decreases and percent of animals responding increases in the presence of food, presumably because starving animals are less invested in avoiding aversive stimuli as they search for food. (Chao et al., 2004, Ezcurra et al., 2011, Wragg et al., 2007). Two neuromodulators, serotonin and dopamine, are implicated in facilitating this sensitivity, along with many neuropeptides (Hapiak et al., 2013). Interestingly, the tyramine receptor TYRA-3 has been suggested to antagonize increased sensitivity on food, while TYRA-2 in the AIM interneurons is thought to promote feeding suppression, implicating the tyramineric RIM neuron as a regulator of this behavioral modulation (Fu et al., 2018, Wragg et al., 2007).

### **Behavioral states in *C. elegans***

*C. elegans* changes its patterns of spontaneous locomotion based on its behavioral state. While on food, *C. elegans* switches between two prolonged behavioral states: roaming and dwelling. Roaming consists of bouts of high-speed forward crawling with minimal turning, while dwelling is characterized by low forward speed and increased turning rates (Ben Arous et al., 2009, Fujiwara et al., 2002). Roaming and dwelling are regulated by both metabolic state and sensory stimuli and may indicate an exploration-exploitation decision as animals increase roaming when food quality is poor (Ben Arous et al., 2009, Shtonda and Avery, 2006). These two states are maintained by neuromodulators. The neuropeptide pigment dispersing factor (PDF) stabilizes roaming states, and release of the biogenic amine serotonin stabilizes dwelling states. RIM,

along with the interneurons AIY and RIA, promotes roaming through the PDF receptor PDFR-1, a GPCR that can increase cyclic AMP upon activation (Flavell et al., 2013).

*C. elegans* also exhibits different behavioral states over time after removal from food, called local search and global search. Immediately after removal from food, animals participate in local search, maintaining a high frequency of reversals coupled to omega turns in order to reencounter the recent food source. After about fifteen minutes, in the absence of any external chemical or mechanical stimuli, animals enter global search, a state with infrequent reversals, and engage in long forward runs in search of a new food source (Calhoun et al., 2014, Gray et al., 2005, Hills et al., 2004, López-Cruz et al., 2019, Wakabayashi et al., 2004). Local search is triggered by parallel glutamatergic mechanosensory and chemosensory modules that are thought to detect mechanical and chemical features of the food source (López-Cruz et al., 2019). Glutamate release from these neurons immediately after removal from food activates the G-protein coupled metabotropic glutamate receptor MGL-1 on interneurons to suppress their activity and release local search. After several minutes off food, the sensory neurons decrease their activity and decrease glutamate release onto MGL-1 interneurons. The resulting disinhibition of MGL-1 interneurons promotes global search.

Optogenetic stimulation of sensory neurons is more able to drive reversals during the local search state than in the global search state. By contrast, optogenetic stimulation of RIM robustly promotes reversals regardless of behavioral state (López-Cruz et al 2019). Together, these results show that both sensory activity and the downstream motor circuit's sensitivity to sensory activity are altered during the transition from local search to global search states.

Roaming, dwelling, local search, and global search are composed of the same locomotor components: forward movement, turning, and reversals. *C. elegans* modulates the duration and frequency of these behavioral subsets, reorganizing them to manifest behavioral states. Additionally, the neurons and transmitters that contribute to maintaining these behavioral states are multifunctional. Many of them influence behaviors and neural processes that are not directly tied to a particular behavioral state. While some of the mechanisms that cause animals to switch between states and maintain states have been uncovered, we are just beginning to understand the greater neural organization underlying these processes.

### **Network states influence behavioral output in *C. elegans***

Short-term network states that develop over a timescale of seconds contribute to behavioral variation in *C. elegans*. The olfactory neuron AWC signals to the reversal circuitry through connections to the interneuron AIB and the reversal command neuron AVA, both of which receive electrical and chemical outputs from RIM. AWC reliably responds to appetitive odor, but the activation of reversal behavior by odor removal varies from trial to trial (Chalasanani et al. 2007, Gordus et al., 2015). The activity of AIB, AVA, and RIM is highly correlated, and collectively these neurons exhibit sustained high



and low activity states. Artificial chemogenetic hyperpolarization of RIM increases the probability that both AIB and AVA will respond to odor (Gordus et al., 2015). Furthermore, knockdown of RIM chemical synapses through expression of Tetanus toxin causes all three neurons to become highly responsive to odor, indicating that RIM chemical synapses generate variability in the response to olfactory stimuli. Knocking down chemical synapses in RIM also results in more reliable reversal suppression in response to odor, suggesting that the responsiveness of the RIM-AIB-AVA circuit influences behavioral output. In summary, behavioral output to odor is influenced by a multineuron network state, and RIM chemical synapses increase variability in both network state and behavioral response to appetitive odor.

These network states likely extend to many neurons, not just AIB, RIM, and AVA. Calcium imaging of the complete *C. elegans* nervous system has revealed cyclical, global brain states that are hypothesized to correlate with locomotor patterns and transitions (Kato et al., 2015). The activity of neurons that drive reversals, such as RIM and AVA, is correlated with activity in many other neurons and anticorrelated with activity in another population of neurons, including those implicated in forward movement. The existence of global brain dynamics suggests that the circuits that drive forward movement and reversals may drive many neurons into stable high or low states. Silencing the reversal command neuron AVA truncates reversals, but does not disrupt overall brain dynamics, indicating that these dynamics are stable and may only be disrupted by changing the activity of multiple neurons simultaneously.

It is possible that the intrinsic dynamics and stability of whole brain activity states restrict behavioral parameters. For example, they may dictate the maximum time an animal can spend reversing or turning. At the same time, the global brain states respond to sensory input. For instance, oxygen conditions that promote reversals increase the probability of time spent in the state associated with reversals (Kato et al., 2015).

Large scale brain dynamics may be associated with long-lasting behavioral states as well as shorter forward and reversal motor states. For example, roaming and dwelling states are represented in the activity patterns of 10 neurons relevant to these behavioral states in ways that are not simply correlated with forward and reverse motion (Ji et al., 2020).

### **A role for RIM in learning and memory**

As described above, RIM modulates acute reversal behavior, integration of sensory information, maintenance of behavioral states, and generation of behavioral variability. In addition, RIM contributes to learned pathogen avoidance. *C. elegans* shows a naïve preference for the pathogenic bacteria PA14 but learns to avoid it after infection. In adult animals, RIM is required for animals to modify turning rates to chemotax away from PA14 and toward another bacterial food source (Ha et al., 2010). Similarly, RIM is necessary for imprinting, through which larval *C. elegans* exposed to PA14 at a critical timepoint remembers to avoid it as an adult (Jin et al., 2016). RIM is required during

memory formation and sends an extrasynaptic tyraminergetic signal to the interneuron AIY via the G-protein coupled tyramine receptor SER-2. AIY, in turn, is required for memory retrieval. Thus, RIM is important for memory formation on two different time scales.

### **RIM co-transmits glutamate and tyramine**

A single neuron can have several downstream effects through co-transmission – the release of multiple neurotransmitters from some combination of classical synaptic vesicles and dense core vesicles. RIM acts as the major source of the noradrenaline-like transmitter tyramine in the *C. elegans* nervous system. Tyramine is synthesized by the enzyme tyramine decarboxylase (TDC-1) and packaged into synaptic vesicles by the vesicular monoamine transporter CAT-1 (VMAT), both of which are expressed by RIM (Alkema et al., 2005, Duerr et al., 1999, Serrano-Saiz et al., 2017). RIM also expresses the gene for EAT-4, a homolog of the mammalian vesicular glutamate transporter VGLUT, making it glutamatergic (Lee et al., 1999, Serrano-Saiz et al., 2013). While RIM's tyraminergetic output has been implicated in shaping reversal and turning behavior, memory formation, and sensory integration, among other behaviors and neural processes, its glutamatergic pathway is not well characterized.

While co-transmission was initially discovered in 1972 in the electric organ of the Pacific electric ray and postulated by Burnstock in 1976, its functional and behavioral implications are poorly understood (Burnstock, 1976, Burnstock, 2004, Hnasko and Edwards, 2012, Whittaker et al., 1972). Co-release occurs when neurotransmitters are released from the same synaptic vesicles, as opposed to from distinct vesicles from a single neuron (Hnasko and Edwards, 2012, Vaaga et al., 2014). When co-transmitted neurotransmitters are segregated into different vesicles, they may be spatially segregated, being released onto different postsynaptic targets, or be differentially sensitive to intracellular calcium levels, requiring different levels of neural activity for release. Co-transmission may increase the complexity of neuronal computations and vary the chemical output of a neural population during different network states or behavioral states.

### **Glutamatergic co-transmission**

Glutamatergic co-transmission is widespread throughout mammalian nervous systems and has been detected in dopaminergic, cholinergic, serotonergic, noradrenergic, and GABAergic neurons (Trudeau and El Mestikawy, 2018). Packaging of neurotransmitters by vesicular transporters relies on electrochemical gradients generated by the vacuolar-type hydrogen-ATPase and in some cases, as with VGLUT, gradients generated by the transporters themselves (Hnasko and Edwards, 2012, Vaaga et al., 2014).

The presence of VGLUT in the vesicular membrane can increase the packaging efficiency of other vesicular transporters through vesicular synergy. Efficient packaging of the monoamines and acetylcholine by VMAT and the vesicular acetylcholine

transporter (VACHT), respectively, requires a strong pH gradient. Packaging of anionic glutamate through VGLUT relies more on electrical gradients and maximizes the pH gradient (El Mestikawy et al., 2011). Thus, co-expression of VGLUT and VMAT or VACHT enhances packaging of monoamines or acetylcholine.

Evidence of vesicular synergy in mice indicates that glutamatergic co-transmission is important for the proper generation of behaviors attributed to neurotransmitters co-released with glutamate. Knocking out VGLUT3 in mice decreased acetylcholine release from the striatum as measured by microperfusion of striatal slices and scintillation counting and decreased acetylcholine uptake into vesicles as measured by superfusion (Gras et al., 2008). VGLUT3 KO mice also have hyperactivity phenotypes in response to cocaine that are rescued by inhibiting acetylcholinesterase in the striatum, suggesting that this behavioral phenotype is due to diminished acetylcholine release. Similarly, knocking out VGLUT2 in dopaminergic neurons of mice reveals that vesicular synergy enhances dopamine packaging in the ventral tegmental area (Hnasko et al., 2010). Conditionally knocking out VGLUT2 in dopaminergic neurons diminished dopamine release from ventral striatum tissue as measured by high performance liquid chromatography and fast-scanning cyclic voltammetry. Moreover, co-transfecting HEK293T cells with VMAT and VGLUT2 showed that expression of VGLUT2 enhanced VMAT packaging of biogenic amines as measured by scintillation counting. Conditional VGLUT2 KO mice also showed decreased hyperactivity in response to cocaine, a phenotype associated with loss of striatal dopamine.

Importantly, dopamine neurons in the mouse brain express VGLUT2 early in development, and conditional loss of VGLUT2 leads to loss of dopaminergic mesencephalic neurons in cell culture, as well as impaired neurite complexity and axon growth of cultured dopaminergic neurons. Thus, glutamatergic co-transmission may be important for proper neuron development (Fortin et al., 2012). In contrast to knocking out VGLUT, knocking out the glutamate-recycling enzyme phosphate-activated glutaminase (PAG) selectively decreases neurotransmission at higher neural firing frequency (Gaisler-Salomon et al., 2009). Indeed, knocking out PAG in dopaminergic neurons selectively decreased glutamatergic excitatory post-synaptic currents in the nucleus accumbens during burst-evoking optogenetic stimulation, but did not alter single-evoked currents (Mingote et al., 2017). Fast-scanning cyclic voltammetry of slices from the nucleus accumbens revealed that dopamine release in dopaminergic PAG KO mice was intact, and while these animals had behavioral phenotypes such as reduced sensitization to amphetamine injections indicated by hyperactivity, they did not exhibit phenotypes associated with VGLUT KO mice, such as initial blunted hyperactivity in response to amphetamine or cocaine. These results indicate that glutamate co-transmission regulates behaviors not attributed to neuronal development or vesicular synergy.

In *Drosophila*, octopamine and glutamate are co-transmitted and have both cooperative and differential effects on male mating behavior, providing another example of how co-transmission regulates behavior apart from vesicular synergy and demonstrating that

co-transmission of classical neurotransmitters and neuromodulators is behaviorally relevant in invertebrates (Sherer et al., 2020). Reducing the *Drosophila* homolog of VGLUT specifically in octopaminergic neurons did not affect neuron survival nor distribution. Octopamine is required for promotion of male aggression and inhibition of intermale courtship. While flies with reduced VGLUT in octopamine neurons demonstrated diminished aggression similar to that of octopamine-deficient flies, exhibiting reduced lunging and wing threats as well as increased latency to initiate aggression, they suppressed intermale courtship behavior. Additionally, VGLUT is required for male aggression only in octopamine neurons, not motor neurons. Thus, co-transmitted glutamate works with octopamine to promote male aggression but does not play a role in suppressing male courtship, providing evidence that co-transmitted neurotransmitters can regulate different aspects of a greater behavior in invertebrates.

In addition to methods such as electrophysiological recording and fast-scanning cyclic voltammetry, pHluorin, a pH-sensitive GFP, can be used to study vesicular loading of neurotransmitters and to measure exo- and endocytosis dynamics. pHluorin has been imaged extensively in cell culture, as well as in dissected brain tissue and in intact *C. elegans* (Aguilar et al., 2017, Miesenböck et al., 1998, Onoa et al., 2010, Pan and Ryan, 2012, Silm et al., 2019, Ventimiglia & Bargmann, 2017).

Imaging pHluorin fused to VMAT in dopaminergic neurons in intact *Drosophila* brains has provided direct evidence of vesicular synergy. Upon depolarization, dopaminergic vesicles undergo hyperacidification prior to exocytosis, indicated by a decrease in pHluorin fluorescence (Aguilar et al., 2017). This period of hyperacidification was shown to be associated with increased dopamine loading into vesicles using a false fluorescent neurotransmitter. VGLUT and VMAT colocalized, and imaging pHluorin dynamics upon depolarization in VGLUT knockdown animals, as well as in animals overexpressing VGLUT, indicated that VGLUT bidirectionally contributes to the hyperacidification process, providing direct evidence that glutamatergic co-release aids dopamine packaging through vesicular synergy. Dopamine is known to promote basal locomotion and amphetamine-induced hyperactivity in *Drosophila*. VGLUT knockdown and overexpression decreased and increased these two behaviors, respectively, indicating that vesicular synergy in *Drosophila* regulates behavior.

pHluorin imaging has also provided evidence of co-transmission from distinct vesicles. Fusing pHluorin to VMAT2 and VGLUT1 in mouse neurons revealed that dopamine exhibits slower endocytosis dynamics than those of glutamate after a 10 Hz stimulation in both hippocampal neurons and midbrain dopaminergic neurons (Onoa et al., 2010). VMAT2 exocytosis dynamics differed from VGLUT1 in both hippocampal neurons and dopaminergic midbrain neurons in response to 10 Hz stimulation and emptying the vesicle pool by prolonged stimulation in the presence of a hydrogen pump inhibitor revealed that more glutamatergic vesicles reside in the readily releasable pool (Onoa et al., 2010, Silm et al., 2019). While differences in endocytosis dynamics can reflect a difference in the rate at which two proteins are targeted to the same endocytic pathway rather than a difference between endocytic pathways, differences in exocytosis

dynamics suggest that two proteins are on the cell surface at different times. Thus, this work indicates that VMAT2 and VGLUT1 are targeted to separate vesicles in these neuronal populations in mice.

Immunohistochemistry revealed that VMAT2 and VGLUT1 colocalized in hippocampal neurons but not in midbrain dopamine neurons, suggesting that colocalization alone does not indicate co-release from the same vesicles (Onoa et al., 2010). Moreover, simultaneous imaging of VMAT2 and VGLUT1 fused to red and green pHluorins indicated that dopamine release varies across synaptic boutons that express both transporters, providing further evidence that colocalization does not dictate co-release (Silm et al., 2019). Lastly, VMAT2 is more loosely coupled to presynaptic calcium channels than VGLUT1, as indicated by its increased inhibition in the presence of the slow calcium chelator EGTA, and VMAT2 exo- and endocytosis require the adaptor protein AP-3, while VGLUT1 dynamics were normal in AP-3 mutants (Pan and Ryan, 2012, Silm et al., 2019). These results indicate that biogenic amines are released separately from glutamate at some synaptic boutons, that biogenic amines and glutamate can have different requirements for release, and that they may rely on different recycling pathways.

## Thesis Overview

The goal of this thesis is to further elucidate the mechanisms by which behavioral outputs are organized and to better understand how these mechanisms generate behavioral variability. I accomplish this by dissecting the chemical and electrical outputs of RIM using precise genetic manipulations and by analyzing both spontaneous and optogenetically-evoked behaviors across behavioral states. I also compare the release and retrieval dynamics of the two neurotransmitters released from RIM to study the presynaptic organization of RIM chemical transmission and to clarify how RIM co-transmission contributes to the ability of RIM to organize behavior and generate behavioral variability.

In Part I, I focus on how RIM chemical synapses and gap junctions contribute to reversal behavior during off-food foraging. In Chapter 2, I uncover the role of RIM glutamate in the reversal circuit by generating a cell-specific glutamate vesicular transporter knockout. I find that RIM glutamate and RIM tyramine differentially regulate spontaneous reversal behavior. RIM glutamate mainly functions to inhibit all reversals during local search and has a modest effect on increasing reversal length, while tyramine specifically inhibits long reversals while increasing reversal length and speed. My results also suggest that RIM glutamate lengthens reversals by inhibiting the coupling of reversals to omega turns.

In Chapter 3, I further probe RIM chemical synapses by optogenetically stimulating RIM across behavioral states. I characterize the behavioral responses to RIM stimulation of increasing duration and show that there may be an intrinsic limit to the duration of evoked reversal states. I also find that, in contrast to their effect on spontaneous reversal behavior, RIM chemical synapses do not inhibit reversals upon direct stimulation of RIM. Despite this, I show that RIM chemical synapses, particularly RIM tyraminerbic synapses, are essential regulators of reversal parameters and are necessary to promote length and speed of reversals.

I also interrogate RIM gap junctions and find that they are bidirectional regulators of reversal frequency, both inhibiting spontaneous reversals and promoting reversals upon direct stimulation of RIM. Additionally, I show that RIM gap junctions strongly promote reversals during global search, but not local search. Thus, I uncover that, in contrast to previous findings, RIM is less coupled from the reversal circuit during local search. This uncoupling is downstream of RIM activity.

In Part II, I characterize and compare RIM glutamate and RIM tyramine exo- and endocytosis dynamics to better understand if the findings of Chapter 2 are influenced by presynaptic differences between RIM glutamate and RIM tyramine. I investigate whether or not packaging of RIM glutamate and RIM tyramine into distinct vesicles contributes to the ability of RIM to generate behavioral variation. I engineer and validate a reporter for biogenic amine release in *C. elegans* by fusing CAT-1 (VMAT) to pHluorin and compare the dynamics of this reporter to an EAT-4 (VGLUT) pHluorin fusion. My

preliminary data indicate that RIM glutamate and RIM tyramine share exo- and endocytosis dynamics but suggest that RIM tyramine may also be released from distinct vesicles with slower exocytosis dynamics than RIM glutamate.

I conclude that RIM plays a dual role in off-food foraging behavior, stabilizing both the forward and reversal states, and that RIM glutamate and RIM tyramine are likely released together during off-food foraging. My discussion will focus on the potential targets of RIM glutamate, the implications of my findings on the ability of RIM to generate behavioral variability, and how this work may be interpreted in the context of global brain dynamics, among other topics.

## **PART I**

### **CHAPTER 2: Co-transmitted neurotransmitters separately modulate reversals**

#### **Introduction**

Nervous systems process information through overlapping circuits that function within the context of higher-order network states. While we can glean information about how circuits function to generate behavior by probing individual components of a circuit, the conclusions drawn are constrained by the manipulations that are performed and the behavioral parameters that are measured. The ability to accurately describe how a particular neural node functions within a circuit to produce a behavior is challenging.

While the *C. elegans* nervous system is relatively small and its connections are mapped, we are only beginning to understand how *C. elegans* integrates sensory information and internal states to generate behavior. In *C. elegans*, information flows from sensory neurons (such as ASK and AWC) to primary interneurons (such as AIB) to secondary interneurons (such as RIM) to command premotor neurons (such as AVA and AVB) to motor neurons (Cook et al. 2019, Gray et al., 2005, Kaplan et al., 2018, White et al., 1986). The command neurons compress many inputs into forward and reverse locomotion states, which are additionally shaped by separate control of motor neurons. Importantly, there is a high level of interconnectedness and feedback within the 302 neurons, approximately 7,000 chemical synapses, and 900 gap junctions of the *C. elegans* nervous system, so the flow of information through this system is not obvious.

The interneuron RIM contributes to multiple aspects of reversal behavior off food, but despite the extensive research surrounding this neuron, its specific role within the reversal circuitry is enigmatic. Different experiments suggest that RIM can either inhibit or induce reversal behaviors. Killing the RIM neurons increases the spontaneous reversal frequency of foraging animals on and off of food, suggesting RIM inhibits reversals (Gray et al., 2005). In agreement with this result, acute optogenetic inhibition of RIM neurons with halorhodopsin triggers reversals in freely moving animals on food (Piggott et al., 2011). These reversals do not require the AVA, AVE, and AVD backward command neurons, which are required for most reversal behaviors. However, optogenetic activation of RIM also induces immediate reversals, suggesting that RIM can promote reversals (Gordus et al., 2015, Guo et al., 2009, López-Cruz et al., 2019). Most, but not all, calcium imaging experiments indicate that RIM is active during reversals, and not during forward locomotion (Piggott et al., 2011, Gordus et al., 2015, Kato et al., 2015; Kagawa-Nagamura et al., 2018).

The ambiguity of RIM function might be related to the fact that RIM uses two different chemical transmitters and gap junctions to signal in the reversal circuit (Figure 1-1). In its best-characterized function, RIM's tyraminergetic output has been implicated in shaping reversal and turning behavior, memory formation, and sensory integration,



among other behaviors and neural processes (Alkema et al., 2005, Donnelly et al., 2013, Fu et al., 2018, Ha et al., 2010, Hapiak et al., 2013, Jin et al., 2016, Li et al., 2012, Pirri et al., 2009, Wragg et al., 2007). RIM is also one of many glutamatergic neurons in *C. elegans* (Lee et al., 1999, Serrano-Saiz et al., 2013, Figure 2-1A). The function of RIM's glutamatergic output and electrical synapses is unknown.

Approximately 32% of *C. elegans* neurons express *eat-4* and are therefore believed to use glutamate as a neurotransmitter (Figure 2-1A). These glutamatergic neurons include chemosensory, thermosensory, and mechanosensory neurons, as well as AIB and RIM interneurons. Glutamate is detected by multiple excitatory AMPA and NMDA glutamate-gated cation channels, inhibitory glutamate-gated chloride channels, and metabotropic GPCRs. Remarkably, *eat-4* mutants are viable, but they have many changes in their stimulus-evoked and spontaneous behaviors, including reduced reversals, diminished escape behaviors, and other behavioral deficiencies (Berger et al., 1998, Ghosh et al., 2012, Harris et al., 2010, Hart et al., 1999, Lee et al., 1999, López-Cruz et al., 2019, Ohnishi et al., 2011, Ranken and Wicks, 2000, Wakabayashi et al., 2015). The roles of glutamate have been dissected using glutamate receptor mutants and by combining *eat-4* cell-specific rescue and knockout mutations with glutamate receptor mutants and rescues (Baidya et al., 2014, Chalasani et al., 2007, Choi et al., 2015, Hills et al., 2004, López-Cruz et al., 2019). However, because there are many classes of glutamatergic neurons and functionally distinct glutamate receptors coexist on many targets—for example, both excitatory and inhibitory glutamate receptors are expressed by the AVA backward command neurons—it is difficult to interpret the effects of null mutations in integrating networks (Hart et al., 1995, Maricq et al., 1995, Taylor et al., 2019). Compounding this complexity, integrating circuits are modified by both external contexts, like the presence of food, and internal network states, like those that represent motivational states, and these have indirect effects on information propagation.

In this chapter, I combine discrete manipulations of each of RIM's neurotransmitters with experiments across behavioral states to clarify the influence of RIM in reversal behavior. I focus on spontaneously generated reversals during off-food foraging to understand RIM's endogenous function. By generating and applying a cell-specific *eat-4* glutamate vesicular transporter knockout in RIM, I define the role of RIM glutamate in this circuit. I show that RIM glutamate and tyramine affect multiple reversal parameters, and that removing either neurotransmitter differentially affects the reversal circuit. My results indicate that RIM tyramine and glutamate act through different targets to stabilize both the reversal state and the forward state during spontaneous foraging off food.

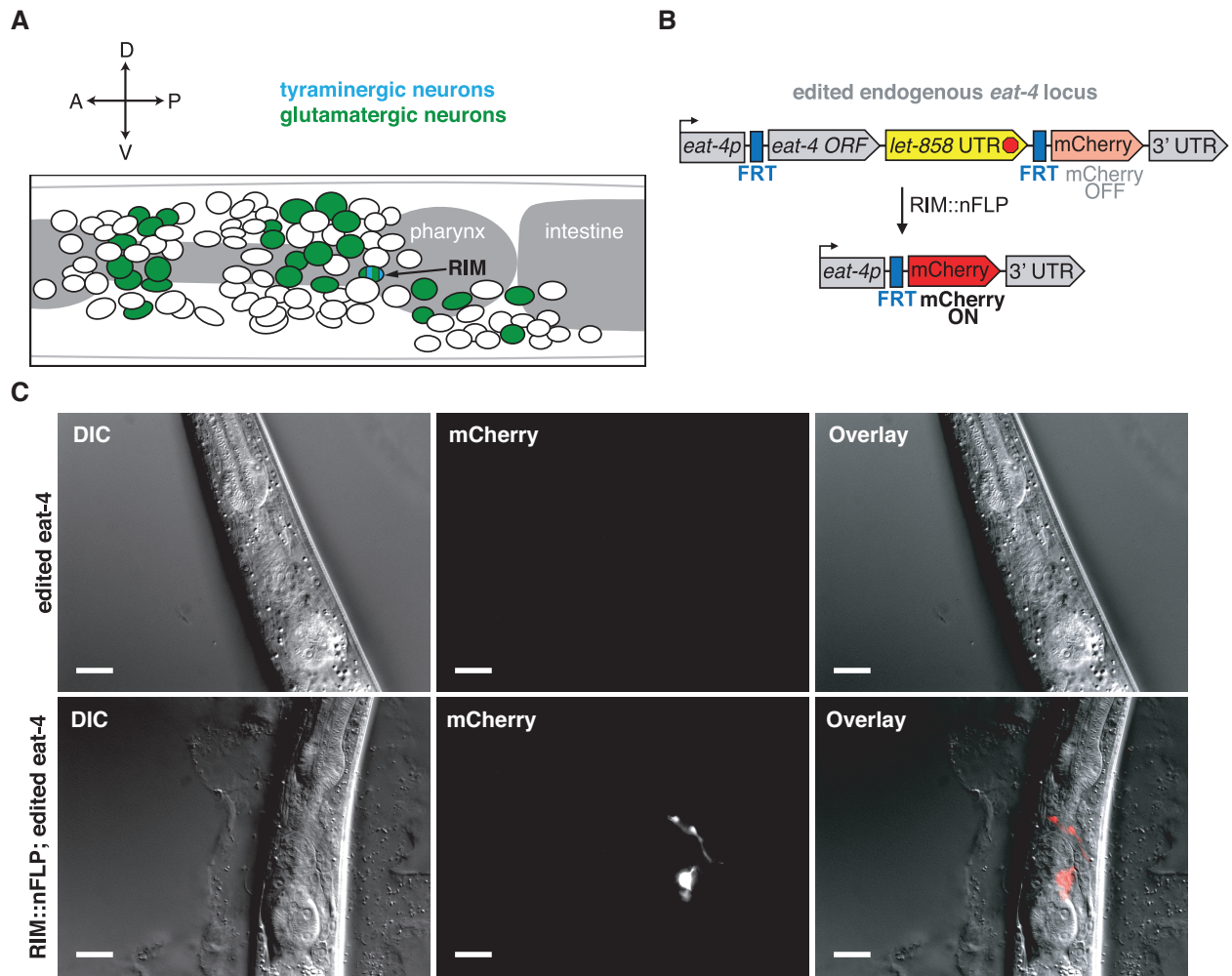


**Figure 2-1. A CRISPR-Cas9 generated, cell-specific glutamate knockout enables the elucidation of the role of RIM glutamate on reversal behavior.**

**Figure 2-1. A CRISPR-Cas9 generated, cell-specific glutamate knockout enables the elucidation of the role of RIM glutamate on reversal behavior.**

**(A)** Schematic of the sources of glutamate and tyramine in the *C. elegans* nervous system. Adapted from Pereira et al., 2015.

**(B)** Schematic of cell-specific glutamate transporter knockout genetic strategy. Using CRISPR/Cas9, an FRT site was inserted immediately before the start codon of *eat-4* (VGLUT) and *let-858* 3'-UTR:: FRT::mCherry immediately after the stop codon of *eat-4*. *let-858* 3'-UTR stops transcription so mCherry is not expressed. To knock out glutamate release in this edited strain, nuclear-localized flippase (nFLP) was expressed under a *tdc-1* promoter. The intersection of *tdc-1* and *eat-4* expression is limited to RIM leading to excision of the *eat-4* ORF in RIM, confirmed by mCherry expression in the targeted cells.

**(C)** Validation of CRISPR-Cas9 recombination. Top panel: Differential interference contrast (DIC) (left), mCherry fluorescence (middle), and merged (right) images of animals with edited endogenous *eat-4* (VGLUT) locus. In the edited strain there is no mCherry expression, confirming that the *let-858*-3'-UTR stops transcription. Bottom: DIC (left), mCherry (middle), and merged (right) images for edited *eat-4* strain following RIM-specific nFLP expression (*tdc-1p::nFLP*). mCherry is expressed only in RIM. mCherry specificity to RIM was confirmed by screening 30 animals. Scale bar is 20  $\mu$ M.

## Results

### *RIM glutamate inhibits reversal initiation and lengthens reversals together with tyramine*

As RIM releases both tyramine and glutamate neurotransmitters, I hypothesized that glutamate may contribute to RIM's modulation of reversal behavior. In collaboration with Alejandro López-Cruz, I generated a cell-specific glutamate knockout to ask how glutamate from RIM contributes to locomotion. Using CRISPR-Cas9, I edited the endogenous *eat-4* locus, which encodes the *C. elegans* homolog of the vesicular glutamate transporter VGLUT. I inserted flippase recognition targets (FRTs) directly preceding the start codon and after the stop codon of *eat-4*, such that the entire *eat-4* open reading frame (ORF) is excised by nuclear-localized flippase (nFLP) expression. I also inserted a *C. elegans* transcriptional stop sequence directly before the 3' FRT site and a sequence encoding the fluorescent protein mCherry directly after the 3' FRT site such that mCherry is expressed only upon *eat-4* ORF excision (Figure 2-1B). By driving nuclear-localized flippase using a RIM-specific promoter, I created a RIM-specific glutamate knockout (here termed RIM glu KO) that was confirmed by reliable and specific mCherry expression in RIM (Figure 2-1B, C).

To quantitatively evaluate the effects of RIM neurotransmitters, I examined RIM glu KO animals, tyramine-deficient *tdc-1* mutants, and RIM glu KO; *tdc-1* mutant animals that lack release of both RIM neurotransmitters. Spontaneous foraging behavior was recorded for 45 minutes after removing animals from a bacterial food lawn, a time period that encompasses local search and global search behavioral states (López-Cruz et al. 2019, Figure 2-2A).

The ~15-minute local search state is characterized by a high frequency of spontaneous reversals and is followed by a global search state with a low reversal frequency. This pattern was shared by RIM glu KO animals, tyramine-deficient *tdc-1* mutants, and RIM glu KO; *tdc-1* mutant animals (Figure 2-2B). The frequency of reversals was higher in all mutant genotypes than in wild-type animals during local search and will be characterized further below.

During the transition to global search, all mutants and wild-type animals had similar decreases in reversal frequency (Figure 2-2B), and by 30 minutes after removal from food their reversal rates were indistinguishable (Figure 2-2C), I conclude that glutamate and tyramine release from RIM are not essential for the underlying local search or global search behavioral states.

In all subsequent figures, local search behavior was quantified at 4-8 minutes after removal from food, and global search behavior at 40-45 minutes after removal from food.

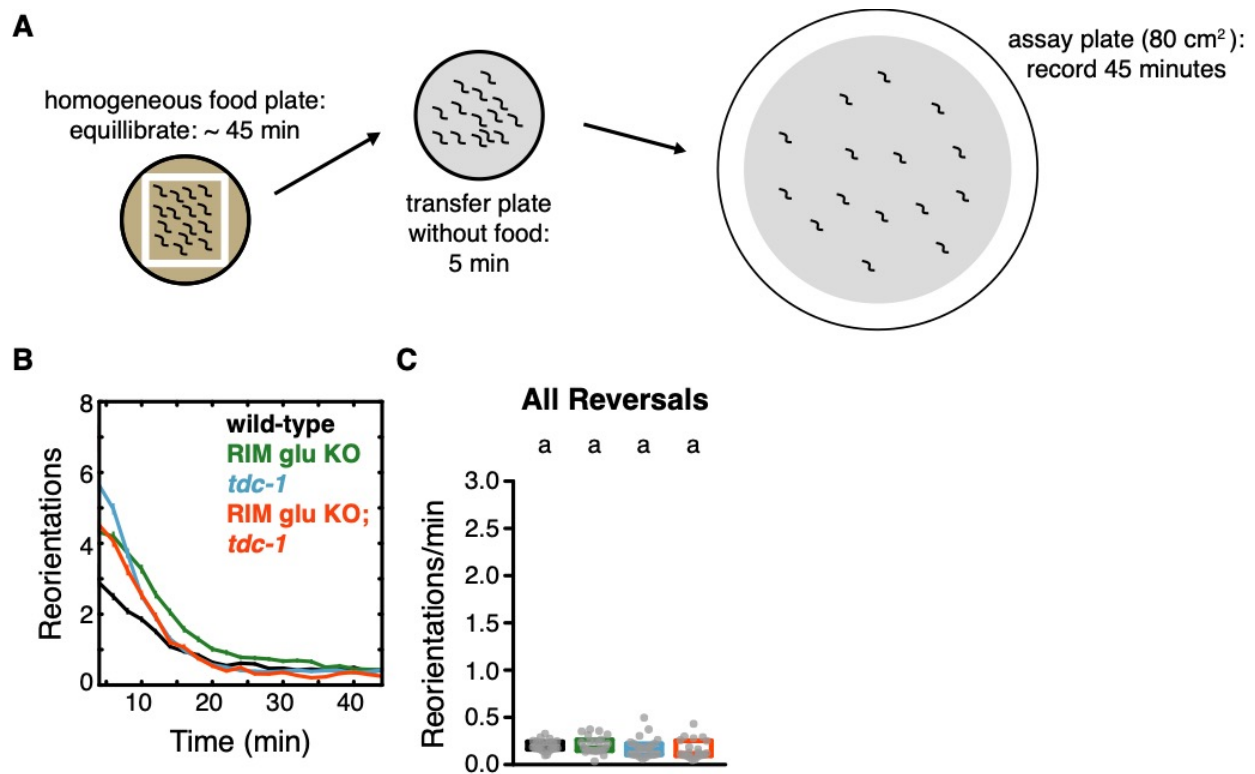


**Figure 2-2. RIM glutamate and tyramine do not affect the local search - global search transition or reversal frequency during global search.**

**(A)** Schematic of off-food foraging assay. White square and circle indicate copper ring. Adapted from López-Cruz et al., 2019.

**(B)** Average reversal frequency from minutes 4-45 of recording, binned by 2-minute intervals. Vertical dashes indicate standard error of the mean.

**(C)** Average frequency of all reversals during minutes 36-40 of global search. Each gray dot is 1 assay, n=12-15 animals per assay. Boxes indicate median and interquartile range. Different letters indicate statistical significance using a Kruskal-Wallis test with Dunn's multiple comparisons test.

See Methods & Appendices for further details.

The most striking effect of RIM glutamate and tyramine during local search was an increase in the frequency of reversals (Figure 2-3A). Each mutant, as well as the RIM glu KO; *tdc-1* double mutant, had a similar overall increase in all reversals. These results demonstrate that RIM glutamate and tyramine decrease reversal frequency during local search, but their effects are not additive or redundant, suggesting that they function in a common process.

Next, I examined the effects of RIM neurotransmitters on reversal characteristics. Previous results have demonstrated that RIM, and tyramine in particular, affect the length of reversals (Alkema et al., 2005, Gray et al., 2005, Pirri et al., 2009). Spontaneous reversals in *C. elegans* have a bimodal length distribution, with a natural break around 0.5 body lengths that separates short and long reversals. Using this 0.5 body length cutoff, RIM glu KO animals had increased frequency of both short and long reversals compared to wild-type, whereas *tdc-1* mutants only had increased frequency of short reversals (Figure 2-3A). The double RIM glu KO; *tdc-1* mutants resembled *tdc-1* mutants, with increased short reversals only.

To more rigorously evaluate the effects of RIM glutamate and tyramine, the full reversal length distributions were examined in wild-type and mutant backgrounds (Figure 2-3B). In wild-type animals, short reversals averaged ~ 0.15 body lengths, and long reversals averaged ~1 body length. RIM glu KO mutants maintained a bimodal length distribution, but long reversals were shortened with a peak at ~0.8 body lengths (Figure 2-3B). *tdc-1* mutants and RIM glu KO; *tdc-1* double mutants had distributions consistent with short (0.15 body length) and long (>0.5 body length) classes that were poorly resolved, or with a single class of reversals. RIM glu KO; *tdc-1* mutant animals closely resembled *tdc-1* mutants. Together, these results indicate that tyramine and glutamate act together to suppress reversal initiation and to lengthen reversals, with tyramine having a quantitatively larger effect on reversal length.

Compared to reversal length, less is known about neurons responsible for controlling reversal speed (Ghosh et al., 2012, Ghosh et al., 2015, Kato et al., 2015, Ardiel et al., 2018, Zhao et al., 2003). Plotting the distributions of reversal speeds revealed that reversals in *tdc-1* mutants were significantly slower than in wild-type. The RIM glu KO had only a slight change in reversal speed, and the RIM glu KO; *tdc-1* mutant resembled the *tdc-1* mutant (Figure 2-3C). These results indicate that tyramine increases reversal speed, while RIM glutamate has a minimal effect.

In control experiments, spontaneous behavior was minimally affected in the FRT-edited *eat-4* strain, in animals expressing nFLP in RIM, and in animals expressing the co-injection marker *pelt-2::nGFP* (Figure 2-4). The slight change in reversal speed in the RIM glu KO was also observed in animals expressing the *elt-2p::nGFP* coinjection marker (Figure 2-4C), suggesting that this effect may not be biologically significant.

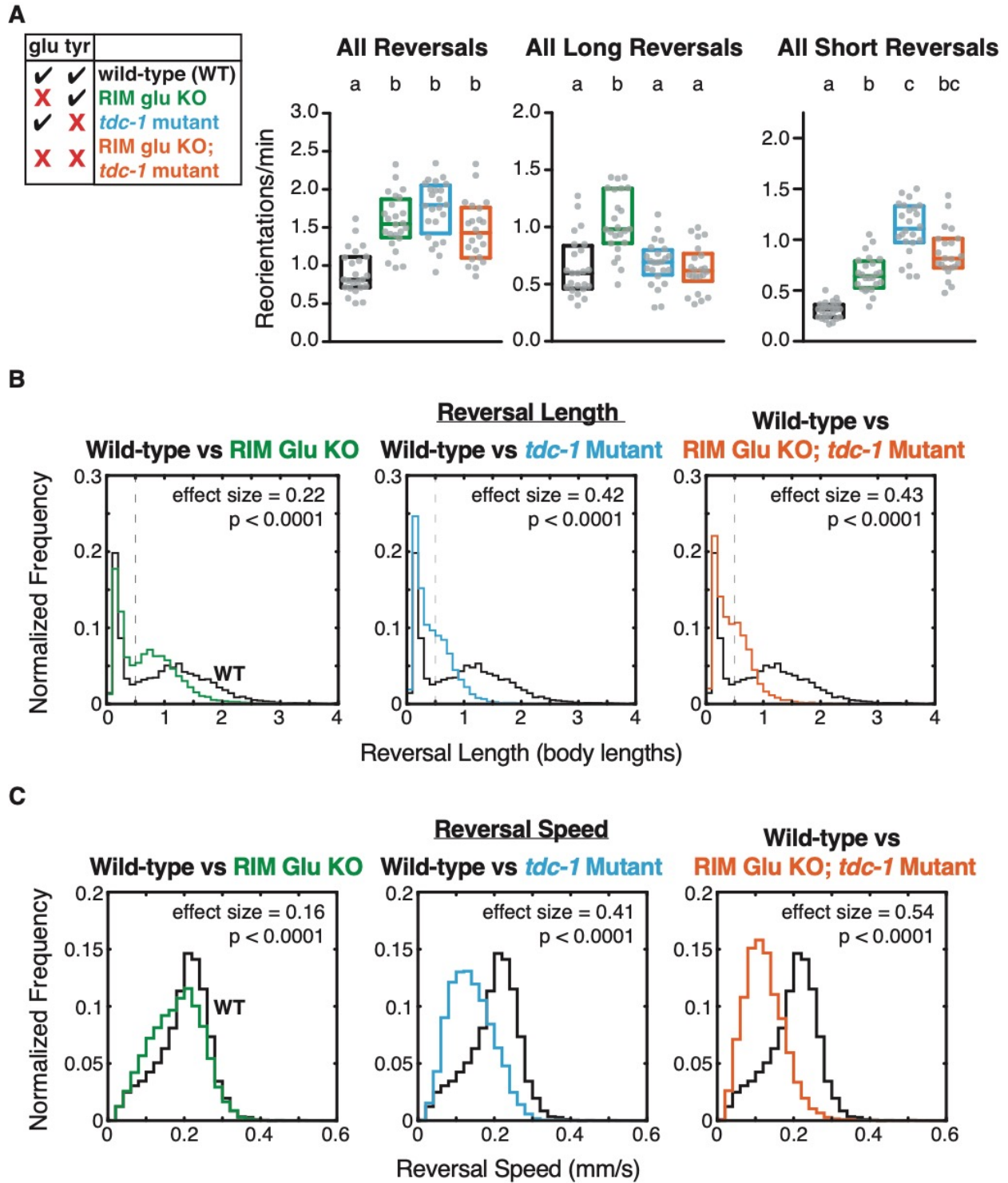


**Figure 2-3. RIM glutamate decreases reversal frequency during off-food foraging; tyramine decreases reversal frequency in parallel by increasing reversal length and speed.**

**Figure 2-3. RIM glutamate decreases reversal frequency during off-food foraging; tyramine decreases reversal frequency in parallel by increasing reversal length and speed.**

**(A)** Average frequency of reversals during minutes 4-8 of local search. Left panel: all reversals regardless of length. Middle panel: only long reversals (>0.5 body lengths). Right panel only short reversals (<0.5 body lengths). Each gray dot is 1 assay, n=12-15 animals per assay. Boxes indicate median and interquartile range. Different letters indicate statistical significance using a Kruskal-Wallis test with Dunn's multiple comparisons test.

**(B)** Distributions of reversal length of all reversals over entire 45-minute recording normalized by probability. Dotted line indicates the separation of short and long reversals in the wild-type. Wild-type (WT) distribution is plotted in all panels; left: against RIM glu KO; middle: against *tdc-1* mutant; right: against *tdc-1* mutant; RIM glu KO.

**(C)** Distributions of reversal speed of all reversals over entire 45-minute recording normalized by probability. Wild-type (WT) distribution is plotted in all panels; left: against RIM glu KO; middle: against *tdc-1* mutant; right: against *tdc-1* mutant; RIM glu KO.

**(B)** and **(C)** n=8851-13419 reversal events from 22-24 assays. p is the significance of the difference of each experimental group compared to wildtype based on the Kolmogorov-Smirnov test, effect size is the D statistic.

See Methods & Appendices for further details.



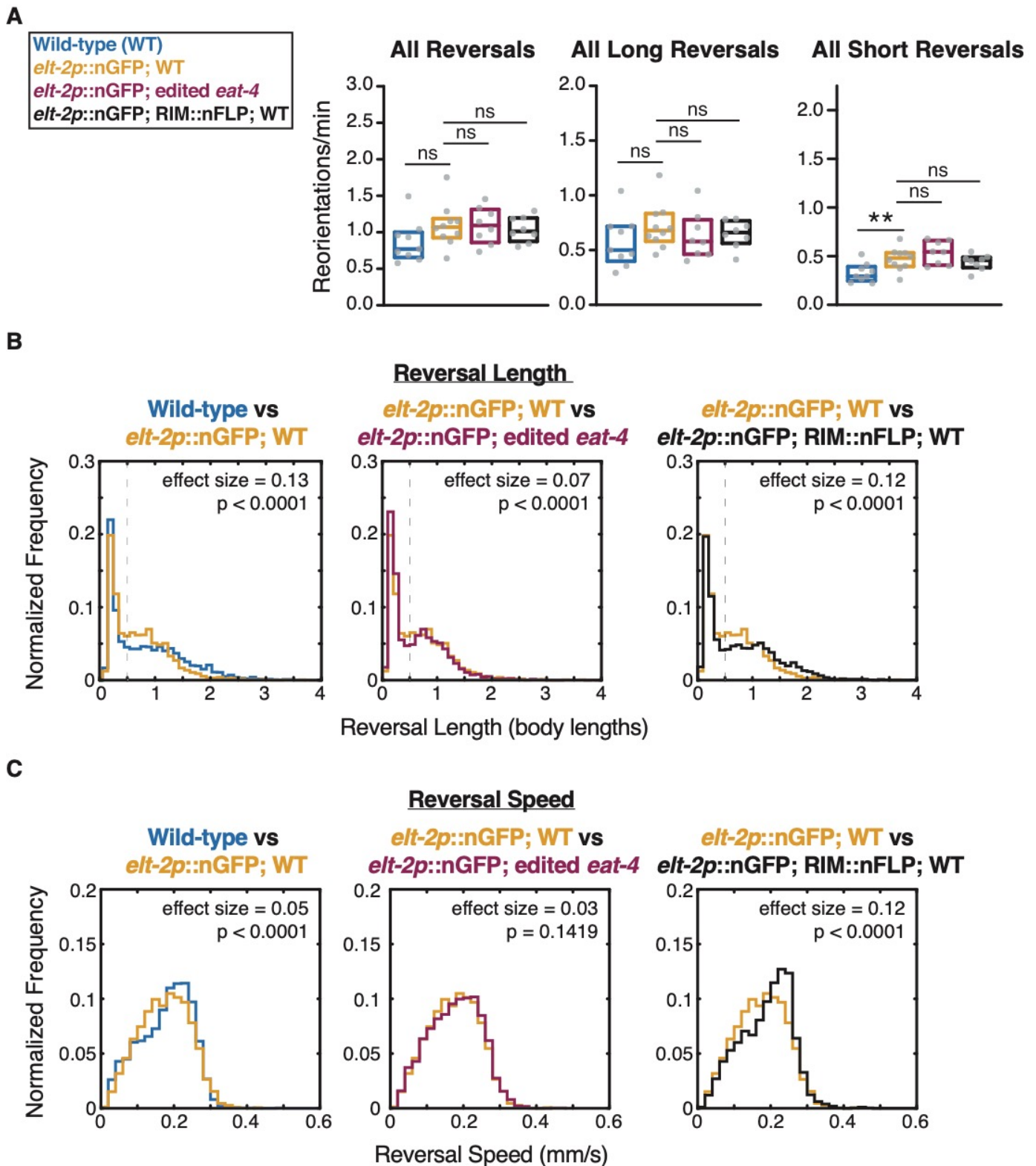


**Figure 2-4. Edited *eat-4* locus, nFLP expression, or co-injection marker alone do not account for changes in behavior in a RIM-specific glutamate knockout. Supplement to Figure 2-2.**

**Figure 2-4. Edited *eat-4* locus, nFLP expression, or co-injection marker alone do not account for changes in behavior in a RIM-specific glutamate knockout. Supplement to Figure 2-2.**

**(A)** Average frequency of reversals during minutes 4-8 of local search. Left panel: all reversals regardless of length. Middle panel: only long reversals (>0.5 body lengths). Right panel only short reversals (<0.5 body lengths). Each gray dot is 1 assay, n=12-15 animals per assay. Boxes indicate median and interquartile range. Asterisks indicate significant difference between 2 conditions using Mann-Whitney test; ns = not significant.

**(B)** Distributions of reversal length of all reversals over entire 45-minute recording normalized by probability. Dotted line indicates the separation of short and long reversals in the wild-type. *elt-2p::nGFP*; WT distribution is plotted in all panels; right: against wild-type (WT); middle: against *elt-2p::nGFP*; edited *eat-4*; right: against *elt-2p::nGFP*; RIM::nFLP; WT.

**(C)** Distributions of reversal speed of all reversals over entire 45-minute recording normalized by probability.

**(B)** and **(C)** n=2985-3366 reversal events from 8-10 assays. p is the significance of the difference of each experimental group compared to wildtype based on the Kolmogorov-Smirnov test, effect size is the D statistic.

See Methods & Appendices for further details.

While the experiments described above were designed to test the roles of different RIM neurotransmitters, it was possible that some of them could be explained by different pathways. For example, TDC-1 is required for synthesis of both tyramine and octopamine, which have distinct effects on behavior in *C. elegans*. Octopamine in *C. elegans* is produced primarily by the RIC neurons, which in addition to *tdc-1* express *tbh-1*, which encodes the tyramine beta-hydroxylase that converts tyramine to octopamine (Alkema et al., 2005). To determine whether the effects of *tdc-1* are due to tyramine or octopamine, I examined spontaneous behavior in octopamine-deficient *tbh-1* mutants. *tbh-1* mutants have normal reversal frequency, reversal length, and reversal speed during local search behavior (Figure 2-5). Therefore, the effects of *tdc-1* on spontaneous reversals are primarily due to a loss of tyramine, consistent with previous studies.

Finally, to confirm these results through a different method, I used an independent approach to disrupt both glutamatergic and tyraminergetic RIM chemical synapses, For these experiments, I examined a strain in which RIM expresses the Tetanus toxin light chain, which inhibits synaptic vesicle release by cleaving the fusion protein synaptobrevin (Gordus et al., 2015, Schiavo et al., 1992). Animals expressing Tetanus toxin light chain in RIM closely resembled *tdc-1* or RIM glu KO; *tdc-1* mutants, having an increased number of reversals, and shorter, slower reversals, than the wild type during local search (Figure 2-6A-C).

In summary, multiple lines of evidence indicate that the RIM chemical neurotransmitters tyramine and glutamate act together to suppress spontaneous reversals and lengthen reversals.

#### *RIM chemical transmitters increase forward locomotion speed*

RIM has a well-established role in the control of reversal frequency and length; my work showed that it also affects reversal speed (Figure 2-7A). The role of RIM in forward locomotion has not been examined. To address this issue, I measured forward locomotion speed during the local search period in RIM glu KO, *tdc-1* or RIM glu KO; *tdc-1* double mutants. Forward locomotion speed was also slightly diminished in *tdc-1* mutants, and further diminished in RIM glu KO; *tdc-1* double mutants (Figure 2-7B). Animals expressing Tetanus toxin light chain in RIM had similar changes in forward speed (Figure 2-6E). Forward locomotion speeds are highly heterogenous in different behavioral states (Ben Arous et al., 2009, Fujiwara et al., 2002 Gray et al., 2005, Hills et al., 2004, Sawin et al., 2000, Shtonda and Avery, 2006). To control for this factor, I examined locomotion speed at the transition from forward to reverse locomotion, a more uniform behavior, and observe a similar small decrease in RIM glu KO; *tdc-1* double mutants (Figure 2-7C). I conclude that RIM chemical transmitters affect the speed of both forward and reverse locomotion.

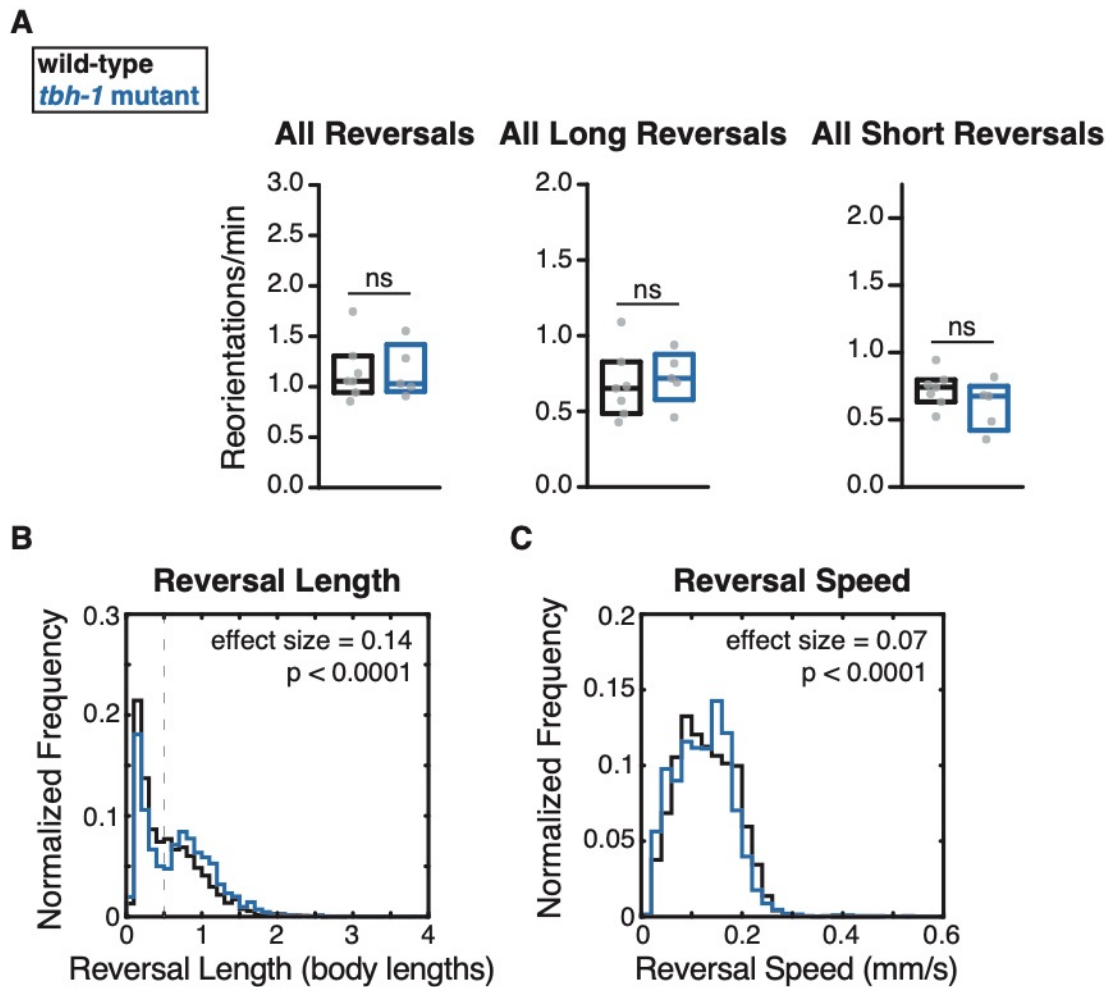


**Figure 2-5. Octopamine deficient *tbh-1* mutants exhibit normal reversal behavior during off-food foraging.**

**(A)** Average frequency of reversals during minutes 4-8 of local search. Left panel: all reversals regardless of length. Middle panel: only long reversals ( $> 0.5$  body lengths). Right panel only short reversals ( $< 0.5$  body lengths). Left panel: all reversals regardless of length. Each gray dot is 1 assay,  $n=12-15$  animals per assay. Boxes indicate median and interquartile range. ns indicates no significant difference between 2 conditions using Mann-Whitney test.

**(B)** Distributions of reversal length of all reversals over entire 45-minute recording normalized by probability. Dotted line indicates the separation of short and long reversals in the wild-type.

**(C)** Distributions of reversal speed of all reversals over entire 45-minute recording normalized by probability.

**Figure 2-5. Octopamine deficient *tbh-1* mutants exhibit normal reversal behavior during off-food foraging.**

**(A)** Average frequency of reversals during minutes 4-8 of local search. Left panel: all reversals regardless of length. Middle panel: only long reversals (> 0.5 body lengths). Right panel only short reversals (< 0.5 body lengths). Each gray dot is 1 assay, n=12-15 animals per assay. Boxes indicate median and interquartile range. ns indicates no significant difference between 2 conditions using Mann-Whitney test.

**(B)** Distributions of reversal length of all reversals over entire 45-minute recording normalized by probability. Dotted line indicates the separation of short and long reversals in the wild-type.

**(C)** Distributions of reversal speed of all reversals over entire 45-minute recording normalized by probability.

**(B)** and **(C)** n=1935 & 3139 reversal events from 5-7 assays. p is the significance of the difference of each experimental group compared to wildtype based on the Kolmogorov-Smirnov test, effect size is the D statistic.

See Methods & Appendices for further details.

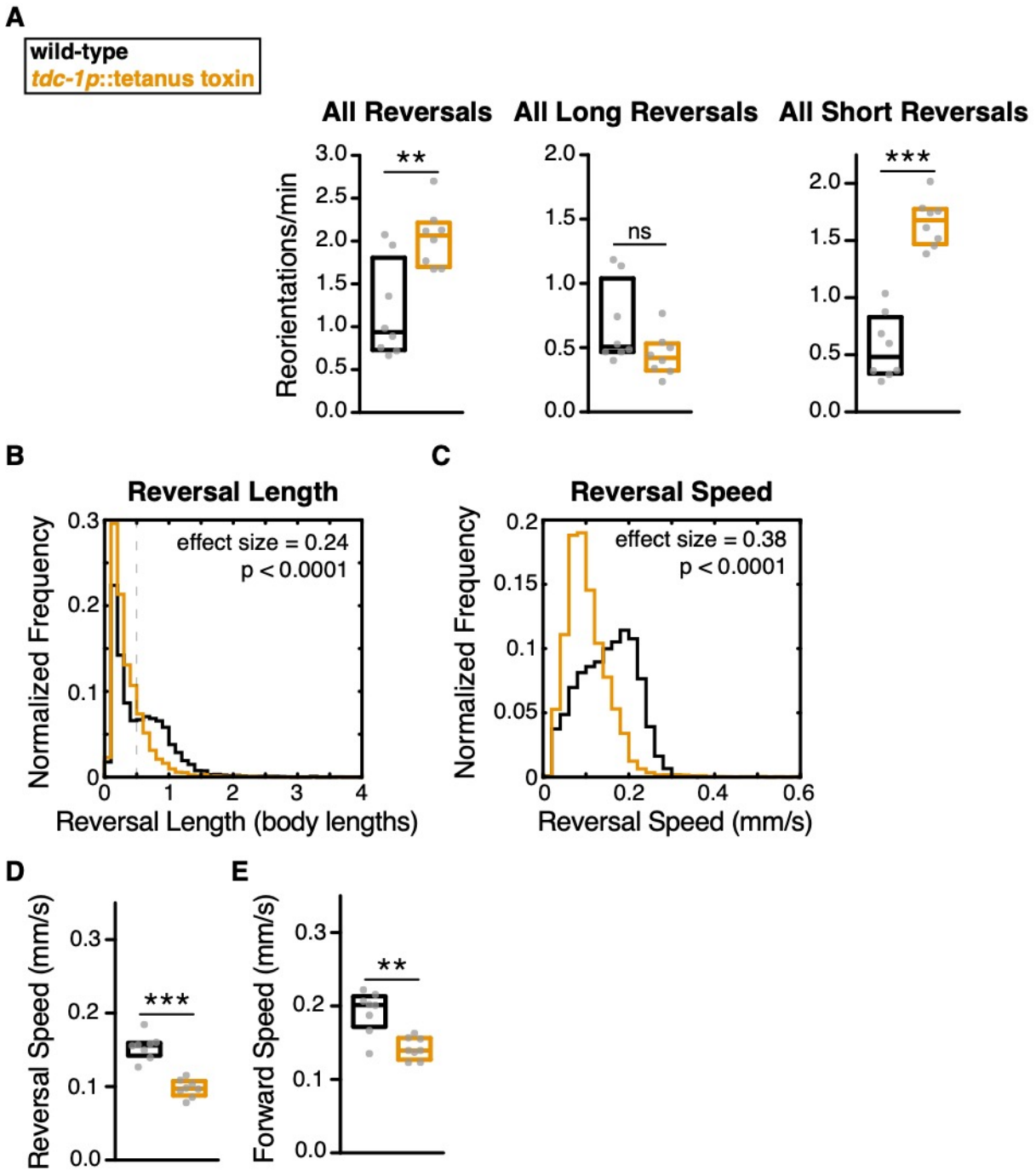


**Figure 2-6. Expressing Tetanus toxin in RIM causes defects similar to the combined RIM glutamate KO; *tdc-1* mutant.**

**Figure 2-6. Expressing Tetanus toxin in RIM causes defects similar to the combined RIM glutamate KO; *tdc-1* mutant.**

**(A)** Average frequency of reversals during minutes 4-8 of local search. Left panel: all reversals regardless of length. Middle panel: only long reversals (> 0.5 body lengths). Right panel only short reversals (< 0.5 body lengths).

**(B)** Distributions of reversal length of all reversals over entire 45-minute recording normalized by probability. Dotted line indicates the separation of short and long reversals in the wild-type.

**(C)** Distributions of reversal speed of all reversals over entire 45-minute recording normalized by probability.

**(D)** Average reversal speed during minutes 4-8 of local search.

**(E)** Average forward speed during minutes 4-8 of local search.

**(B)** and **(C)** n=3584-6268 reversal events from 8 assays. p is the significance of the difference of each experimental group compared to wildtype based on the Kolmogorov-Smirnov test, effect size is the D statistic.

**(A)**, **(D)**, & **(E)** Each gray dot is 1 assay, n=12-15 animals per assay. Boxes indicate median and interquartile range. Asterisks indicate significant difference between 2 conditions using Mann-Whitney test. ns = not significant.

See Methods & Appendices for further details.

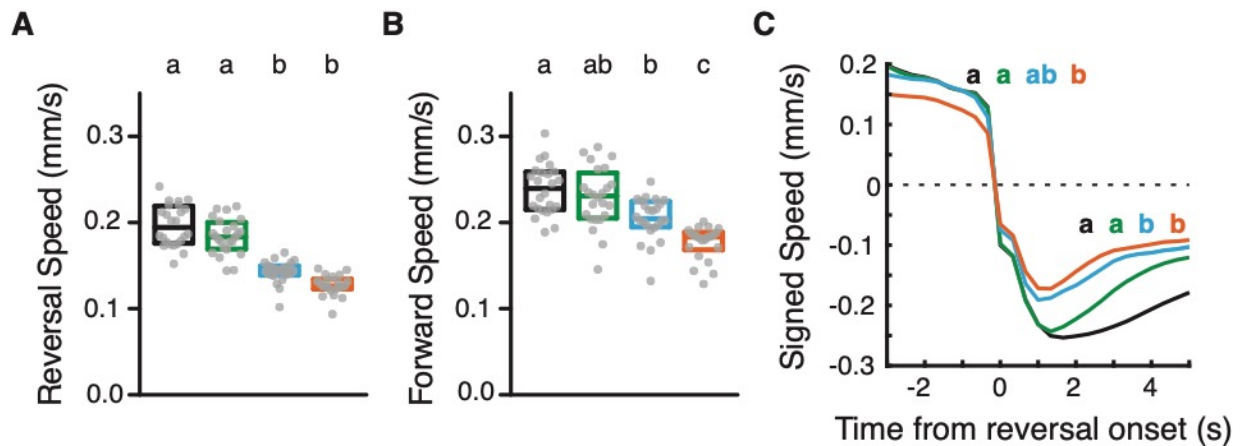


**Figure 2-7. RIM chemical synapses increase forward and reverse speed.**

**(A)** Average reversal speed during minutes 4-8 of local search.

**(B)** Average forward speed during minutes 4-8 of local search.

**(C)** Speed aligned to 3 seconds prior to reversal initiation. Different letters indicate statistical significance using a Friedman test with Dunn's multiple comparisons test.

**(A)** and **(B)** Each gray dot is 1 assay,  $n=12-15$  animals per assay. Boxes indicate median and interquartile range. Different letters indicate statistical significance using a Kruskal-Wallis test with Dunn's multiple comparisons test.

See Methods & Appendices for further details.



### *RIM glutamate may lengthen reversals by inhibiting omega turns*

In wild-type foraging behavior, most long reversals are followed by a sharp turn called an omega turn, but short reversals are not (Chalasan et al., 2007, Croll 1975, Gray et al., 2004, Huang et al., 2006, Zhao et al., 2003, Figure 2-8A). In tyramine receptor mutants, reversals coupled to omega turns (here termed reversal omegas) decrease, and in *tdc-1* mutants and tyramine receptor mutants omega turns are reduced in amplitude (Donnelly et al., 2013, Kagawa-Nagamura, 2018); in agreement with this observation, I observed a 2-fold reduction in the fraction of reversal omegas in *tdc-1* mutants (Figure 2-8B). By contrast, RIM glu KO animals maintained strong coupling of reversals to omegas at a comparable fraction to wild-type (Figure 2-8B). However, the average length of reversals coupled to omega turns was reduced in RIM glu KO mutants, consistent with the reduced length of long reversals in these mutants (Figure 2-8C). *tdc-1* mutants and double RIM glu KO; *tdc-1* mutants both coupled short reversals to omega turns (Figures 2-8C).

To quantify this effect further, I defined the median reversal length of reversal omegas for tyramine-deficient worms (~0.6 body lengths) and then found the percentage of reversal omegas for each genotype at reversal lengths surrounding this median (0.5 - 0.8 body lengths, Figures 2-8C-D). RIM glu KO animals had a higher percentage of reversal omegas at this length than all other genotypes, indicating that RIM glutamate inhibits omega turn coupling at shorter reversal lengths (Figure 2-8D) This result was robust to other reversal length cutoffs (Figure 2-9A-B).

The sharpness of omega turns is reduced in *tdc-1* mutants, but not in RIM glu KO animals (Donnelly et al., 2013, Figure 2-8E). Double RIM glu KO; *tdc-1* mutants resembled *tdc-1* single mutants (Figure 2-8E).

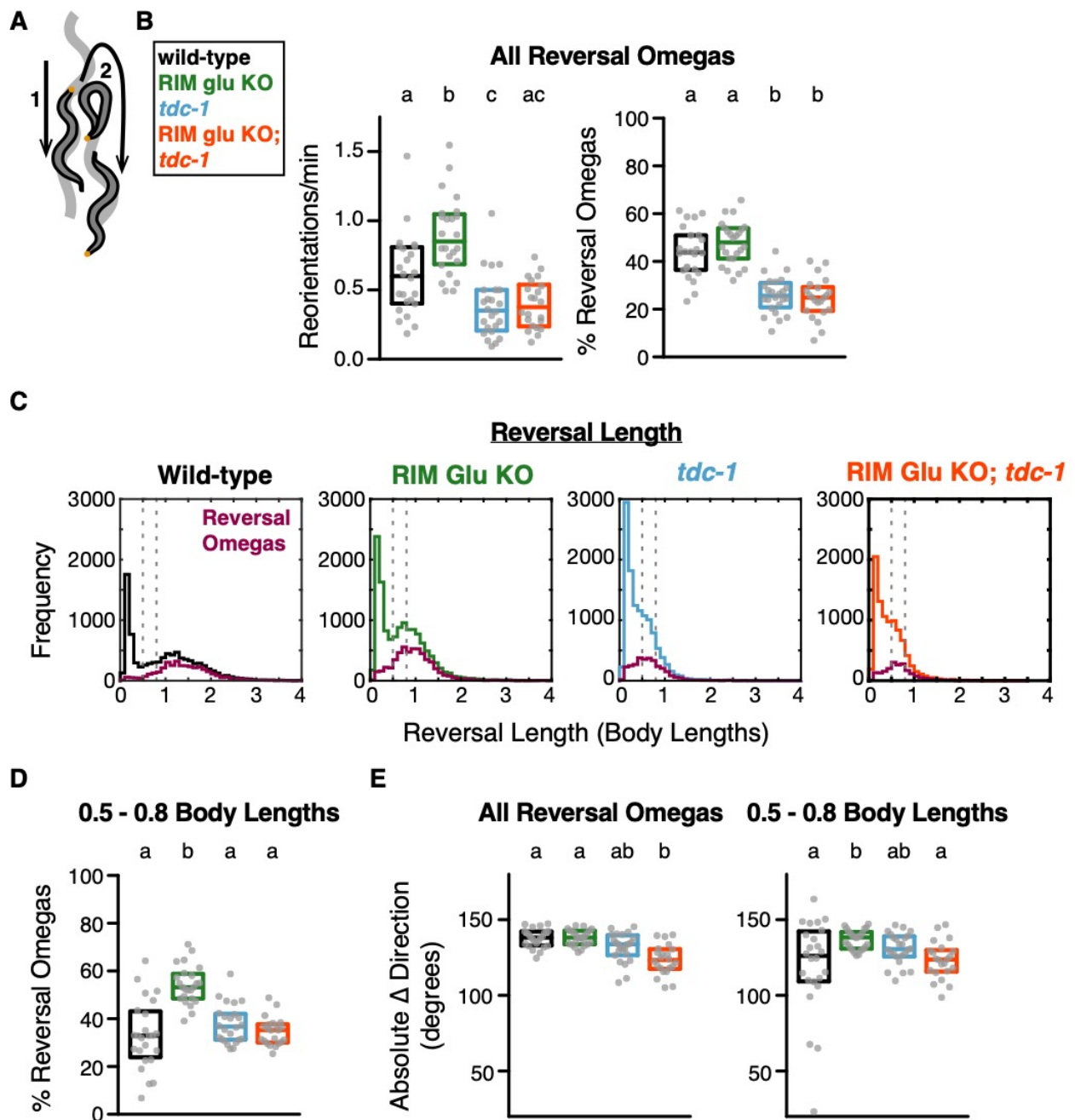


**Figure 2-8. RIM tyramine promotes long reversals coupled to omega turns; RIM glutamate inhibits coupling to omega turns.**

**Figure 2-8. RIM tyramine promotes long reversals coupled to omega turns; RIM glutamate inhibits coupling to omega turns.**

**(A)** Schematic of a reversal (1) coupled to an omega turn (2) where the nose of the worm (orange dot) touches its tail, allowing the worm to orient in a new direction. Omega turn probability increases with reversal length in wild-type worms. Redrawn from López-Cruz et al., 2019.

**(B)** Left panel: Average frequency of reversal omegas during minutes 4-8 of local search. Right panel: Percent reversal omegas during minutes 4-8 of local search; calculated by dividing the data from the left panel by the mean frequency of all reversals during this time period (see Figure 2-2B; left panel).

**(C)** Distributions of reversal length of all reversals over entire 45-minute recording. Length of reversals coupled to omega turns shown in maroon. Dotted line indicates 0.5-0.8 body lengths, a range surrounding the median length of reversals coupled to omegas of *tdc-1* mutants and *tdc-1*; RIM glu KO animals (see D). n=8851-13419 reversal events from 22-24 assays.

**(D)** Percent reversal omegas throughout 45-minute recording, only considering reversals 0.5-0.8 body lengths long (see C).

**(E)** Average change in direction after reversal omegas throughout 45-minute recording. Left panel: all omega turns coupled to reversals, regardless of length Right panel: only turns coupled to reversals 0.5-0.8 body lengths long.

**(C), (D), and (E)** Each gray dot is 1 assay, n=12-15 animals per assay. Boxes indicate median and interquartile range. Different letters indicate statistical significance using a Kruskal-Wallis test with Dunn's multiple comparisons test. See Methods for details.

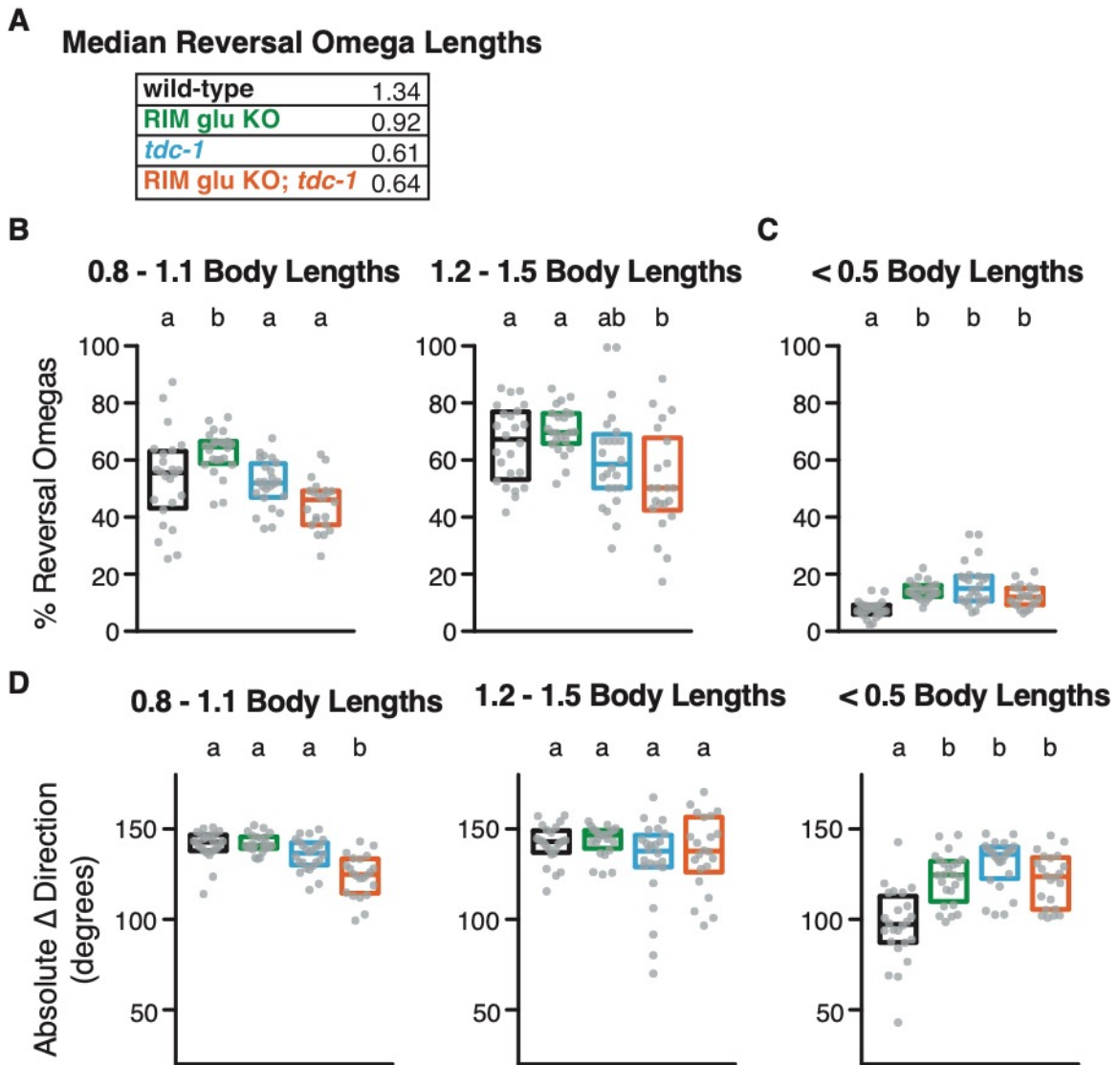


**Figure 2-9. Effects of RIM chemical synapses on reversal omegas at various reversal lengths. Supplement to Figure 2-8.**

**Figure 2-9. Effects of RIM chemical synapses on reversal omegas at various reversal lengths. Supplement to Figure 2-8.**

**(A)** Median reversal length of reversal omegas for each genotype in body lengths. The percent of reversal omegas and average change in direction was found for a 0.3 body length range around each median length. Median reversal lengths of *tdc-1* single mutants and RIM glu KO; *tdc-1* were close in value; accordingly, only 3 ranges of lengths were evaluated.

**(B)** Percent reversal omegas throughout 45-minute recording, only considering reversals 0.8-1.1 body lengths long (left) or reversals 1.2-1.5 body lengths long (right). See A.

**(C)** Percent reversal omegas throughout 45-minute recording, only considering short reversals <0.5 body lengths long.

**(D)** Average change in direction after sharp turns throughout 45-minute recording. Left: only omega turns coupled to reversals 0.8-1.1 body lengths long, middle: only omega turns coupled to reversals 1.2-1.5 body lengths long, right: only omega turns coupled to short reversals <0.5 body lengths long.

See Methods & Appendices for further details.

*Not all reversal types are modulated by RIM chemical synapses*

As an alternative classification of reversal types, I produced a scatter plot representing each reversal's length and speed (Figure 2-10). This plot reveals two potential clusters of reversals. One cluster encompasses short reversals that reach relatively high speeds; the second cluster includes a broader overall range of reversal lengths and speeds, with length and speed correlated with each other across the range. The first cluster is composed entirely of reversals that are not coupled to turns. The second cluster includes all reversal types and is dominated by longer reversals coupled to omega turns. Comparing this plot across genotypes reveals that the second large cluster is shaped by RIM chemical synapses, whereas the first small cluster is more constant and largely unaffected by RIM chemical synapses, save for a small decrease in speed in tyramine-deficient animals (Figure 2-10).

These results provide further evidence for the hypothesis that reversals are heterogenous in their neural and molecular requirements, such that RIM and tyramine are preferentially required for the execution of long reversals.

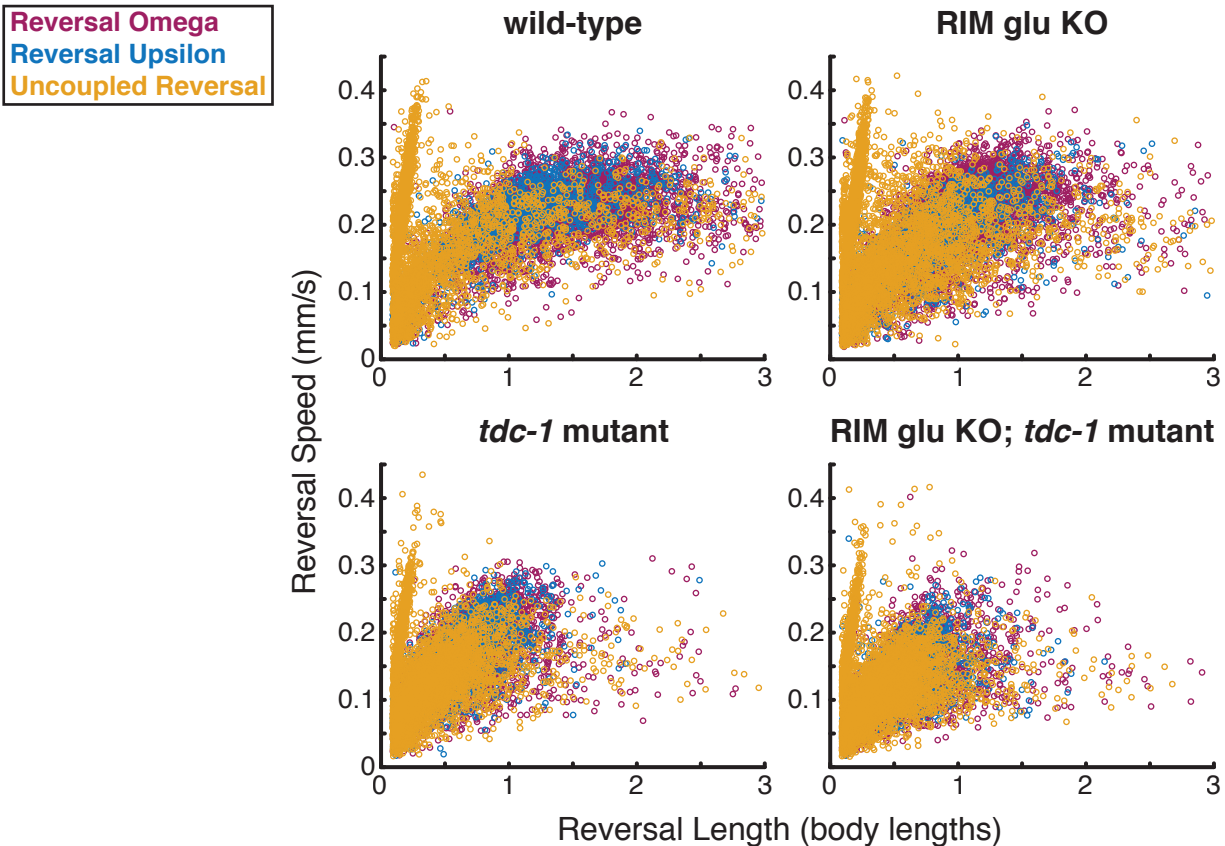


**Figure 2-10. RIM chemical synapses do not shape uncoupled, short reversals.**

Scatter plots of each reversal during 45-minute recording. Each dot is a single reversal. Top left: wild-type reversals; top right: RIM glu KO; bottom left: *tdc-1* mutant; bottom right: RIM glu KO; *tdc-1* mutant. Reversal Omega = all reversals coupled to omega turns. Reversal Upsilon = all reversals coupled to shallow epsilon turns. Uncoupled Reversal = all reversals not coupled to turns. See Methods & Appendices for further details.

## Discussion

### *The effects of RIM glutamate on reversal frequencies and features during off-food foraging*

Using a cell-specific glutamate vesicular transporter knockout, I determined that RIM glutamate reduces reversal frequencies and lengthens long reversals, potentially by inhibiting the coupling of reversals to omega turns.

My dissection of RIM glutamate sheds light on multiple features of *C. elegans* locomotion. Wild-type reversal lengths clearly fall into a bimodal distribution, confirming previous results suggesting that reversals naturally separate into two classes (Alkema et al., 2005, Gray et al., 2005, Figure 2-2B). This bimodality is not detectable in tyramine-deficient animals, either because the two classes actually merge or because the shortening of long reversals drives the two classes to overlap in my measurements. In contrast, glutamate-deficient animals maintain a bimodal distribution of reversal lengths, and glutamate appears to modulate only the length of longer reversals. Further analyses may reveal how RIM chemical synapses shape reversal distributions in greater detail.

The distinction between RIM tyramine and glutamate suggests that reversal length and reversal frequency can be regulated separately. This distinction is even clearer with genetic manipulation of gap junctions, as described in Chapter 3.

RIM tyramine has strong effects on spontaneous reversal speed, while RIM glutamate does not (Figure 2-2D). Past work has found that the slope of the rise in RIM calcium levels correlates with reversal speed; it could be interesting to determine whether a steep calcium slope promotes tyramine release (Kato et al., 2015).

RIM chemical synapses slightly increase speed during forward locomotion, suggesting an overlap between the activity of the forward locomotion circuit and the reversal circuit. Chemogenetic inhibition of other neurons in the reversal circuit—AVA and AIB—decreases forward speed by 50% and 25%, respectively, apparently larger effects than those of RIM chemical synapses (Pokala et al., 2014). My results provide further evidence that the function of the forward and reversal circuits overlap.

Overall, I revealed that RIM glutamate works with RIM tyramine to inhibit reversal frequency and lengthen reversals and that RIM glutamate may antagonize RIM tyramine by inhibiting the coupling of reversals to omega turns (Figure 2-11). However, uncovering the effects of RIM glutamate on spontaneous reversal behavior does not reconcile previous findings that indicate that RIM can also promote reversal frequency.



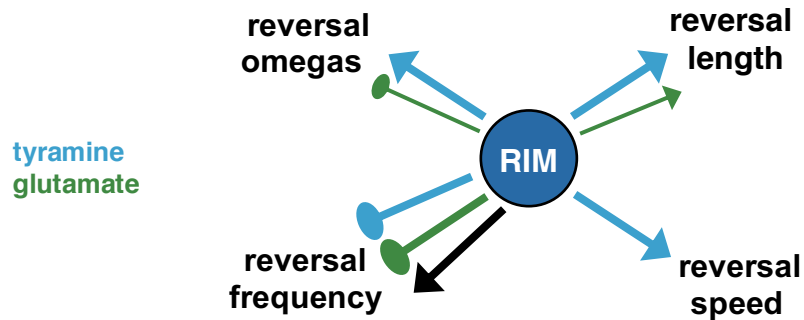


**Figure 2-11. Effects of RIM chemical synapses on reversal behavior.**

A schematic summarizing the results of this chapter: Triangle arrow heads indicate that a behavioral parameter is promoted. Circle arrow heads indicate that a behavior is inhibited. Black arrow indicates an effect of RIM on reversal behavior not explained by RIM chemical synapse data.

*RIM co-transmission and variation in reversal behavior across contexts*

RIM chemical synapses decrease the fidelity with which animals suppress reversals in response to an appetitive odor stimulus and thus generate behavioral variability (Gordus et al., 2015). The results in this chapter, along with previous work on tyramine, indicate that during spontaneous behavior RIM chemical synapses predominately act to prolong the forward state—inhibiting reversals—and to prolong the reversal state—lengthening reversals. This dual role for RIM during foraging suggests that RIM may generate variability by promoting either the forward state or the reversal state in response to complex inputs from internal states and external stimuli.

I speculate that RIM glutamate works cooperatively with RIM tyramine to lengthen spontaneous reversals but may also inhibit the omega turns that follow most reversals. In this model, co-transmission from the RIM interneuron can generate behavioral variability by multiple mechanisms.

## Future Directions

### *What are the targets of RIM glutamate?*

I have found that RIM glutamatergic signaling inhibits reversal initiation and lengthens reversals, but the cellular and molecular targets of RIM glutamate remain to be determined. The forward command neuron AVB receives chemical synapses from RIM, and tyramine extends reversal length by inhibiting AVB through the tyramine-gated chloride channel LGC-55 (Cook et al., 2019, Pirri et al., 2009, White et al., 1986, Figure 1-1). AVB also expresses the glutamate-gated chloride channel AVR-14, as well the AMPA type glutamate-gated cation channels GLR-1 and GLR-5 (Brockie et al., 2001, Hart et al., 1995, Maricq et al., 1995, Taylor et al., 2019). Thus, one possibility is that RIM glutamate inhibits AVB through AVR-14.

The reversal command neuron AVA is also post synaptic to RIM and expresses genes for both AMPA and NMDA type glutamate-gated cation channels, such as GLR-1, GLR-5, and NMR-2, as well as the glutamate-gated chloride channels AVR-14 and GLC-4 (Cook et al., 2019, Brockie et al., 2001, Hart et al., 1995, Katz et al., 2019, Maricq et al., 1995, Taylor et al., 2019, White et al., 1986, Figure 1-1). Another possibility is that RIM glutamate stabilizes the reversal state by depolarizing AVA through GLR-1, GLR-5, and NMR-2.

The results of this chapter also indicate that RIM glutamate inhibits coupling of reversals to omega turns. The interneuron AIB, which promotes omega turns and has bidirectional synapses with RIM, is an interesting candidate to mediate this effect (Figure 1-1). While RIM and AIB are both active during reversals, a competition or shift between RIM-dominated and AIB-dominated circuits may be associated with the shift from reversals to turns (Gordus et al., 2015, Kato et al., 2015). AIB receives chemical synapses from RIM and expresses the excitatory glutamate receptors GLR-1, GLR-2, GLR-5, the metabotropic glutamate receptor MGL-2, and the inhibitory glutamate receptors AVR-14 and GLC-2 (Brockie et al., 2001, Chalasani et al., 2007, Cook et al., 2019, Dillon et al., 2015, Kang and Avery 2009, Katz et al., 2019, Maricq et al., 1995, Piggott et al., 2011, Taylor et al., 2019, White et al., 1986, Zou et al., 2018, Figure 1-1). I speculate that RIM glutamate inhibits AIB through AVR-14 and GLC-2 during spontaneous reversal behavior.

I also found that RIM glutamate has a modest effect on increasing reversal length. I speculate that RIM glutamate lengthens reversals by inhibiting AIB, decreasing the likelihood that AIB-dominated circuits dominate and lengthening the reversal state. This hypothesis could be tested by silencing AIB in RIM glu KO animals. Additionally, cell-specific knockouts of different glutamate receptors may help to elucidate the major targets of RIM glutamate.

### *How are RIM glutamate and tyramine co-transmitted?*

The results of this chapter indicate that RIM glutamate and RIM tyramine differentially affect *C. elegans* locomotion, but this conclusion is based on the assumption that EAT-4 (VGLUT) acts solely to release glutamate at RIM chemical synapses. However, it is possible that EAT-4 (VGLUT) has other molecular or cell-biological interactions at the synapse and could affect tyramine release (for example by vesicular synergy, as described in Chapter 1). Further study of proteins required for synaptic vesicle and dense core vesicle release is required to determine whether glutamate and tyramine are co-released from RIM. Through analysis of wild-type RIM EAT-4 (VGLUT) and RIM CAT-1 (VMAT) exo- and endocytosis dynamics, I have begun to elucidate the nature of RIM co-transmission (see Chapter 4).

## CHAPTER 3: RIM gap junctions are bidirectional regulators of reversal frequency

### Introduction

The results of the previous chapter and work from others show that RIM chemical synapses decrease spontaneous reversal initiation. However, work from our lab and others has also shown that RIM is active during reversals, and that stimulating RIM directly via optogenetics promotes reversals (Gordus et al., 2015, Guo, Hart, and Ramanathan, 2009, Kato et al., 2015, López-Cruz et al., 2019). Thus, optogenetics reveals a cryptic ability of RIM to induce reversals that is opposite to its basal effect of inhibiting reversals.

In the previous chapter, I demonstrated that RIM chemical synapses decrease spontaneous reversal frequency during local search, but not global search. This observation suggests that RIM's regulation of reversal behavior changes between the two behavioral states (Figure 2-3A). However, this result contrasts with earlier conclusions from optogenetic stimulation of RIM, which showed that RIM robustly evokes reversals during both local and global search (López-Cruz et al., 2019). That result suggested that RIM remains coupled to the reversal circuit in both behavioral states. In this respect, RIM contrasts with the sensory neuron ASK, which can efficiently drive reversals upon optogenetic stimulation in local search, but not during the global search state (López-Cruz et al., 2019).

In this chapter, I further probe RIM across behavioral states using optogenetic stimulation and expand my analysis to include RIM gap junctions. In addition to its chemical synapses, RIM forms gap junctions with five classes of neurons (Cook et al., 2019, White et al., 1986, Figure 1-1). Notably, RIM has numerous gap junctions with the AVE and AVA reversal command neurons and with AIB neurons that promote reversals and omega turns. These neurons are all active during reversal states, consistent with a coupled function. RIM also forms gap junctions with AIY interneurons that promote forward locomotion, and RIS neurons that promote pausing and sleep (Steuer Costa et al., 2019, Tsalik and Hobert, 2003, Turek et al., 2013, Wakabayashi et al., 2004). Thus, neurons that share gap junctions with RIM represent three different locomotion states—reversals, pauses, and forward locomotion.

Invertebrate gap junctions are made up of subunits called innexins, which assemble as homo- or heteromers of eight subunits on each of the two cells connected by a gap junction (Burendei et al., 2020, Oshima et al., 2016). RIM neurons express the innexin UNC-9, one of the most widely expressed neuronal and muscle innexins in *C. elegans*, among other innexins (Bhattacharya, et al., 2019). Genetic studies have demonstrated that *unc-9* function is modified by the stomatin-like protein encoded by *unc-1* (Chen et al., 2007). *unc-9* mutants are highly uncoordinated, precluding their direct use in behavioral assays, but they can be inactivated in a cell-specific fashion by expression of the dominant negative allele *unc-1(n494)* (Brenner 1974, Jang et al., 2017, Park and

Horvitz, 1986). Using this tool to specifically knock down gap junctions in RIM, I ask how RIM's chemical synapses and gap junctions interact in reversal behavior.

The results of this chapter show that optogenetic stimulation of RIM evokes long reversals coupled to omega turns over all other reversal types, regardless of stimulation protocol or behavioral state. I provide evidence that the RIM-evoked reversals are intrinsically stereotyped in duration, with characteristic dynamics that might relate to the global activity states observed in whole brain calcium imaging. In addition, I show that RIM chemical synapses are essential regulators of reversal parameters such as length and speed under all conditions. By contrast, RIM gap junctions are required for RIM-dependent reversals during global search but are less important during local search. By comparing their effects on spontaneous and optogenetically induced reversals, I infer that RIM gap junctions bidirectionally regulate reversal frequency.

## Results

### *Optogenetic RIM activation induces a stereotyped reversal-omega behavior*

In the previous chapter I showed that RIM chemical synapses alter reversal frequency during local search, but not global search. The change from local to global search requirements could result from a decrease in spontaneous RIM activity during global search, a decrease in the fidelity of RIM chemical synapses during global search, a decrease in the overall activity of the reversal circuit, or some combination of these processes. Previous work has shown that optogenetic activation of the red-shifted channelrhodopsin ReaChR in RIM evokes reversals during both local and global search states (Lin et al., 2013, López-Cruz et al., 2019), suggesting that the diminished effects of RIM chemical synapses during global search may be due to a decrease in RIM activity.

To better understand these responses and the role of RIM chemical synapses across behavioral states, I used optogenetic methods that elicited robust and quantitative behaviors to defined stimuli. I first varied the optogenetic stimulus time, providing light pulses of 5 s, 10 s, 20 s, and 30 s ( $\sim 45 \mu\text{W}/\text{mm}^2$  light, 50% duty cycle, Figure 3-1A). As previously reported, the majority of all animals performed reversals throughout the light pulse, during both local and global search periods (Figure 3-1B-E). Two additional features were uncovered by close examination; a transient dip in the fraction of animals performing reversals approximately 10-15 s into the longer light pulses, and a transient suppression of reversals after the end of the light pulse, particularly after long pulses and during local search.

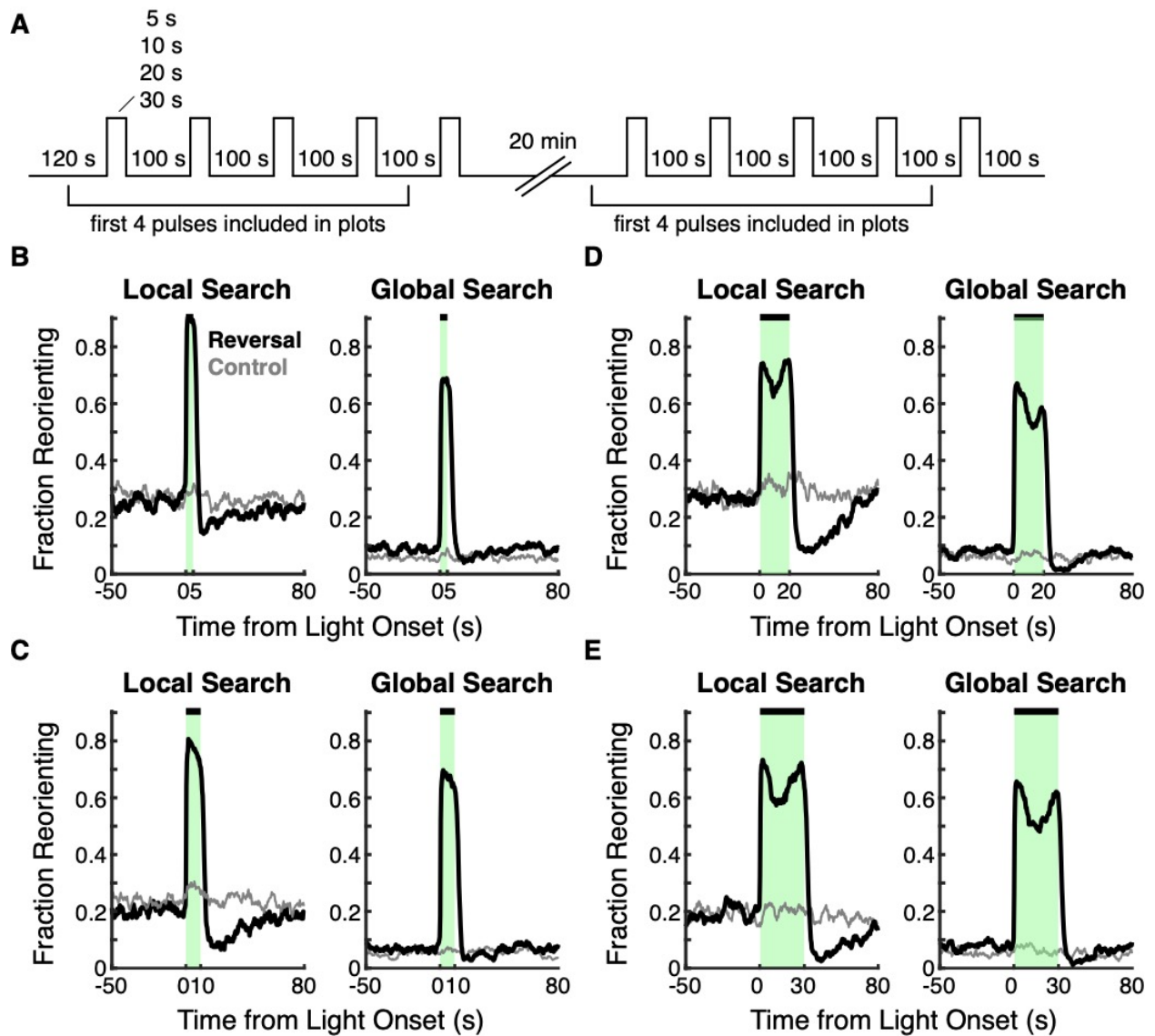


**Figure 3-1. Direct stimulation of RIM evokes reversals throughout the light pulse across off-food foraging states regardless of pulse time.**

**Figure 3-1. Direct stimulation of RIM evokes reversals throughout the light pulse across off-food foraging states regardless of pulse time.**

**(A)** Schematic of stimulation protocol. Length and intensity of light pulses was constant throughout each experiment. Light intensity was  $\sim 45\mu\text{W}/\text{mm}^2$  at a 50% duty cycle.

**(B)** Fraction of animals reversing during a 5-s light pulse, showing 50 s before and after pulse.

**(C)** Fraction of animals reversing during a 10-s light pulse, showing 50 s before and after pulse.

**(D)** Fraction of animals reversing during a 20-s light pulse, showing 50 s before and after pulse.

**(E)** Fraction of animals reversing during a 30-s light pulse, showing 50 s before and after pulse.

**(A) – (E)** Animals with (black) or without (gray) retinal pre-treatment. Left: aligned pulses during local search. Right: aligned pulses during global search. Green shading/black bar indicate time when light was on. Data from all full tracks included, regardless of the locomotor state of the animal at the time of light onset or response time.

See Methods & Appendices for further details.



To understand the effects of optogenetic manipulation further, I categorized the reorientations induced by light in further detail. First, I asked which specific reorientation types are evoked by RIM depolarization (long reversals, short reversals, or turns). Between 60-80% of all reorientations elicited by the optogenetic stimulation of RIM were long reversals ( $>0.5$  body length) coupled to omega turns (Figure 3-2). The long-reversal omega sequence was elicited during both local search and global search states, and at a variety of stimulus durations. I conclude that RIM stimulation preferentially induces long reversal-omega behavior.

Next, to understand the dynamics of behavior, I examined the responses of individual animals during the light pulse, instead of the average population response. This analysis uncovered characteristic behavioral dynamics, with instructive differences depending on the duration of the optogenetic stimulus (Figure 3-3).

Upon RIM stimulation, approximately half of all animals began to reverse within 3 s of light onset (Figure 3-3A-G, Table 3-1). Among these animals, the fraction reversing peaked within 2 s of light onset. This class of behaviors will be called short-onset reversals. When RIM was stimulated for 5 s, the short-onset reversals terminated immediately upon light offset, and omega turns occurred at light offset with the stereotyped duration ( $\sim 3$  s) noted in previous studies (Figure 3-3A-B, Table 3-1, Ghosh et al., 2012,).

When RIM was stimulated for 10 to 30 s, the short-onset reversals lasted for  $\sim 6-9$  s, followed by a transition to omega turn behavior (Figure 3-3C-H, Table 3-1). The omega turns that occurred during the light pulse were about twice as long as those that occurred at light offset. The burst of turning behavior was sometimes followed by a brief forward movement or a reorientation other than a long reversal omega. Subsequently, most animals generated additional long reversal omegas (Figure 3-3C-H, Table 3-1). Reversals that were in progress at the light offset terminated promptly when the light pulse ended and were followed by omega turns that peaked within 2 s of light offset.

A fraction of animals did not respond to RIM optogenetic stimulation; I did not determine whether response probability was reproducible in a single animal or stochastic.

These results suggest that reversals and turns elicited by RIM stimulation have characteristic dynamics that are partly independent of the stimulus duration. The fact that RIM-evoked reversals end abruptly upon light offset indicates that RIM is required to sustain, as well as initiate, reversals. However, the fact that RIM-evoked reversals terminate after 6-9 s when light is still on indicates that RIM is not sufficient to sustain a long reversal indefinitely; the reversal apparently must be interrupted by an omega turn before another reversal can begin. Omega turns are favored upon light offset but can also occur when light is on for long durations. Together, it appears that RIM activates a long reversal - omega circuit with intrinsic internal dynamics.

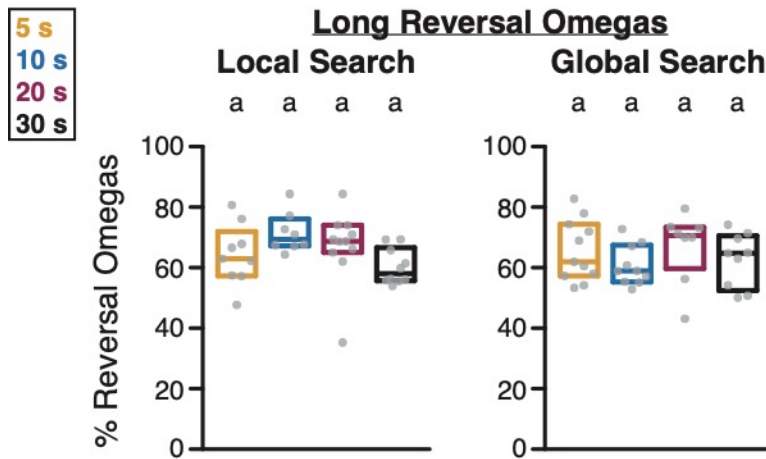


**Figure 3-2. Long reversal omegas are evoked upon RIM activation. Supplement to Figures 3-1 & 3-3.**

The percent of long reversals omegas evoked out of all evoked reversal behaviors that occur during the light pulse. Percent is calculated by dividing the mean fraction of animals performing a long reversal omega from 1 second after light onset through 1 second before light offset by the mean fraction of animals doing any reversal behavior during that time. Data from all full tracks included, regardless of the locomotor state of the animal at the time of light onset or response time. Each gray dot is 1 assay, n=12-15 animals per assay. Boxes indicate median and interquartile range. Different letters indicate statistical significance using a Kruskal-Wallis test with Dunn's multiple comparisons test. See Methods & Appendices for further details.

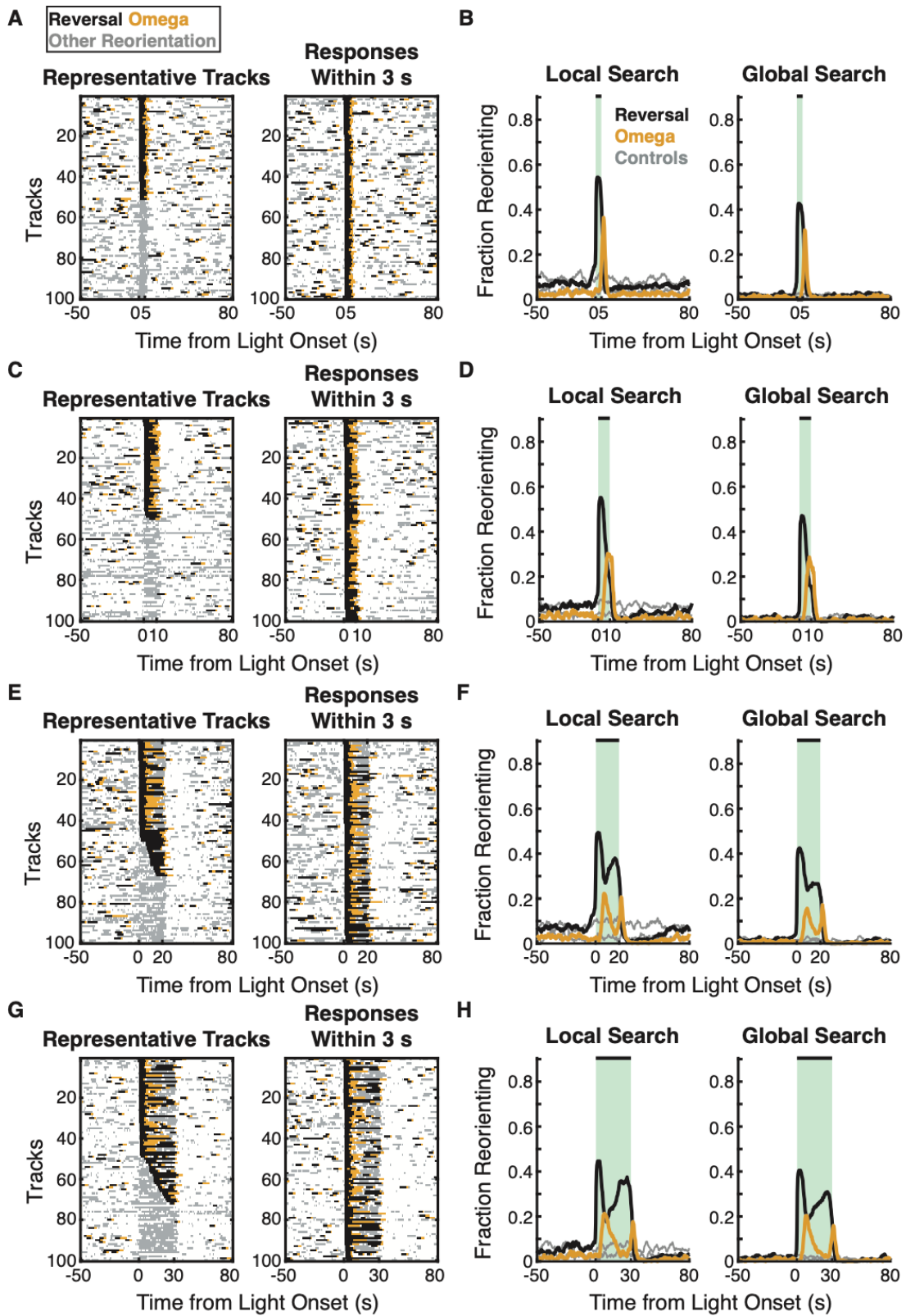


**Figure 3-3. RIM stimulation evokes long reversals of characteristic duration, followed by coupled omega turns.**

**Figure 3-3. RIM stimulation evokes long reversals of characteristic duration, followed by coupled omega turns.**

**(A)** Left: ethogram of 100 randomly chosen tracks in which animals were not performing a long reversal omega 1 s before light onset during a 5-s light pulse, showing 50 s before and after pulse. Right: ethogram of 100 randomly chosen tracks during which animals were not performing a long reversal omega 1 s before light onset and responded within 3 s of light onset. White indicates time animals were moving forward.

**(B)** Fraction of animals performing a long reversal coupled to a sharp turn during a 5-s light pulse, showing 50 s before and after pulses, including data from all full tracks.

**(C)** Left: ethogram of 100 randomly chosen tracks in which animals were not performing a long reversal omega 1 s before light onset during a 10-s light pulse, showing 50 s before and after pulse. Right: ethogram of 100 randomly chosen tracks during which animals were not performing a long reversal omega 1 s before light onset and responded within 3 s of light onset. White indicates time animals were moving forward.

**(D)** Fraction of animals performing a long reversal coupled to a sharp turn during a 10-s light pulse, showing 50 s before and after pulses, including data from all full tracks.

**(E)** Left: ethogram of 100 randomly chosen tracks in which animals were not performing a long reversal omega 1 s before light onset during a 20-s light pulse, showing 50 s before and after pulse. Right: ethogram of 100 randomly chosen tracks during which animals were not performing a long reversal omega 1 s before light onset and responded within 3 s of light onset. White indicates time animals were moving forward.

**(F)** Fraction of animals performing a long reversal coupled to a sharp turn during a 20-s light pulse, showing 50 s before and after pulses, including data from all full tracks.

**(G)** Left: ethogram of 100 randomly chosen tracks in which animals were not performing a long reversal omega 1 s before light onset during a 30-s light pulse, showing 50 s before and after pulse. Right: ethogram of 100 randomly chosen tracks during which animals were not performing a long reversal omega 1 s before light onset and responded within 3 s of light onset. White indicates time animals were moving forward.

**(H)** Fraction of animals performing a long reversal coupled to a sharp turn during a 30-s light pulse, showing 50 s before and after pulses, including data from all full tracks.

**(B), (D), (F), & (H)** Animals with (black and orange) or without (gray) all-trans retinal pre-treatment. Data from all full tracks included, regardless of the locomotor state of the animal at the time of light onset or response time. Left: aligned pulses during local search. Right: aligned pulses during global search. Green shading/black bar indicate time when light was on.

See Methods & Appendices for further details.

**Table 3-1. Quantification of evoked reversal omega parameters: All Tracks.**

Analysis of curves from Figure 3-2B, D, F, & H, which include data from all full tracks, regardless of the locomotor state at the time of light onset or response time. Duration is the width of each curve at its half-height. See Methods & Appendices for further details.

<b>Reversals</b>						
<b>Local Search</b>				<b>Global Search</b>		
Pulse Time (s)	Reversal Peak (fraction reorienting)	Reversal Duration (s)	Reversal Peak Location (s from light onset)	Reversal Peak (fraction reorienting)	Reversal Duration (s)	Reversal Peak Location (s from light onset)
5	0.54	5.77	1.33	0.43	5.81	1.33
10	0.55	7.07	1.67	0.47	6.91	2.00
20	0.50	8.19	2.00	0.42	9.05	2.00
30	0.45	6.84	1.67	0.40	7.90	1.67
<b>Omegas</b>						
<b>Local Search</b>						
Pulse Time (s)	First Omega Peak (fraction reorienting)	First Omega Duration (s)	First Omega Peak Location (s from light onset)	Second Omega Peak (fraction reorienting)	Second Omega Duration (s)	Second Omega Peak Location (s from light onset)
5	0.35	3.07	6.67			
10	0.30	5.77	8.00			
20	0.23	5.99	7.00	0.21	3.33	21.67
30	0.21	5.38	7.33	0.18	3.99	31.67
<b>Global Search</b>						
Pulse Time (s)	First Omega Peak (fraction reorienting)	First Omega Duration (s)	First Omega Peak Location (s from light onset)	Second Omega Peak (fraction reorienting)	Second Omega Duration (s)	Second Omega Peak Location (s from light onset)
5	0.31	2.71	6.67			
10	0.29	7.47	8.33			
20	0.16	7.26	8.67	0.17	2.71	21.67
30	0.20	6.76	8.33	0.16	3.96	31.00

These initial experiments showed similar effects of RIM stimulation on local and global search at a single light stimulus intensity with different durations. As an alternative way to vary the RIM input to behavior, I provided weaker optogenetic stimuli by using a 5% duty cycle (instead of 50%) and varied the light intensity from  $\sim 5 \mu\text{W}/\text{mm}^2$  light to  $\sim 45 \mu\text{W}/\text{mm}^2$  across the experiment (Figure 3-4A). The response to light was dose-dependent, with a marginally significant response at  $\sim 5 \mu\text{W}/\text{mm}^2$  during local search and strong responses at  $\sim 25 \mu\text{W}/\text{mm}^2$  and  $\sim 45 \mu\text{W}/\text{mm}^2$ . The responses at  $\sim 45 \mu\text{W}/\text{mm}^2$  and a 5% duty cycle persisted throughout the light stimulus during both local and global search and resembled those at the 50% duty cycle in the earlier experiments (Figures 3-4B-G, 3-5; compare to Figures 3-1D, 3-3E-F).  $\sim 25 \mu\text{W}/\text{mm}^2$  and  $\sim 45 \mu\text{W}/\text{mm}^2$  stimuli mostly evoked long reversal-omega sequences with similar dynamics to those evoked by the stronger light stimulus (Figure 3-5).

These results suggest that the behavioral response to RIM stimulation is saturated across this optogenetic range. Moreover, they imply that the failure to elicit reversals in 100% of animals is either technical (e.g. variation in transgene expression between animals), or due to transient differences in the animal's circuit state that make it refractory to RIM activation.

The 5% duty cycle;  $\sim 45 \mu\text{W}/\text{mm}^2$  pulses were used for all subsequent analyses.

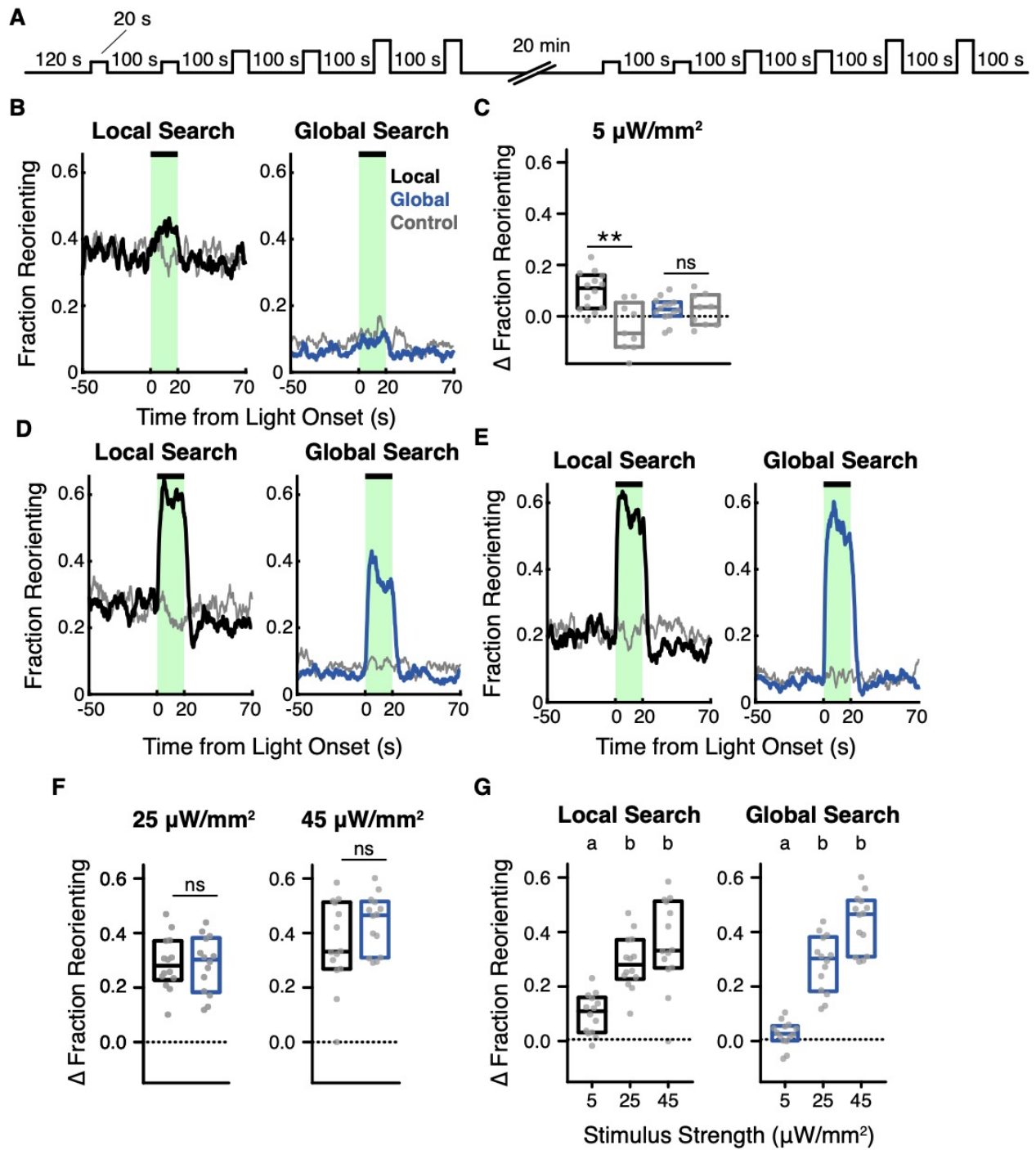


**Figure 3-4. Effects of stimulus strength and behavioral state on optogenetically-induced reversals.**

**Figure 3-4. Effects of stimulus strength and behavioral state on optogenetically-induced reversals.**

**(A)** Schematic of stimulation protocol. Stimulation time was always 20 s and intensity increased within each experiment. Light intensity of first 2 pulses is  $\sim 5\mu\text{W}/\text{mm}^2$ , followed by 2 pulses at  $\sim 25\mu\text{W}/\text{mm}^2$ , followed by 2 pulses at  $\sim 45\mu\text{W}/\text{mm}^2$ . This light titration train was executed once during local search and once during global search. A 5% duty cycle was used for all light pulses.

**(B)** Fraction of animals performing reversal during a  $5\mu\text{W}/\text{mm}^2$  light pulse, showing 50 s before and after pulse.

**(C)** Average change in the fraction of animals reversing during a  $5\mu\text{W}/\text{mm}^2$  light pulse while in local search (black) and global search (blue) compared to controls not fed all-trans retinal in the respective behavioral state (gray). Note: x-axis extended compared to other figures from -0.15 to -0.185 to fit one data point.

**(D)** Fraction of animals performing a reversal during a  $25\mu\text{W}/\text{mm}^2$  light pulse, showing 50 s before and after pulse.

**(E)** Fraction of animals performing a reversal during a  $45\mu\text{W}/\text{mm}^2$  light pulse, showing 50 s before and after pulse.

**(F)** Average change in the fraction of animals reversing during the light pulse during local search (black) and global search (blue). Left:  $25\mu\text{W}/\text{mm}^2$  light, right:  $45\mu\text{W}/\text{mm}^2$  light.

**(G)** Data from (F) compared across stimulation strengths. Left: local search; right: global search. Different letters indicate statistical significance using a Kruskal-Wallis test with Dunn's multiple comparisons test.

**(B), (D), & (E)** Animals with (black and blue) or without (gray) all-trans retinal pre-treatment. Left: aligned pulses during local search. Right: aligned pulses during global search. Green shading/black bar indicate time when light was on. Data from all full tracks included, regardless of the locomotor state of the animal at the time of light onset or response time.

**(C) & (F)** Asterisks indicate significant difference between 2 conditions using Mann-Whitney test. ns = not significant.

**(C), (F) & (G)** Change in fraction reorienting is calculated by taking the average over seconds 2-19 of the pulse and subtracting the average taken over 12 s before the pulse. All full tracks included. Data from all full tracks included, regardless of the locomotor state of the animal at the time of light onset or response time. Each gray dot is 1 assay,  $n=12-15$  animals per assay. Boxes indicate median and interquartile range.

See Methods & Appendices for further details.



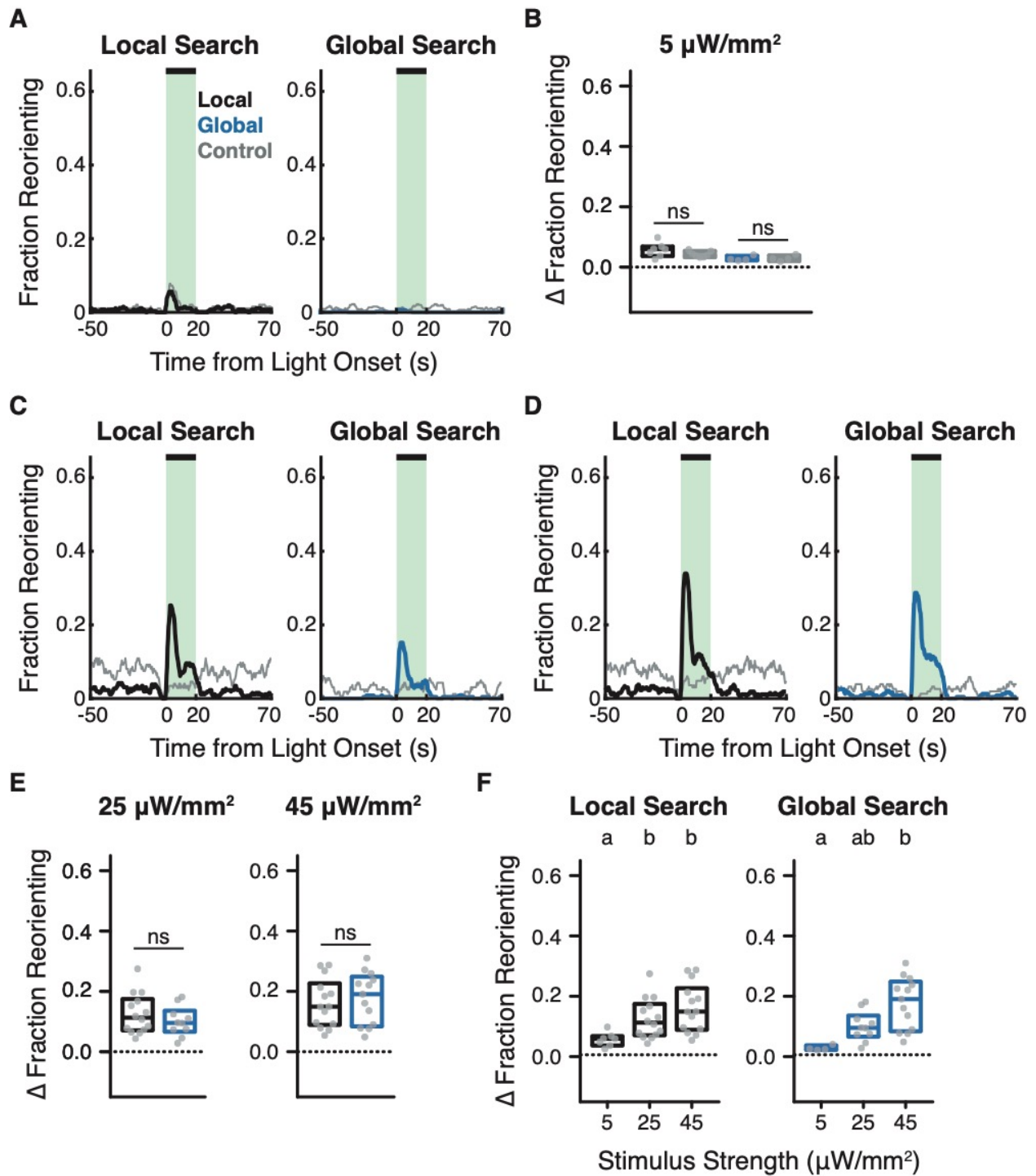


**Figure 3-5. Effects of stimulus strength and behavioral state on optogenetically-induced reversal omegas. Supplement to Figure 3-4.**

**Figure 3-5. Effects of stimulus strength and behavioral state on optogenetically-induced reversal omegas. Supplement to Figure 3-4.**

**(A)-(F)** Include data only from animals not performing long reversal omegas during the 1 s before the light pulse and within 3 s of light onset.

**(A)** Fraction of animals performing an evoked long reversal omega during a 5  $\mu\text{W}/\text{mm}^2$  light pulse, showing 50 s before and after pulse.

**(B)** Average change in the fraction of animals performing an evoked long reversal omega during a 5  $\mu\text{W}/\text{mm}^2$  light pulse while in local search (black) and global search (blue) compared to controls not fed all-trans retinal in the respective behavioral state (gray).

**(C)** Fraction of animals performing an evoked long reversal omega during a 25  $\mu\text{W}/\text{mm}^2$  light pulse, showing 50 s before and after pulse.

**(D)** Fraction of animals performing an evoked long reversal omega during a 45  $\mu\text{W}/\text{mm}^2$  light pulse, showing 50 s before and after pulse.

**(E)** Average change in the fraction of animals performing an evoked long reversal omega during 25  $\mu\text{W}/\text{mm}^2$  (left) and 45  $\mu\text{W}/\text{mm}^2$  (right) light pulses while in local search (black) and global search (blue).

**(F)** Average change in the fraction of animals performing an evoked long reversal omega while in local search (black) and global search (blue) across stimuli strengths. Different letters indicate statistical significance using a Kruskal-Wallis test with Dunn's multiple comparisons test.

**(A), (C), & (D)** Animals with (black and blue) or without (gray) all-trans retinal pre-treatment. Left: aligned pulses during local search. Right: aligned pulses during global search. Green shading/black bar indicate time when light was on.

**(B) & (E)** ns indicates no significant difference between 2 conditions using Mann-Whitney test.

**(B), (E), & (F)** Change in fraction reorienting is calculated by taking the average over seconds 2-19 of the pulse and subtracting the average taken over 12 s before the pulse. Each gray dot is 1 assay, n=12-15 animals per assay. Boxes indicate median and interquartile range.

See Methods & Appendices for further details.

*RIM chemical synapses do not inhibit RIM-evoked reversals, but do affect their length and speed*

In the last chapter, I showed that RIM chemical synapses inhibit spontaneous reversal initiation and extend the length of reversals during local search behavior. While these results provide insight into how RIM chemical synapses function within the context of endogenous circuit activity, they do not reveal how RIM chemical synapses affect behavior at the time of RIM depolarization. Additionally, it remained unclear why RIM chemical synapses do not affect reversal frequency during global search. In order to better understand how RIM chemical synapses organize reversal behavior upon RIM activation across behavioral states, I optogenetically stimulated RIM in RIM glu KO animals, *tdc-1* mutants, and double RIM glu KO; *tdc-1* mutants. Remarkably, disrupting RIM glutamatergic and tyraminerpic signaling did not alter the frequency of optogenetically-evoked reversals, regardless of behavioral state (Figure 3-6A-B). Thus, in contrast to their effect on spontaneous reversal frequency, RIM chemical synapses do not inhibit optogenetically-induced reversals. This result suggests that the effects of RIM chemical synapses on reversal frequency during local search may be dependent on an endogenous circuit state that is disrupted by depolarizing RIM on the timescale of seconds.

RIM chemical synapses promote spontaneous long reversal omegas, which are the most common reversal-type evoked upon RIM activation. Thus, animals deficient in RIM chemical synapses might have been deficient in their ability to execute long reversal omegas upon RIM activation. This was not the case: disruption of RIM chemical synapses did not alter long reversal omega induction upon RIM activation (Figure 3-7A-B).

Next, I examined whether RIM chemical synapses are still required to promote reversal length and speed during optogenetic stimulation of RIM by finding the length and speed of short-onset long reversal omegas. I found that *tdc-1* mutants had shorter reversal lengths than wild-type, with a stronger effect during global search than local search (Figure 3-6C). The effects of the RIM glu KO on length were not significant, and the double RIM glu KO; *tdc-1* mutants resembled *tdc-1*. RIM glu KO animals had slower reversals than wild-type, with a stronger effect during global search (Figure 3-6D). *tdc-1* mutant and double RIM glu KO; *tdc-1* mutant reversals were slower than wild-type during both local and global search. While control animals that were not pre-treated with all-trans retinal did not exhibit induced reversals or turns in response to light, the spontaneous reversal omegas of control animals had reversal length and speed deficits similar to those of evoked reversal omegas in retinal treated animals (Figures 3-6A, 3-7A,C-D). These results demonstrate that, in contrast to their ability to alter reversal frequency, RIM chemical synapses maintain their ability to shape reversal parameters such as length and speed during RIM activation. This ability may be modulated by behavioral state.

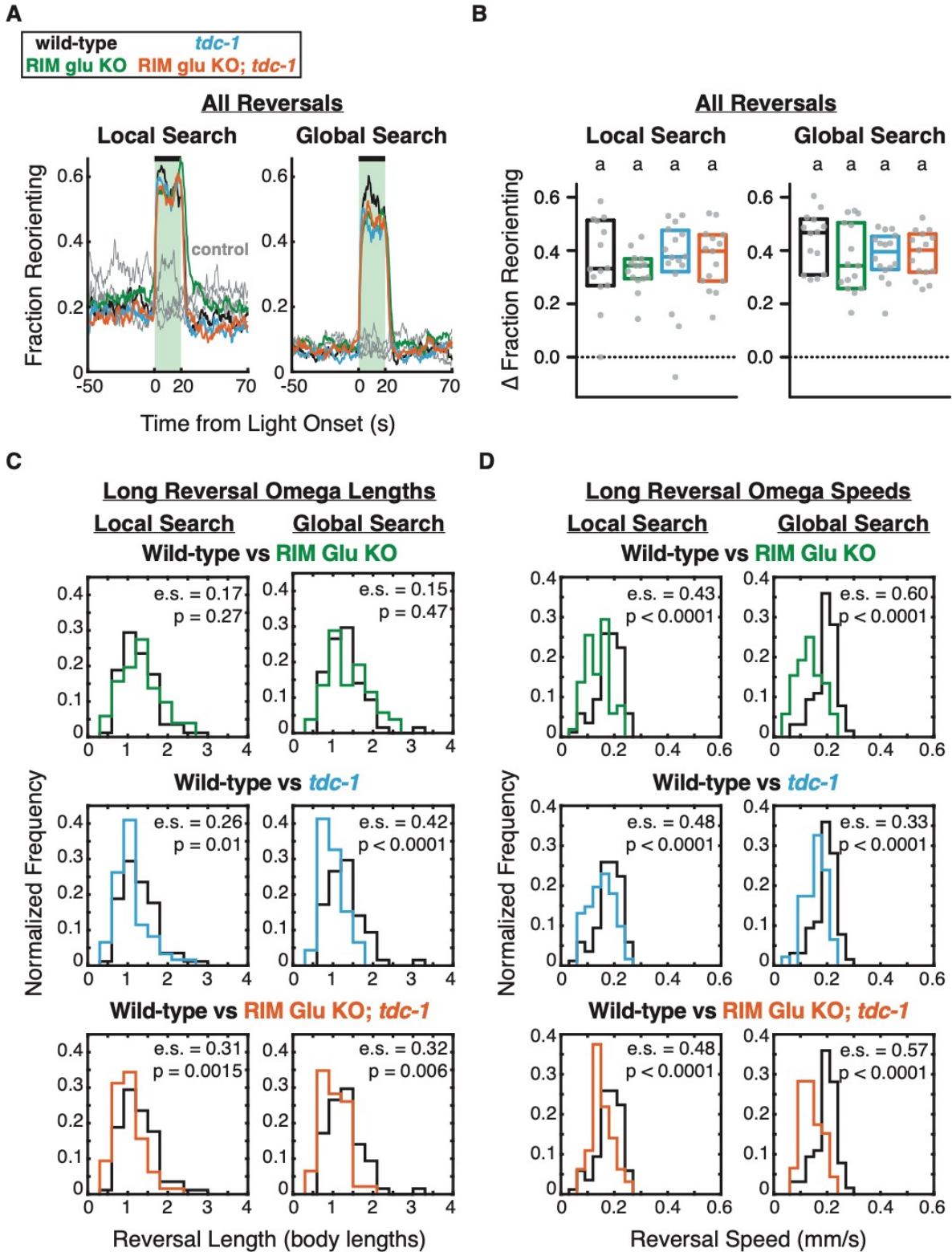


**Figure 3-6. RIM chemical synapses do not inhibit RIM-evoked reversals during off-food foraging but do increase their length and speed.**

**Figure 3-6. RIM chemical synapses do not inhibit RIM-evoked reversals during off-food foraging but do increase their length and speed.**

**(A)** Fraction of animals reversing during a 20-s, 45- $\mu\text{W}/\text{mm}^2$ , 5%-duty cycle light pulse, showing 50 s before and after pulse, with or without (gray) all-trans retinal pre-treatment. Left: aligned pulses during local search. Right: aligned pulses during global search. All full tracks included. Green shading/black bar indicate time when light was on.

**(B)** Average change in the fraction of animals reversing during the light pulse. Average taken over seconds 2-19 of the pulse. Background subtracted is averaged over 12 s before the pulse. Each gray dot is 1 assay,  $n=12-15$  animals per assay. Boxes indicate median and interquartile range. Different letters indicate statistical significance using a Kruskal-Wallis test with Dunn's multiple comparisons test.

**(C)** Distributions of reversal length of long reversal omegas evoked during a 45  $\mu\text{W}/\text{mm}^2$  light pulse.

**(D)** Distributions of reversal speed of long reversal omegas evoked during a 45  $\mu\text{W}/\text{mm}^2$  light pulse.

**(A)-(D)** Black is wild-type, green is RIM glu KO, blue is *tdc-1* mutant, orange is double RIM glu KO; *tdc-1* mutant.

**(A)** and **(B)** Data from all full tracks included, regardless of the locomotor state of the animal at the time of light onset or response time.

**(C)** and **(D)** Include data only from animals not performing long reversal omegas during the 1 s before the light pulse and within 3 s of light onset. Left: local search; right: global search.  $n = 46-85$  reversal events from 14-16 assays.  $p$  is the significance of the difference of each experimental group compared to wild-type based on the Kolmogorov-Smirnov test; e.s. is the effect size, or the D statistic.

See Methods & Appendices for further details.

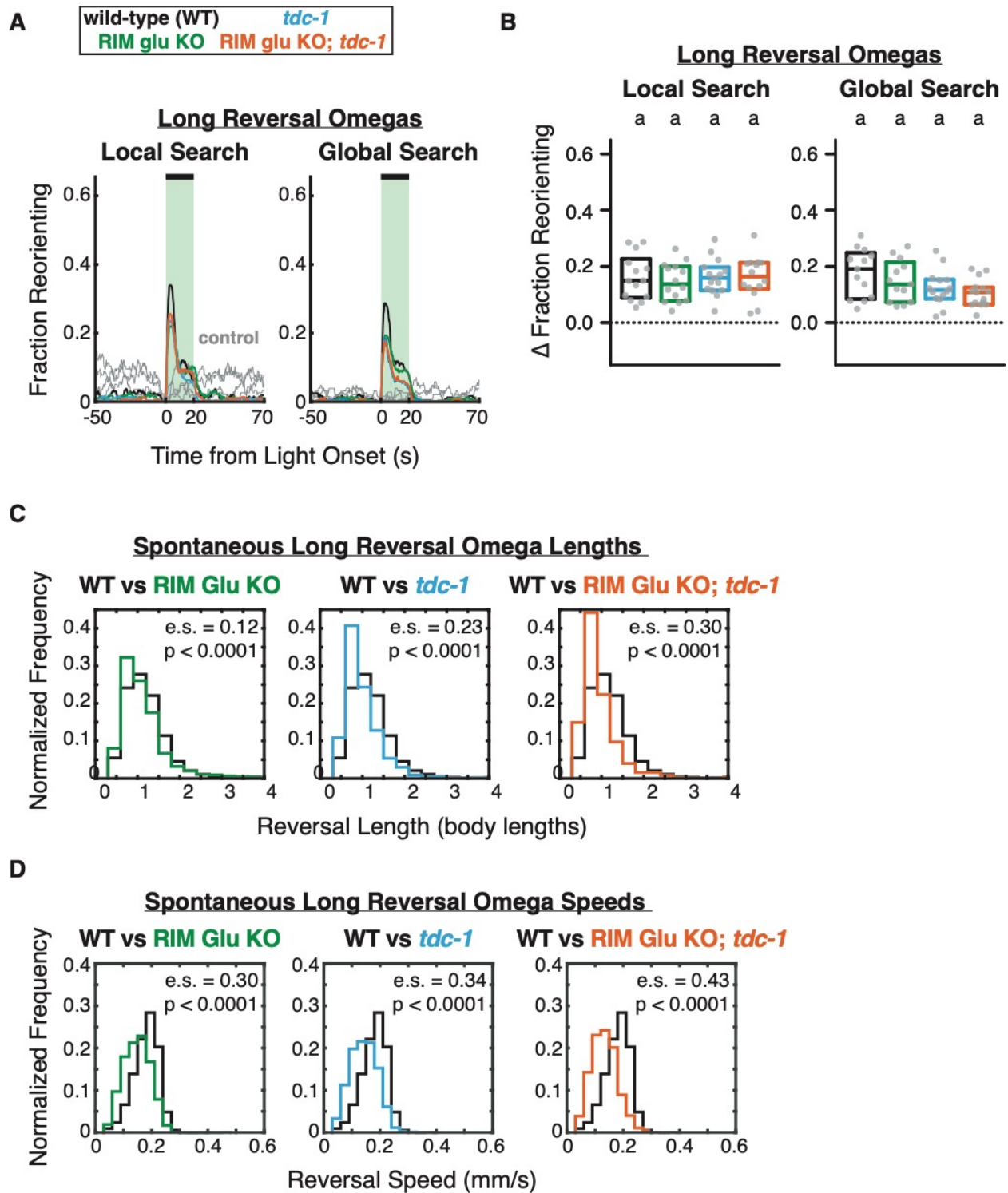


**Figure 3-7. RIM chemical synapses do not affect the fraction of RIM-evoked long reversal omegas during off-food foraging. Supplement to Figure 3-6.**

**Figure 3-7. RIM chemical synapses do not affect the fraction of RIM-evoked long reversal omegas during off-food foraging. Supplement to Figure 3-6.**

**(A)** Fraction of animals performing an evoked long reversal omega during a 20-s, 45- $\mu\text{W}/\text{mm}^2$ , 5%-duty cycle light pulse, with or without (gray) all-trans retinal pre-treatment. Left: aligned pulses during local search. Right: aligned pulses during global search. Green shading/black bar indicate time when light was on.

**(B)** Average change in the fraction of animals performing a long reversal omega during the light pulse. Left: local search; right: global search. Average taken over seconds 3-17 of the pulse. Background subtracted is averaged over 12 s before the pulse. Each gray dot is 1 assay,  $n=12-15$  animals per assay. Boxes indicate median and interquartile range. Different letters indicate statistical significance using a Kruskal-Wallis test with Dunn's multiple comparisons test.

**(C)** Distribution of reversal lengths of all spontaneous long ( $>0.5$  body length) reversals coupled to omegas from 45-minute recording normalized by probability. Data from control animals not pre-treated with all-trans retinal.

**(D)** Distribution of reversal speeds of all spontaneous long ( $>0.5$  body length) reversals coupled to omegas from 45-minute recording normalized by probability. Data from control animals not pre-treated with all-trans retinal.

**(A)-(D)** Black is wild-type, green is RIM glu KO, blue is *tdc-1* mutant, orange is double RIM glu KO; *tdc-1* mutant.

**(A)** and **(B)** Include data only from animals not performing long reversal omegas during the 1 s before the light pulse and within 3 s of light onset.

**(C)** and **(D)**  $n = 751-2167$  reversal events from 8-9 assays.  $p$  is the significance of the difference of each experimental group compared to wild-type based on the Kolmogorov-Smirnov test; e.s. is the effect size, or the D statistic.

See Methods for further details

### *RIM gap junctions inhibit spontaneous reversals and promote optogenetically-evoked reversals*

The fact that RIM activation reliably induces reversal behavior in the absence of RIM chemical synapses suggests that an additional RIM output promotes reversals. To interrogate the third class of RIM synapses, I knocked down the activity of RIM gap junctions by expressing the *unc-1(n494)* dominant negative allele in RIM under a cell-selective promoter. I first examined how RIM gap junctions affect spontaneous reversals during local and global search. RIM gap junction knockdown animals had a greatly increased rate of reversals compared to wildtype (Figure 3-8A). In contrast with chemical synapse manipulations, the RIM gap junction knockdown had little effect on the reversal length (Figure 3-8B; compare to Figures 2-2C, 2-6B). Like the RIM glu KO, the RIM gap junction knockdown had little effect on reversal speed (Figure 3-8C-D; compare to Figures 2-2D, Figure 2-7A). RIM gap junction knockdown did not affect forward speed (Figure 3-8E). These results indicate that RIM gap junctions and RIM chemical synapses have related but distinct effects on endogenous circuit activity: RIM gap junctions specifically alter reversal frequency and do so to a greater extent than RIM chemical synapses.

A second distinction between RIM gap junctions and chemical synapses was their effect in global search. RIM gap junction knockdown resulted in increased spontaneous reversals during the global search period, an effect that was not observed in RIM chemical synapse mutants (Figure 3-9).

I next asked whether RIM gap junctions affect reversal frequency upon optogenetic stimulation of RIM. Direct activation of RIM in the RIM gap junction knockdown animals resulted in a near-normal fraction of evoked reversals during local search, but significantly reduced the fraction of evoked reversals during global search (Figure 3-10A-B). The effects of RIM gap junction knockdown on reversal speed and the length of short-onset long reversal omegas were mostly not significant, save for a decrease in reversal speed during local search (Figures 3-10C-D, 3-11).

Together, these results demonstrate that RIM gap junctions strongly inhibit spontaneous reversals but can increase the number of optogenetically-driven reversals. In each case, the primary role of RIM gap junctions is regulating reorientation probability. The effect of disrupting RIM gap junctions is modulated by behavioral state.



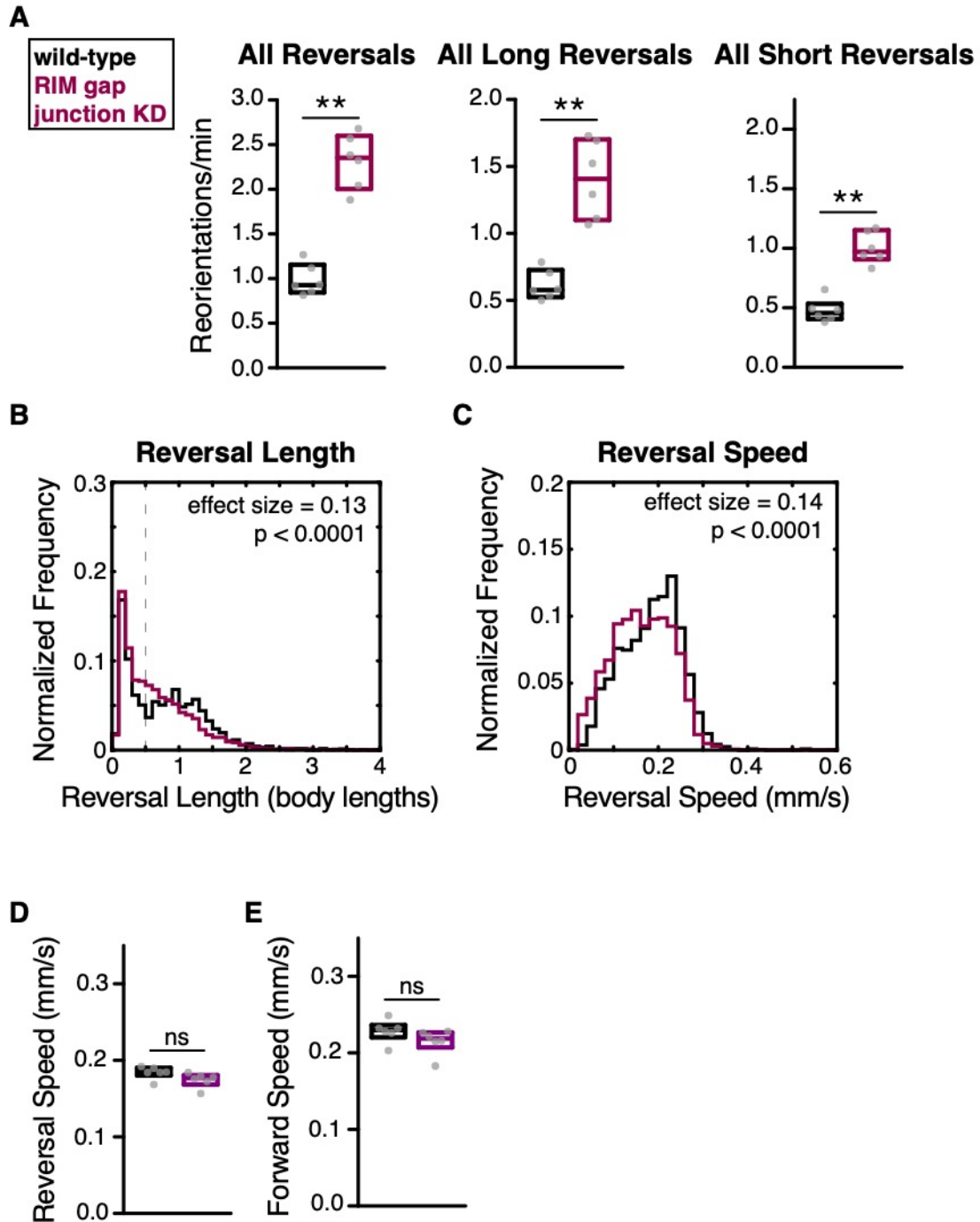


**Figure 3-8. RIM gap junctions decrease spontaneous reversal frequency during local search.**

**Figure 3-8. RIM gap junctions decrease spontaneous reversal frequency during local search.**

**(A)** Average frequency of reversals during minutes 4-8 of local search. Left panel: all reversals regardless of length. Middle panel: only long reversals ( $>0.5$  body lengths). Right panel only short reversals ( $<0.5$  body lengths). KD = knockdown.

**(B)** Distributions of reversal length of all reversals over entire 45-minute recording normalized by probability. Dotted line indicates the separation of short and long reversals in the wild-type.

**(C)** Distributions of reversal speed of all reversals over entire 45-minute recording normalized by probability.

**(D)** Average reversal speed during minutes 4-8 of local search.

**(E)** Average forward speed during minutes 4-8 of local search.

**(B)** and **(C)**  $n = 2355$  &  $5062$  reversal events from 6 assays.  $p$  is the significance of the difference of each experimental group compared to wild-type based on the Kolmogorov-Smirnov test; effect size is the  $D$  statistic.

**(A)**, **(D)**, & **(E)** Each gray dot is 1 assay,  $n = 12-15$  animals per assay. Boxes indicate median and interquartile range. Asterisks indicate significant difference between 2 conditions using Mann-Whitney test. ns = not significant.

See Methods & Appendices for further details.

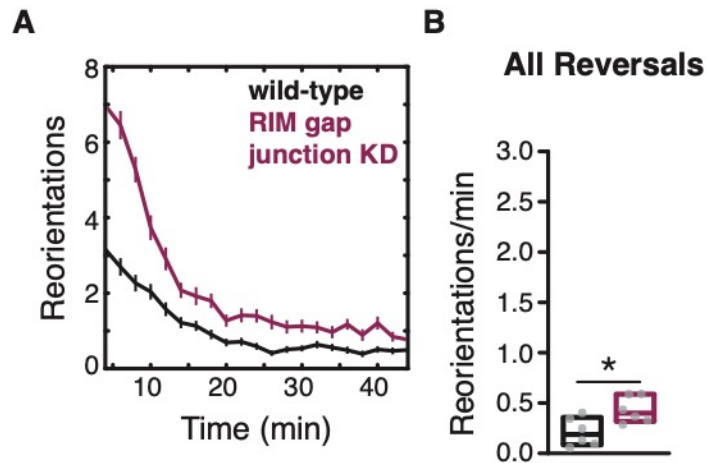


**Figure 3-9. RIM gap junctions do not affect the local search - global search transition but moderately inhibit reversal frequency during global search.**

**(A)** Average reversal frequency from minutes 4-45 of recording, binned by 2-minute intervals. Vertical dashes indicate standard error of the mean.

**(B)** Average frequency of all reversals during minutes 36-40 of global search. Each gray dot is 1 assay, n=12-15 animals per assay. Boxes indicate median and interquartile range. Asterisks indicate significant difference between 2 conditions using Mann-Whitney test. See Methods & Appendices for further details.

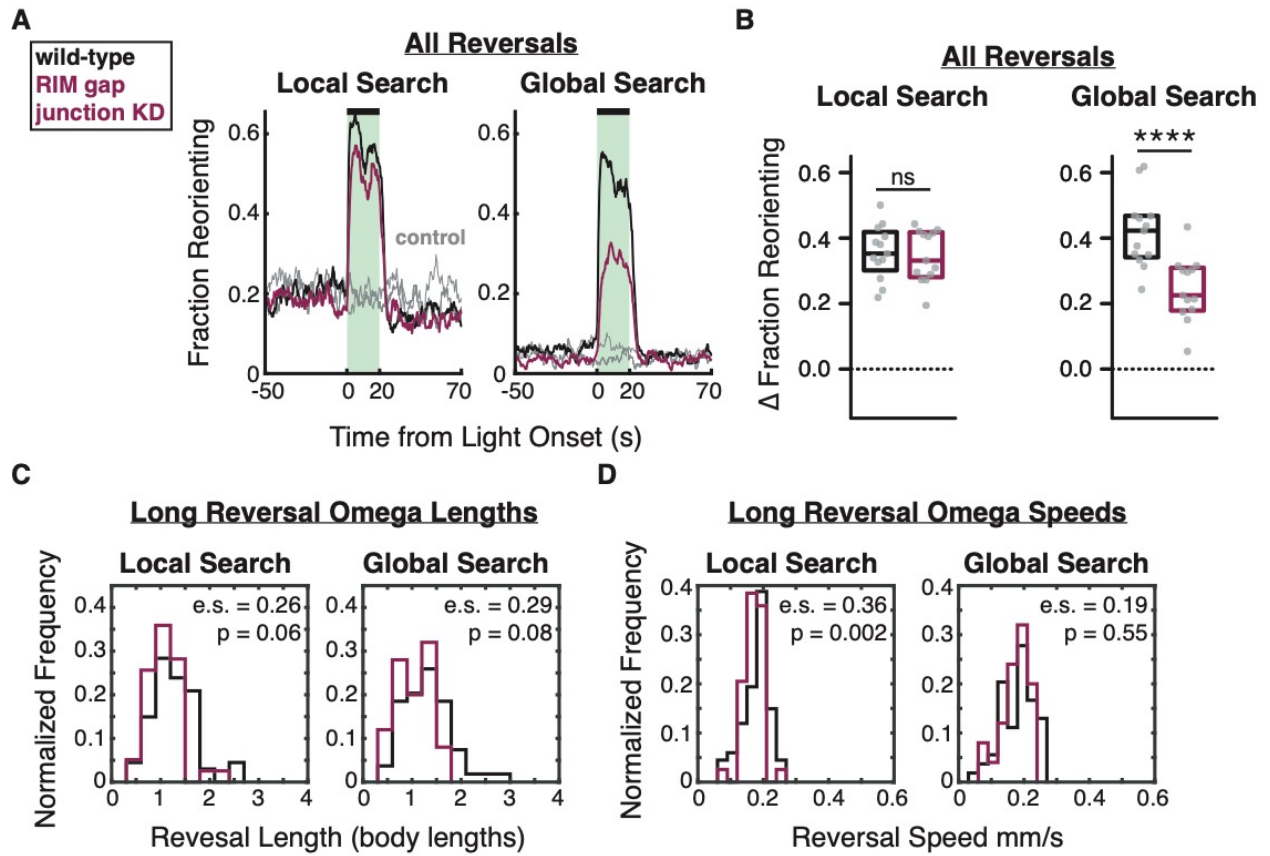


**Figure 3-10. RIM gap junctions support optogenetically-evoked reversals during global search.**

**Figure 3-10. RIM gap junctions support optogenetically-evoked reversals during global search.**

**(A)** Fraction of animals reversing during a 20-s, 45- $\mu\text{W}/\text{mm}^2$ , 5%-duty cycle light pulse, showing 50 s before and after pulse, with or without (gray) all-trans retinal pre-treatment. Left: aligned pulses during local search. Right: aligned pulses during global search. All full tracks included. Green shading/black bar indicate time when light was on.

**(B)** Average change in the fraction of animals reversing during the light pulse. Average taken over seconds 2-19 of the pulse. Background subtracted is averaged over 12 s before the pulse. Each gray dot is 1 assay,  $n=12-15$  animals per assay. Boxes indicate median and interquartile range. Asterisks indicate significant difference between 2 conditions using Mann-Whitney test. ns = not significant.

**(C)** Distributions of reversal length of long reversal omegas evoked during a 45  $\mu\text{W}/\text{mm}^2$  light pulse.

**(D)** Distributions of reversal speed of long reversal omegas evoked during a 45  $\mu\text{W}/\text{mm}^2$  light pulse.

**(A)-(D)** Black is wild-type; magenta is RIM gap junction knockdown.

**(A)** and **(B)** Data from all full tracks included, regardless of the locomotor state of the animal at the time of light onset or response time.

**(C)** and **(D)** Include data only from animals not performing long reversal omegas during the 1 s before the light pulse and within 3 s of light onset. Left: local search; right: global search.  $n = 25-67$  reversal events from 13 assays.  $p$  is the significance of the difference of each experimental group compared to wild-type based on the Kolmogorov-Smirnov test; e.s. is the effect size, or the D statistic.

See Methods & Appendices for further details.

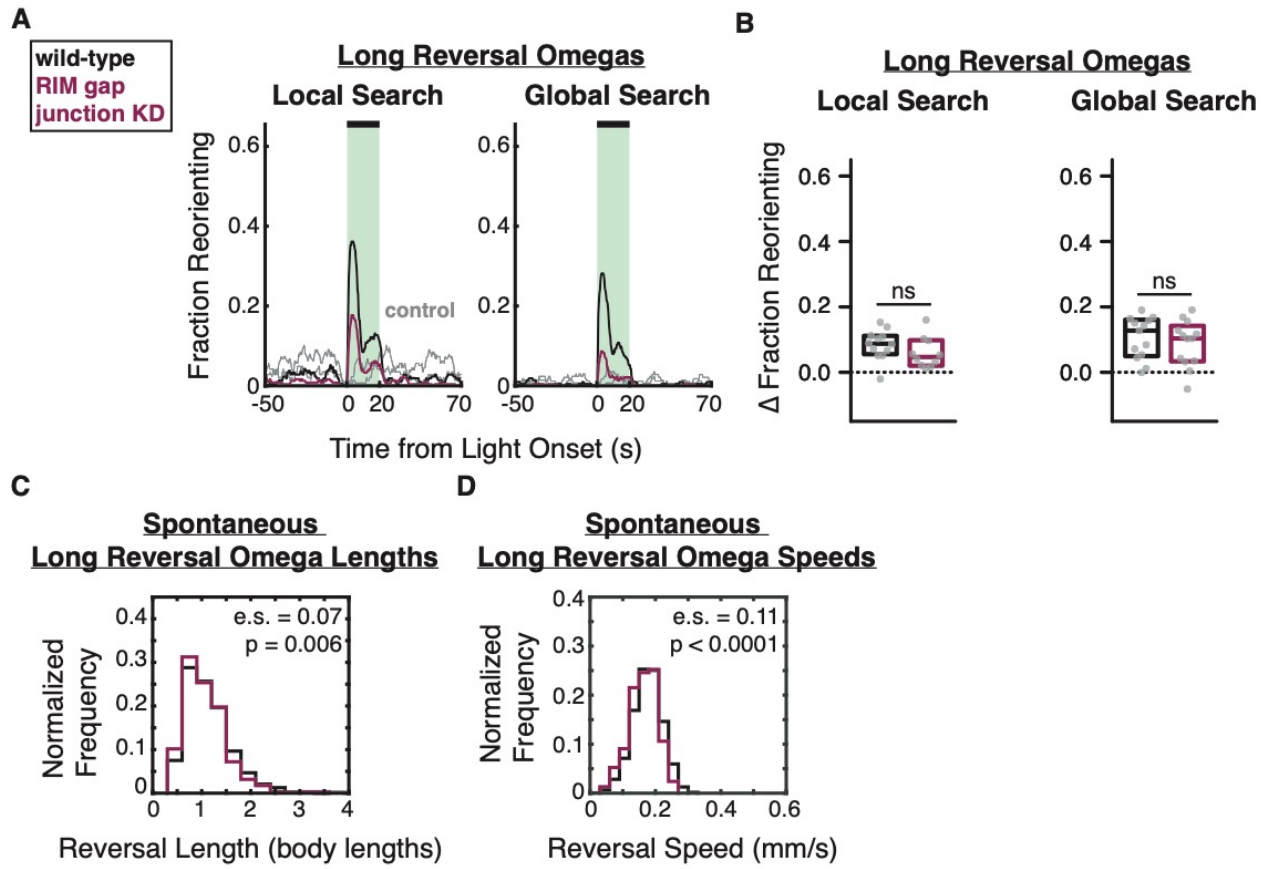


**Figure 3-11. RIM gap junctions do not affect optogenetically-evoked long reversal omegas. Supplement to Figure 3-10.**

**Figure 3-11. RIM gap junctions do not affect optogenetically-evoked long reversal omegas. Supplement to Figure 3-10.**

**(A)** Fraction of animals performing an evoked long reversal omega during a 20-s, 45- $\mu\text{W}/\text{mm}^2$ , 5%-duty cycle light pulse, with or without (gray) all-trans retinal pre-treatment. Left: aligned pulses during local search. Right: aligned pulses during global search. Green shading/black bar indicate time when light was on.

**(B)** Average change in the fraction of animals performing a long reversal omega during the light pulse. Left: local search; right: global search. Average taken over seconds 3-17 of the pulse. Background subtracted is averaged over 12 s before the pulse. Each gray dot is 1 assay,  $n=12-15$  animals per assay. Boxes indicate median and interquartile range. Different letters indicate statistical significance using a Kruskal-Wallis test with Dunn's multiple comparisons test.

**(C)** Distribution of reversal lengths of all spontaneous long ( $>0.5$  body length) reversals coupled to omegas from 45-minutes recording normalized by probability. Data from control animals not pre-treated with all-trans retinal.

**(D)** Distribution of reversal speeds of all spontaneous long ( $>0.5$  body length) reversals coupled to omegas from 45-minutes recording normalized by probability. Data from control animals not pre-treated with all-trans retinal.

**(A)-(D)** Black is wild-type; magenta is RIM gap junction knockdown

**(A)** and **(B)** Include data only from animals not performing long reversal omegas during the 1 s before the light pulse and within 3 s of light onset.

**(C)** and **(D)**  $n = 915$  &  $1729$  reversal events from 9 assays.  $p$  is the significance of the difference of each experimental group compared to wild-type based on the Kolmogorov-Smirnov test; e.s. is the effect size, or the D statistic.

See Methods for further details

## Discussion

### *Intrinsic stereotypy of RIM driven reversal omegas*

In this chapter I used optogenetics to investigate how RIM's depolarization influences the reversal circuit and, ultimately, shapes reversal behavior across behavioral states. Providing a strong, direct stimulus to RIM is sufficient to generate long reversals coupled to omega turns during both local and global search. These experiments also suggest an intrinsic limit to the natural duration of reversal states. For all light pulses exceeding 5 s, reversals were followed by omega turns that peaked 7-8 s after light onset, indicating that the duration of RIM driven reversal bouts is stereotyped. (Figure 3-2, Table 3-1). While previous work showed that exposure to increasingly noxious thermal stimuli increases reversal duration, but not turn duration, I found that omega turning bouts that occurred during a light pulse were about twice as long as those that occurred at light offset (Ghosh et al., 2012). These results show that omega turns are not all equivalent—their duration varies based on the stimuli that induce them (temperature versus RIM activation), and presumably on the composition of the neural circuit that generates them.

### *RIM chemical synapses are essential regulators of reversal parameters*

Results from Chapter 2 indicate that inactivating RIM chemical synapses increases reversal frequency during spontaneous behavior. However, chemical synapses do not appreciably affect reversal frequency upon depolarizing RIM directly, even at intermediate levels of stimulation (Figure 3-6A-B). In contrast, the effect of chemical synapses on reversal length and speed persists—RIM tyramine increases reversal length and speed, and RIM glutamate increases reversal speed. Thus, RIM chemical synapses, especially RIM tyraminerpic synapses, regulate these features of reversals under all tested circumstances.

### *RIM gap junctions are bidirectional regulators of reversal frequency*

RIM forms extensive gap junctions with the reversal command neurons AVA and AVE (Cook et al., 2019, White et al., 1986). My results demonstrate two opposite effects of RIM gap junctions: depolarizing RIM directly leads to an increase in reversals that depends on these gap junctions, but spontaneous reversals during foraging are strongly inhibited by the same gap junctions (Figure 3-8A-B, Figure 3-9A-B). I speculate that during spontaneous behavior, RIM is generally hyperpolarized, and stabilizes the forward state through electrical synapses that hyperpolarize AVA and AVE. When RIM is depolarized, the same electrical synapses initiate and stabilize the reversal state through the same electrical coupling to AVA and AVE. Imaging of RIM activity using a genetically encoded calcium indicator in freely moving wild-type and RIM gap junction knockdown animals may further elucidate the function of RIM gap junctions in spontaneous reversal behavior.



The ability of RIM gap junctions to bidirectionally regulate reversal behavior reconciles previous results indicating that RIM can either promote or inhibit reversal frequency (Figure 3-12). All RIM synapses inhibit reversal frequency, while gap junctions also promote this behavioral parameter. While gap junctions mainly function to regulate reversal frequency, RIM chemical synapses affect multiple parameters of reversal behavior.

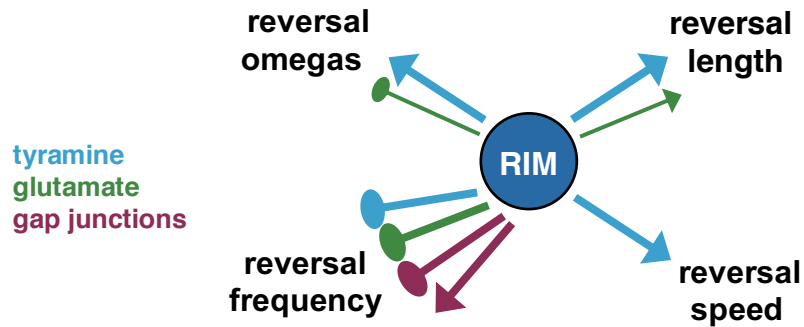


**Figure 3-12. Effects of RIM chemical synapses and gap junctions on reversal behavior.**

A schematic summarizing the results of this chapter and Chapter 2: Triangle arrow heads indicate that a behavioral parameter is promoted. Circle arrow heads indicate that a behavior is inhibited.

*RIM coupling to the reversal circuit is modulated by behavioral state*

Previous experiments in wild-type animals indicated that RIM coupling to the reversal circuit is constant across local search and global search behavioral states (López-Cruz et al., 2019). My optogenetic stimulation of RIM in RIM gap junction knockdown animals revealed that UNC-9 (the innexin affected by UNC-1) is required for RIM-evoked reversals during global search, but not local search (Figure 3-9A-B). This result indicates that the transition from local search to global search is associated with changes downstream of RIM activity. Further experiments are needed to determine the nature of this modulation.

## Future Directions

*How do global brain dynamics influence the structure of behavior?*

My work may provide insight into how reversals, which are correlated with RIM activity, are resolved into omega turns, which are highly dependent upon AIB activity. Direct stimulation of RIM results in a reversal that typically terminates after ~7 s, followed by an omega turn; light offset at 5 s also results in an omega turn. While these evoked behaviors may not be endogenously generated, they suggest that the inertia of overall global brain dynamics may constrain the output of the reversal circuit.

The neurons that drive reversals, like RIM and AVA, make up the 1<sup>st</sup> principal component of the global brain state, which explained ~40% of the variance of the data in immobilized animals (Kato et al., 2015). The neurons that drive turning, like AIB, contribute to the 2<sup>nd</sup> principal component, which explained ~20% of the variance. Yet both AIB and RIM are active during the reversal state (Gordus et al., 2015, Kato et al., 2015). My results in the previous chapter suggest that RIM glutamate prolongs the reversal state and inhibits the initiation of the omega state. I speculate that this is mediated by RIM action on glutamate-gated chloride channels expressed by AIB.

Experiments in this chapter revealed that during direct, prolonged RIM optogenetic activation most animals do not reverse continuously throughout the light pulse. Rather, animals ceased reversing and began turning at stereotyped time points. Moreover, a spike in turning was observed at light offset, providing suggestive evidence that competition between RIM-dominated and AIB-dominated circuits are associated with the shift from a reversal to a turn in spontaneous behavior.

Notably, reducing AVA activity has little effect on network state dynamics in immobilized animals (Kato et al., 2015). In freely moving animals, chemogenetic inhibition of AVA activity results in a pause, instead of a reversal, in response to touch and osmotic stimuli, and the pause is followed by an omega turn after ~7 seconds (Pokala et al., 2014). These data align with my results, as omega turning bouts peaked ~7 seconds after light onset (Figure 3-2, Table 3-1). Taken together, these results suggest that an internal “reversal state” of stereotyped duration persists in freely moving animals despite perturbations to the reversal behavior itself. I speculate that this feature of the natural network state dynamics allows optogenetically-evoked reversal-omega behaviors, albeit diminished in length and speed, to persist in the absence of RIM chemical synapses.

My results suggest that artificially depolarizing RIM does little to combat natural internal dynamics of reversal-omega behaviors. It is possible that stimulating RIM and AVA together, or stimulating RIM while inhibiting AIB, would push more animals into very long reversal states. My experiments also show that prolonged RIM stimulation can suppress the reversal state for several seconds following light offset (Figure 3-1). This behavior may represent a further manifestation of global network dynamics, and the natural transition from reversal to omega to forward state that precedes another

reversal. How would this work? Prolonged stimulation of RIM could lead to a persistent forward state through synaptic plasticity, or through neuropeptide release from RIM or other neurons, in a fashion analogous to the work on pCD neurons and aggression in *Drosophila* (Jung et al., 2020). Further experiments are needed to evaluate how RIM activity interacts with endogenous neural states and behavioral dynamics.

#### *How is RIM decoupled from the reversal circuit during global search?*

The results of this chapter reveal that RIM gap junctions inhibit spontaneous reversals during global search, albeit with a much-reduced effect compared to local search, suggesting that RIM activity or synapse fidelity decreases during global search. This may reflect an overall decrease in the activity of the reversal circuit.

Optogenetic stimulation of RIM in RIM gap junction knockdown animals revealed that RIM gap junctions have a preferential effect on RIM-evoked reversals during global search, indicating that there is redundancy between RIM gap junctions and chemical synapses (or between RIM gap junctions formed by UNC-9 and another class of RIM gap junctions) that is diminished in global search. However, whether the decoupling of RIM from the reversal motor output is presynaptic, postsynaptic, or both, is yet to be determined. Crossing RIM glu KO animals and *tdc-1* mutants to RIM gap junction knockdown animals may reveal whether the decrease in RIM-evoked reversals during global search is due to modulation of RIM chemical synapses. Additionally, observing the activity of RIM and its postsynaptic partners in freely moving worms across behavioral states may provide further insights into the nature of RIM decoupling. Moreover, simultaneous imaging of RIM neural activity and exo- and endocytosis dynamics in immobilized worms could also reveal whether presynaptic changes occur. I begin to address this question in the next chapter.

#### *Do RIM chemical synapses and RIM gap junctions interact?*

Chemical synapses and gap junctions are known to interact with one another, particularly if they are in close proximity (Garcia-Rill et al., 2007, Liu et al., 2017, Pereda et al., 2013, Smith & Pereda, 2003). Inhibitory chemical synapses can act as a shunt, antagonizing the effects of gap junctions, such as in the inferior olive of the mammalian nervous system (Pereda et al., 2013, Smith & Pereda, 2003). In contrast, chemical synapses have also been found to increase electrical coupling through gap junctions, such as in the Mauthner cells of the mammalian auditory system (Pereda et al., 2013, Smith & Pereda, 2003). Similarly, gap junctions can both promote and antagonize effects of chemical synapses. Antidromic electrical synapses can amplify the chemical transmission of presynaptic neurons, while electrical coupling between two neurons via gap junctions can lower their input resistance, diminishing the effects of chemical inputs (Garcia-Rill et al., 2007, Liu et al., 2017).

RIM gap junctions may interact with both RIM presynapses and postsynapses, based on their locations along the RIM process and their proximity to one another. In

immobilized worms, RIM soma calcium dynamics are slower than those of the process (Gordus et al., 2015). RIM gap junctions with AVE are located posteriorly on the RIM process, close to the soma (Cook et al., 2019, White et al., 1986, Figure 3-13). Thus, it is possible that RIM-AVE gap junctions generally impede the flow of information between the more anterior RIM synapses and the RIM soma (Garcia-Rill et al., 2007).

RIM-AVE gap junctions are also adjacent to RIM presynaptic chemical outputs to the forward command neuron AVB, which expresses both inhibitory and excitatory glutamate receptors (Brockie et al., 2001, Cook et al., 2019, Hart et al., 1995, Maricq et al., 1995, Taylor et al., 2019, White et al., 1986, Figure 3-13). The strong effects of RIM gap junctions on reversal frequency suggest there is electrical coupling between RIM, AVE, and AVA. While the results of Chapter 2 suggest that RIM glutamate may activate inhibitory receptors on AVB, it is also possible that during the reversal state, when electrical coupling between RIM and AVE is high, RIM-AVE gap junctions disrupt the glutamatergic outputs from RIM to AVB, decoupling the forward and reversal circuits.

Additionally, RIM-AVE gap junctions are located in close proximity to chemical synaptic inputs from AIB (Cook et al., 2019, White et al., 1986, Figure 3-13). AIB is glutamatergic, and RIM expresses both excitatory glutamate receptors, such as GLR-1, GLR-2, NMR-1, and NMR-2, and inhibitory glutamate receptors, such as AVR-14 (Brockie et al., 2001, Chalasani et al., 2007, Dillon et al., 2015, Kang and Avery 2009, Katz et al., 2019, Maricq et al., 1995, Piggott et al., 2011, Taylor et al., 2019, Zou et al., 2018). Taken together, the results of this chapter and those of Chapter 2 provide evidence that antagonism between RIM and AIB may drive the transition from the reversal state to the turning state. Interactions between RIM gap junctions and nearby AIB postsynaptic chemical inputs may contribute to this antagonism. It is possible that glutamate release from AIB onto AVR-14 counteracts electrical coupling between RIM, AVE, and AVA through a shunting mechanism. Additionally, strong electrical coupling between RIM and AVE, and AVA, may lower the input resistance of RIM, diminishing the effects of chemical inputs from AIB.

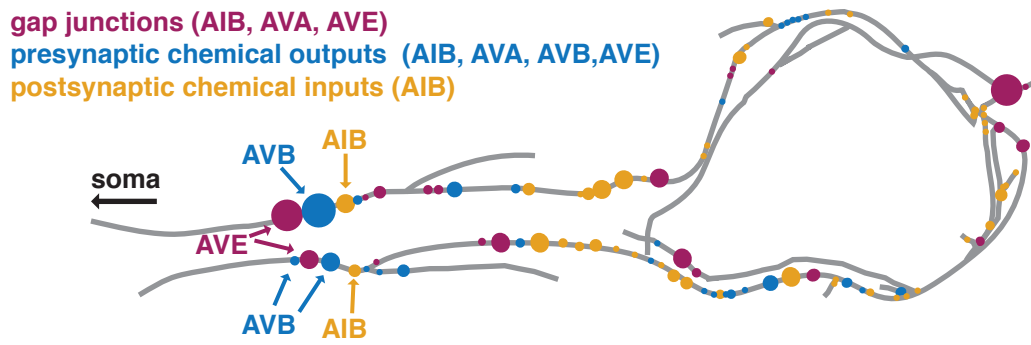


**Figure 3-13. Locations of relevant RIM chemical synapses and RIM gap junctions.**

Gray lines indicate the location of the RIM process. Circles indicate position and relative size of chemical synapses and gap junctions. Synapses discussed in the text are indicated with labels and arrows. Redrawn from wormwiring.org (Cook et al., 2019).

## **PART II**

### **CHAPTER 4: Comparative analysis of RIM glutamate and RIM tyramine exocytosis and endocytosis dynamics in intact *C. elegans***

#### **Introduction**

In the previous chapters I have demonstrated that RIM glutamate and tyramine have differential effects on reversal behavior. My results suggest that both glutamate and tyramine are released from RIM during off-food foraging, but their differential effects could manifest from presynaptic differences, postsynaptic differences, or some combination of the two. It is not known whether RIM tyramine and glutamate are packaged into the same vesicles or different vesicles. The packaging of RIM glutamate and tyramine has implications for the ability of RIM to effect reversal behavior across behavioral and network states. If RIM glutamate and tyramine are released from different vesicles, they may have different requirements for release, allowing one to be preferentially released under particular conditions (Vaaga et al., 2014). I hypothesized that differential release of RIM glutamate and RIM tyramine could be one mechanism by which RIM promotes behavioral variability.

Previous work from mouse neuronal cell culture has established that the vesicular glutamate transporter VGLUT (EAT-4) and the vesicular biogenic amine transporter VMAT (CAT-1) can localize to overlapping vesicles in a single neural population (Silm et al., 2019). Thus, I set out to characterize the exo- and endocytosis dynamics of RIM glutamate and RIM tyramine using vesicular transporter-pHluorin fusions. I recorded exo- and endocytosis dynamics in intact *C. elegans* to determine whether RIM tyramine and glutamate are released under the same conditions and share exo- and endocytosis dynamics.

Donovan Ventimiglia previously fused super-ecliptic pHluorin, a GFP derivative whose fluorescence is highly sensitive to pH, into the first luminal loop of the *C. elegans* vesicular glutamate transporter EAT-4 (here termed VGLUT-pH) and used this fusion to compare the release and retrieval of glutamate from two sensory neurons (Miesenböck et al., 1998, Ventimiglia & Bargmann, 2017). pHluorin is quenched at the acidic pH of a synaptic vesicle but becomes fluorescent when vesicles fuse with the plasma membrane during exocytosis (Figure 4-1). To compare glutamate and tyramine exo- and endocytosis dynamics in RIM I expressed VGLUT-pH in RIM neurons and also made and validated a reporter in which I fused pHluorin to the vesicular biogenic amine transporter (here termed VMAT-pH). I then analyzed and compared the inferred exo- and endocytosis dynamics of each pHluorin transporter fusion to begin to elucidate whether RIM glutamate and RIM tyramine share release and retrieval properties. While RIM::VGLUT-pH and RIM::VMAT-pH share exo- and endocytosis dynamics, suggesting that they are co-transmitted at the same time, my preliminary results also suggest that

VMAT may additionally localize to distinct vesicles that have slower exocytosis dynamics than other VMAT and VGLUT containing vesicles.

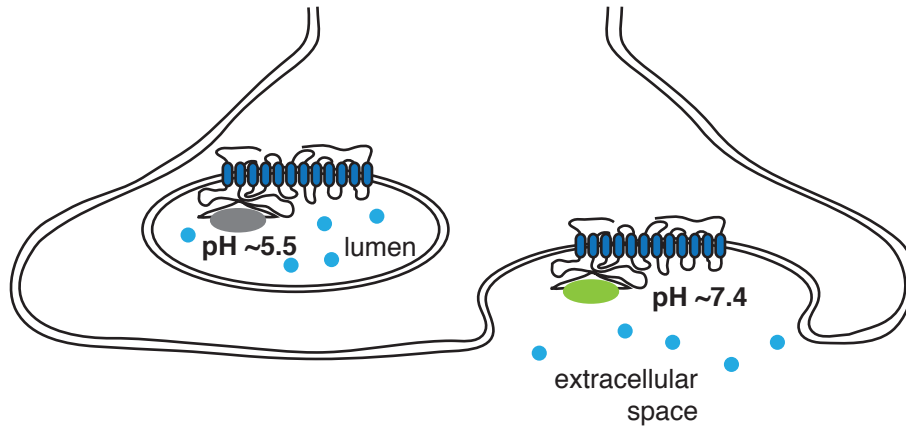


**Figure 4-1. Vesicular transporter-pHluorin fusions fluoresce upon exposure to the extracellular space.**

Schematic of pHluorin (gray and green ovals) fused to the first luminal loop of a vesicular transporter (dark blue). Left: Before neurotransmitter (light blue circles) release and after neurotransmitter retrieval, pHluorin (gray oval) is quenched in the acidic environment of the vesicle lumen. Right: As vesicles fuse to the cell membrane, releasing neurotransmitter into the extracellular space, pHluorin (green oval) fluoresces upon exposure to neutral pH. pHluorin fusion redrawn from Onoa et al., 2010.



## Results

Following Donovan's work, I generated VMAT-pH by replicating the positioning of a VMAT2 pHluorin fusion that has been used in rat primary neuronal culture (Onoa et al., 2010, see also Experimental Procedures). I used homology alignment of rat VMAT2 and its *C. elegans* homolog CAT-1 to insert super-ecliptic pHluorin into the first luminal loop of the transporter, surrounding pHluorin with the same serine-glycine-threonine 5' and 3' linkers used by Onoa et al. (Figure 4-1).

Upon generation of the VMAT-pH reporter, which indicates RIM tyramine exo- and endocytosis events in RIM, I generated separate RIM::VGLUT-pH and RIM::VMAT-pH strains, in which fluorescence localized to the RIM process and showed measurable fluctuations in immobilized *C. elegans* (Figure 4-2A). These animals did not show behavioral deficits in RIM-dependent reversal behaviors, indicating that transgenic expression of transporter-pHluorin fusions do not grossly disrupt neurotransmitter packaging or release from RIM (Figure 4-3).

In order to record and analyze glutamate and tyramine exo- and endocytosis dynamics from RIM, RIM::VGLUT-pH and RIM::VMAT-pH animals were immobilized in a microfluidic device flooded with 1 mM levamisole in buffer to minimize movement. I recorded spontaneous pHluorin dynamics in wild-type animals for 10 minutes at 5 frames/second and 100x magnification (Figure 4-2A-C). I was able to detect spontaneous changes in fluorescence, with many traces exhibiting  $\Delta F/F_0$  (%) values of 20 to 40. These changes were larger in magnitude than those previously observed in *C. elegans* sensory neurons (~5%  $\Delta F/F_0$ , Ventimiglia and Bargmann 2017).

To interpret these fluorescence changes, I compared them to spontaneous RIM calcium transients measured with GCaMP sensors, which have been previously characterized in similar conditions. In animals trapped within a microfluidic device, RIM is sharply bimodal, with spontaneous, long-lasting high and low calcium states (Gordus et al., 2015, Kato et al., 2015). High-calcium RIM states are synchronized with high-calcium states in several other neurons, including the AVA backward command neurons, and comparisons of activity in restrained and freely-moving animals suggest that the high-activity RIM/AVA state correlates with reversal behavior. Together, these results suggest that animals in a microfluidic device cycle spontaneously between ~minute-long states that represent fictive forward motion (low RIM calcium) and fictive reversals (high RIM calcium). I replicated these results by measuring RIM calcium within the same region of the axon that I used to visualize pHluorin dynamics (Figure 4-4).

I found that VGLUT-pH and VMAT-pH dynamics are bimodal, with long-lasting high and low activity states, like RIM calcium dynamics. Both VGLUT-pH and VMAT-pH fluorescence had spontaneous increases in fluorescence from a stable baseline to a high-fluorescence state that could last several minutes before returning to baseline for seconds or minutes (Figures 4-2B-C, Figure 4-4). Direct observation suggested that VGLUT-pH and VMAT-pH typically exhibited an initial sharp rise in fluorescence

followed by a subsequent slower rise or plateau (Figure 4-2C). I infer that these sharp rises in fluorescence, and possibly the slower rises, represent exocytosis events associated with increased RIM calcium. Decay from these high activity states also decreased over the timescale of seconds. When not interrupted by a subsequent increase in fluorescence, decreases in fluorescence gradually fell back to baseline (Figure 4-2C). I hypothesize that these decreases represent endocytosis and vesicle re-acidification (Silm et al., 2019, Ventimiglia & Bargmann, 2017).

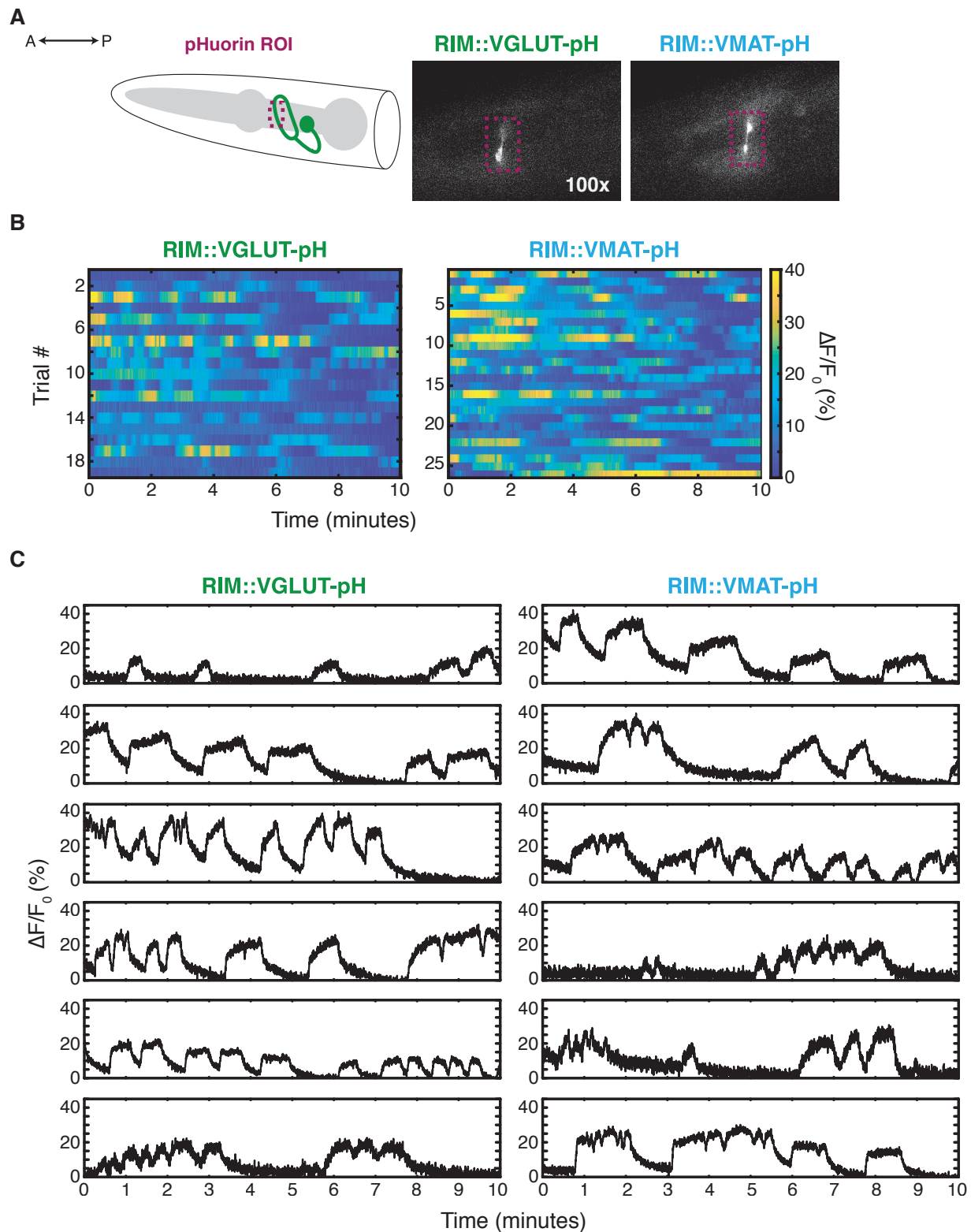


**Figure 4-2.** RIM::VGLUT-pH and RIM::VMAT-pH exhibit spontaneous fluorescence changes, inferred to be exo- and endocytosis events, in immobilized animals.

**Figure 4-2. RIM::VGLUT-pH and RIM::VMAT-pH exhibit spontaneous fluorescence changes, inferred to be exo- and endocytosis events, in immobilized animals.**

**(A)** Left: Cartooned schematic of RIM soma and projections into the nerve ring. Middle: an example of RIM::VGLUT-pH region of interest. Right: an example of RIM::VMAT-pH region of interest. Maroon box indicates the region of interest (ROI) in all three panels. Recordings were taken from the same area at the edge of the nerve ring when possible to maintain consistency.

**(B)** Heat maps showing traces used in further analyses. Left: RIM::VGLUT-pH traces. Right: RIM::VMAT-pH traces. Warmer colors indicate higher Delta F/F. Each trace is from a unique animal. Delta F/F is calculated using median of lowest 10% of ROI fluorescence values and is the percent change in fluorescence.

**(C)** Example traces from (B). Left: RIM::VGLUT-pH traces. Right: RIM::VMAT-pH traces. See Methods & Appendices for further details.

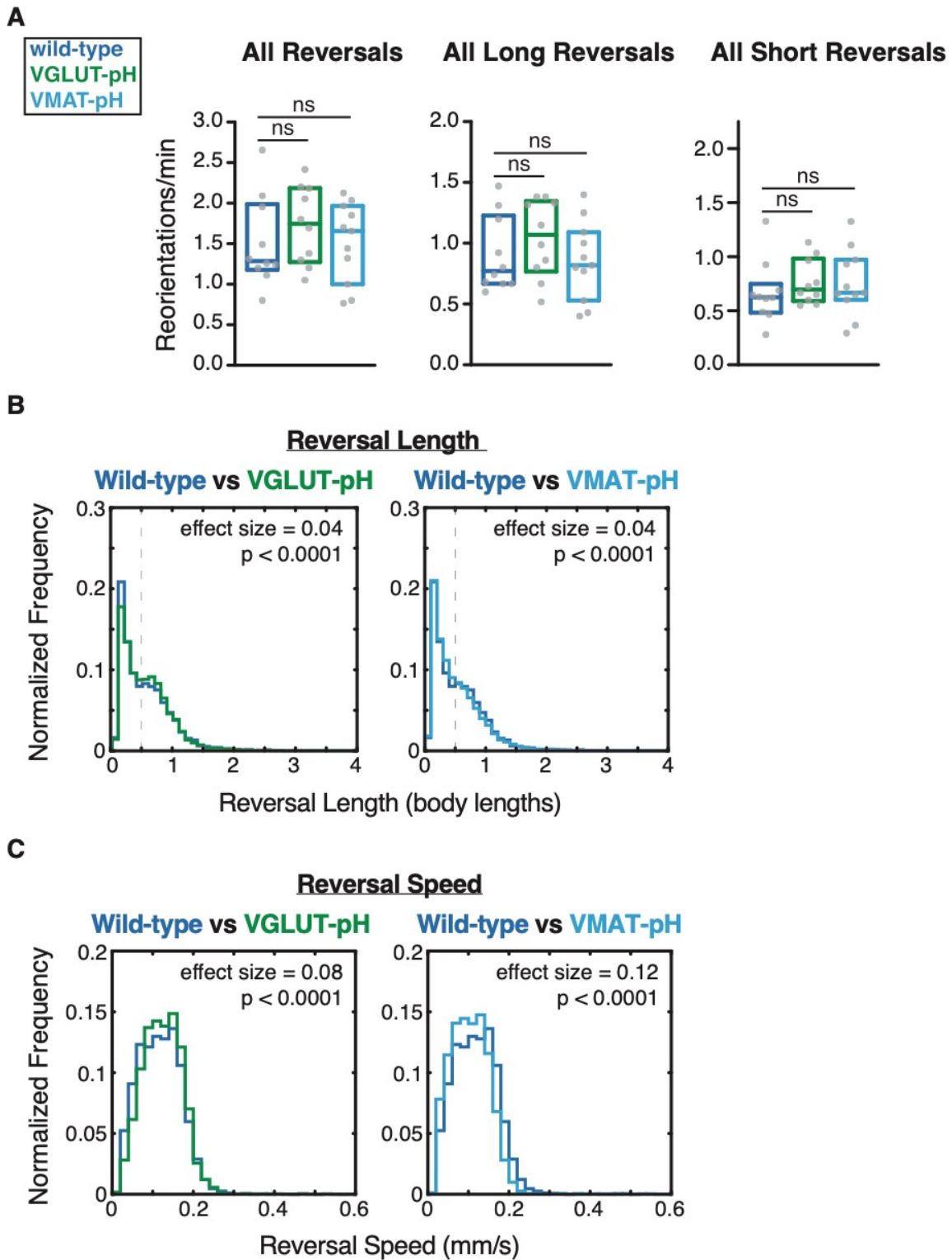


**Figure 4-3. Reversal behavior is unaltered in RIM::VGLUT-pH and RIM::VMAT-pH animals. Supplement to Figure 4-2.**

**Figure 4-3. Reversal behavior is unaltered in RIM::VGLUT-pH and RIM::VMAT-pH animals. Supplement to Figure 4-2.**

**(A)** Average frequency of reversals during minutes 4-8 of local search. Left panel: all reversals regardless of length. Middle panel: only long reversals (>0.5 body lengths). Right panel only short reversals (<0.5 body lengths). Each gray dot is 1 assay, n=12-15 animals per assay. Boxes indicate median and interquartile range. Different letters indicate statistical significance using a Kruskal-Wallis test with Dunn's multiple comparisons test.

**(B)** Distributions of reversal length of all reversals over entire 45-minute recording normalized by probability. Dotted line indicates the separation of short and long reversals in the wild-type.

**(C)** Distributions of reversal speed of all reversals over entire 45-minute recording normalized by probability.

**(B)** and **(C)** n=5382-6308 reversal events from 10-11 assays. p is the significance of the difference of each experimental group compared to wildtype based on the Kolmogorov-Smirnov test, effect size is the D statistic.

See Methods & Appendices for further details.

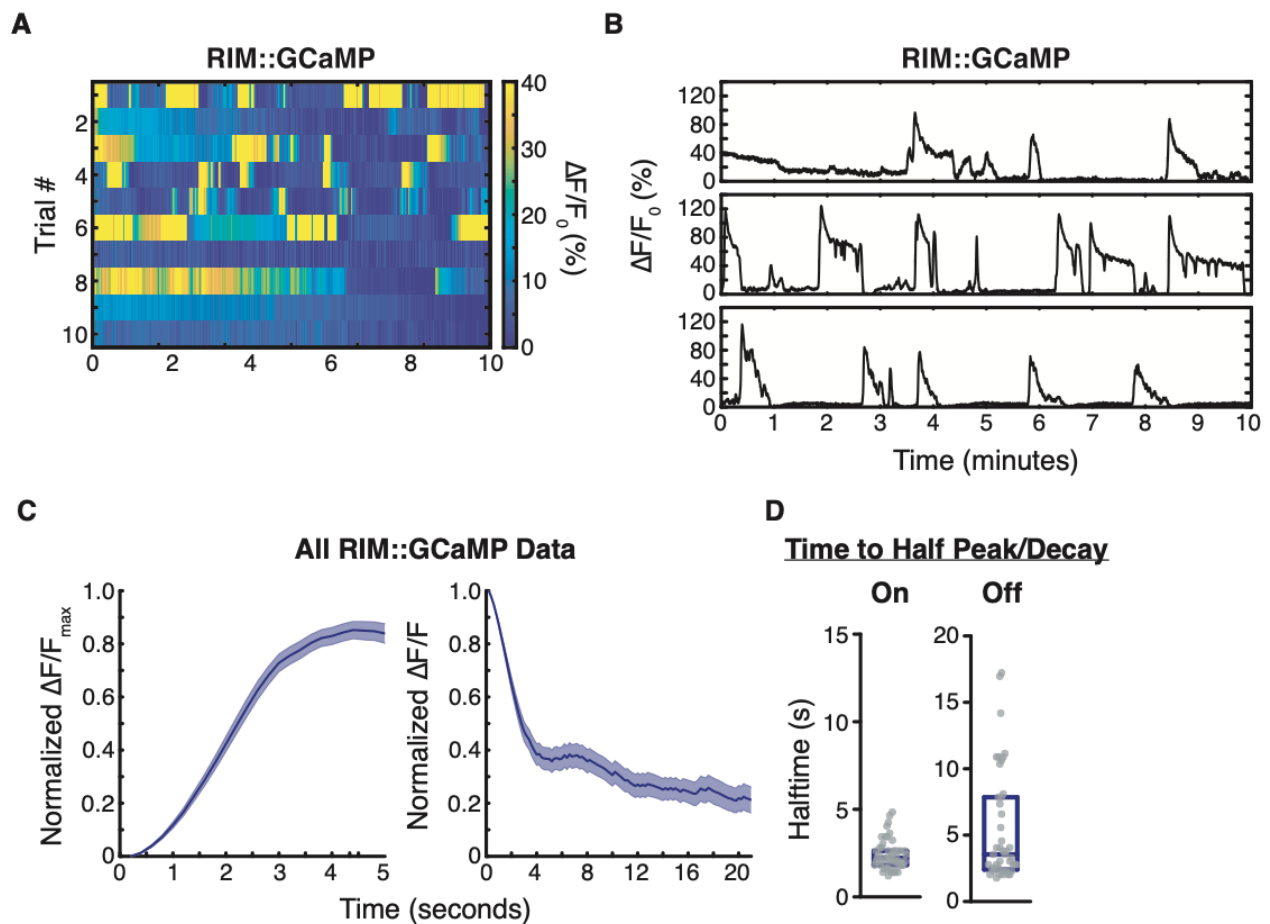


**Figure 4-4. RIM pFluorin dynamics reflect RIM axonal calcium dynamics. Supplement to Figure 4-2, Figure 4-7, & Figure 4-10.**

**(A)** Heat maps showing RIM GCaMP dynamics from the same ROI as pFluorin traces. Warmer colors indicate higher  $\Delta F/F$ . Each trace is from a unique animal.  $\Delta F/F$  is calculated using median of lowest 10% of ROI fluorescence values and is the percent change in fluorescence.

**(B)** Example traces from (A).

**(C)** Left: The mean of the data from all “on” curves aligned to their normalized minima. Right: The mean of the data from all “off” curves aligned to their normalized maxima. Shading indicates the standard error of the mean. X-axes encompass time points up until the mean time at which curves reach their maxima (left) or minima (right).

**(D)** The time point at which a curve reached half the maximum (left) or minimum (right) value of the curve. Left: halftimes of “on” curves. Right: halftimes of “off” curves. Each gray dot is a single event from 8-10 assays. Outliers were excluded from this analysis (see Methods).

See Methods & Appendices for further details.

### *Initial examination of VGLUT-pH and VMAT-pH exocytosis events in RIM*

As RIM is an interneuron that does not respond reliably to sensory stimuli, I extracted inferred exo- and endocytosis events from traces of spontaneous dynamics rather than aligning events to stimulus onset or offset (Gordus et al., 2015). I calculated the time derivative of the smoothed data and used fluorescence changes to find potential exo- and endocytosis events throughout each trace (Figures 4-5, 4-8, see Methods). Traces of spontaneous dynamics contain events that are heterogenous in both changes in fluorescence and timescale. In order to objectively separate events, I normalized the changes in fluorescence by their maxima and chose time-derivative parameters that extracted all event types. I then fit the extracted events to single and double exponential curves (Figures 4-6, 4-9, see Methods) and compared the two fits using the Akaike's Information Criterion (Figures 4-7, 4-10). I did not explore other models.

Both VGLUT-pH and VMAT-pH exocytosis events fell into two classes of curves that best fit either single or double exponentials (Figures 4-6, 4-7A). To further evaluate RIM exocytosis dynamics and to compare VGLUT-pH and VMAT-pH dynamics, I sorted the events based on whether they best fit a single or double exponential and plotted the mean of each data set (Figure 4-7B). For both VGLUT-pH and VMAT-pH, events that best fit a single exponential rose faster than those that best fit a double exponential, showing that this method separates events of different timescales.

I went on to compare VGLUT-pH and VMAT-pH dynamics. Considering events that best fit a single exponential, there was no difference between VGLUT-pH and VMAT-pH dynamics (Figure 4-7B). In contrast, for events that best fit a double exponential VMAT-pH exocytosis curves rose more slowly than those of VGLUT-pH. To quantify differences between these dynamics, I found the time to reach the half peak for each class of potential exocytosis event. The times to half-peak of VMAT-pH and VGLUT-pH were indistinguishable for events that best fit single exponentials, averaging around 3 seconds (Figure 4-7C). The time to half peak for events that fit a double exponential was higher for VMAT-pH events compared to VGLUT-pH events (Figure 4-7C). This difference was apparently associated with the second, slower component of the potential exocytosis event; the first, faster component was similar for both sensors and closely resembled the events observed in traces with a single class of event (Figure 4-7B). However, I have not yet analyzed the timescales of the fast and slow components of the double exponential class quantitatively, which would be necessary to make this conclusion.

One interpretation of these results is that VGLUT-pH and VMAT-pH share a form of fast exocytosis in RIM, with a half-rise time of about 3 seconds. In addition, both VGLUT-pH and VMAT-pH have a slower form of exocytosis from RIM axons, and this second class of events is slower in VMAT-pH than in VGLUT-pH.



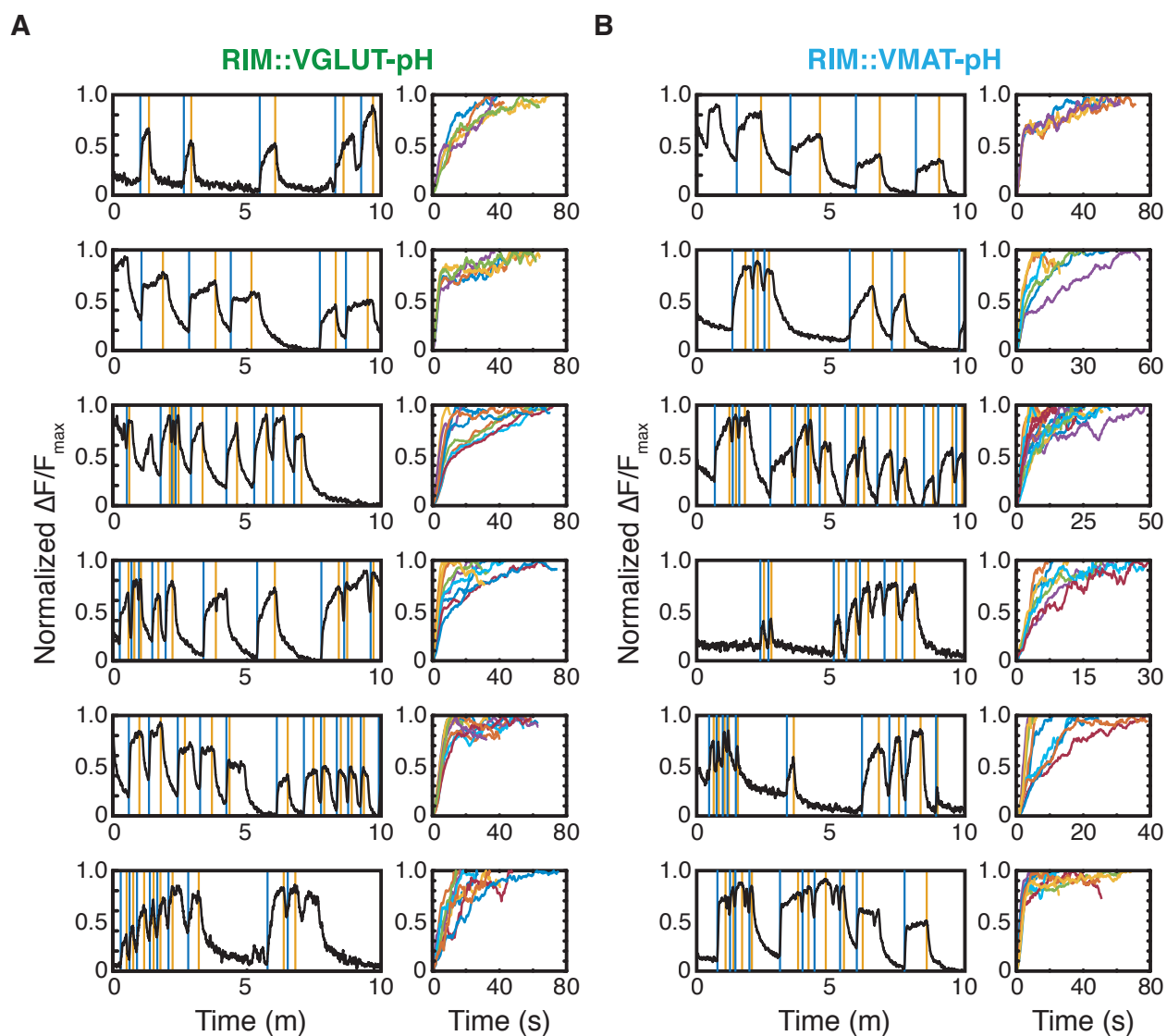


**Figure 4-5. Representative inferred exocytosis events extracted from spontaneous pHluorin dynamics. Supplement to Figure 4-2 and Figure 4-7.**

(A) Example processed traces from VGLUT-pH corresponding to those shown in 4-2C.  
 (B) Example processed traces from VMAT-pH corresponding to those shown in 4-2C.  
 (A) and (B). Left panels: example processed traces. Blue vertical lines indicate the beginning of an inferred exocytosis event. Orange vertical lines indicate the termination of an event. Right panels: All inferred exocytosis events pulled from each trace, individually normalized by dividing by their maxima. Note that x-axes vary. See Methods & Appendices for further details.

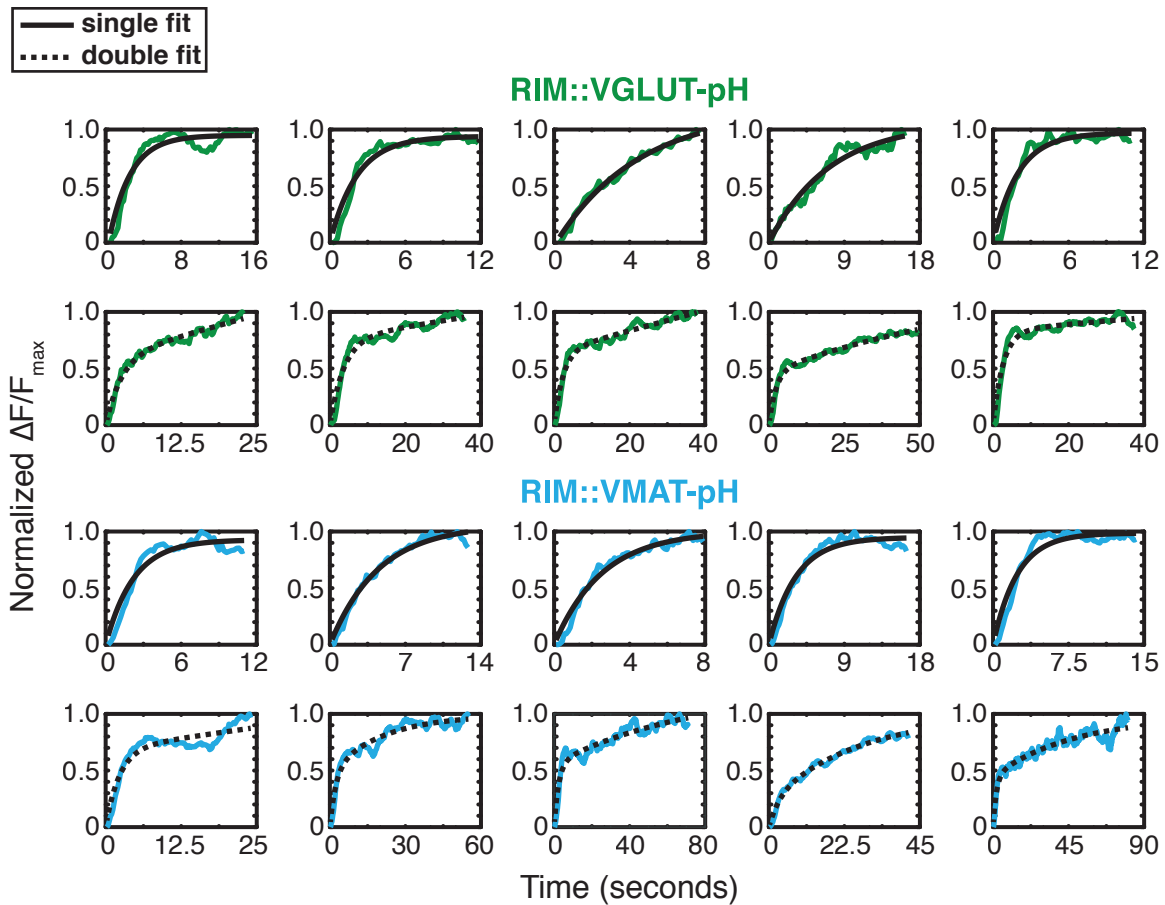


**Figure 4-6. Representative inferred exocytosis events fitted to single and double exponentials. Supplement to Figure 4-7.**

Examples of inferred exocytosis events that best fit to single (solid) and double (dashed) exponentials. For each sensor, the top line (five traces) shows events best fit by a single exponential, and the second line (five traces) shows events best fit by a double exponential. Example single fits shown have an AICp value of  $<0.1$  and double fits shown have an AICp value of  $>0.9$ .

See Methods & Appendices for further details.

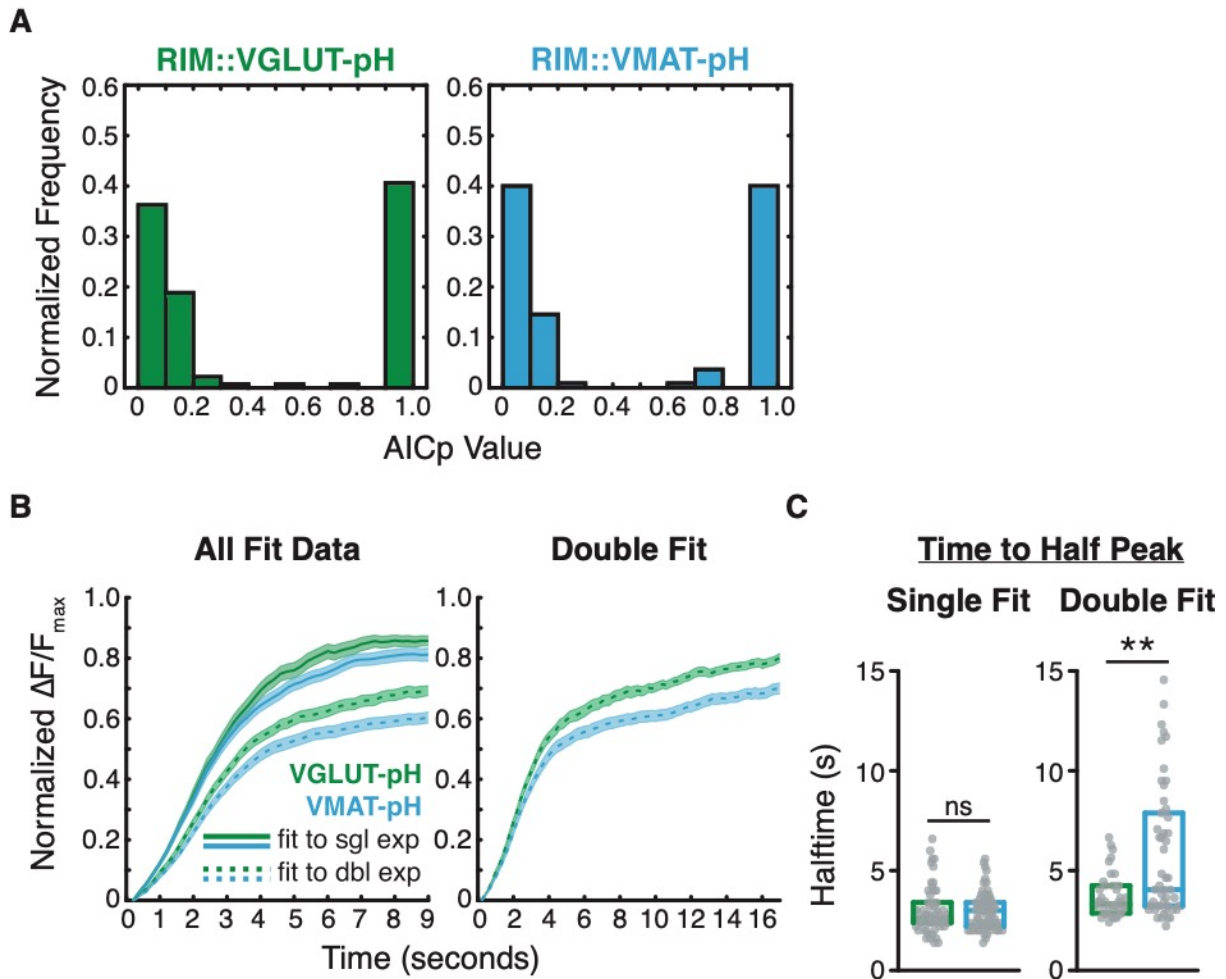


**Figure 4-7. VGLUT-pH and VMAT-pH may share fast exocytosis dynamics but may differ in a class of slower exocytosis events.**

**(A)** Histogram of AICp values for inferred exocytosis curves from RIM::VGLUT-pH (left) and RIM::VMAT-pH (right) normalized by probability. AICp values  $< 0.5$  indicate that the data better fit a single exponential while AICp values  $> 0.5$  indicate that the data better fit a double exponential (see Methods).  $n = 110$  and  $139$  from  $19$  and  $26$  assays.

**(B)** The mean of the data from all curves that best fit either a single exponential (solid lines) or double exponential (dashed lines), aligned to their normalized minima. Shading indicates the standard error of the mean. X-axes encompass time points up until the mean time at which curves reach their maxima for data best fit to single exponentials (left) and double exponentials (right). Left: both classes of data plotted together. Right: Only data that best fit the double exponential, shown over a longer timescale.

**(C)** The time point at which a curve reached half the maximum value of the curve. Left: halftimes of curves that best fit a single exponential. Right: halftimes of curves that best fit a double exponential, including both classes of events. Note slower timescales of some VMAT-pH events. Each gray dot is a single event from  $19$  (VGLUT-pH) or  $26$  (VMAT-pH) assays. Outliers were excluded from this analysis (see Methods).

### *Initial examination of VGLUT-pH and VMAT-pH endocytosis dynamics in RIM*

I also extracted inferred endocytosis events from the spontaneous pHluorin traces, using a similar logic that that used above. The decrease in fluorescence associated with pHluorin sensors is a two-step process, including internalization of the molecule from the plasma membrane and subsequent reacidification of the synaptic vesicles, but I will refer to it as “endocytosis” for simplicity.

As with potential exocytosis events, I first classified potential endocytosis events using objective criteria with smoothed data and the time derivative (Figure 4-8). I then fit events to single and double exponentials and classified them based on Akaike’s Information Criterion (Figures 4-9). As with exocytosis events, there were two classes of endocytosis events that best fit to single or double exponentials (Figure 4-10A). Curves that best fit single exponentials fell faster than those that fit double exponentials (Figure 4-10B).

When comparing VGLUT-pH and VMAT-pH events there was no difference between endocytosis dynamics for either fast or slow events, as reflected by the similarity of the halftimes of the events of both reporters (Figure 4-10B-C).

Taken together, these initial data suggest that both RIM glutamate and RIM tyramine release and retrieval have time courses consistent with RIM axonal calcium dynamics, and therefore that the pHluorin reporters are monitoring calcium-dependent events in the RIM axon. Based on these preliminary analyses, vesicles in RIM containing VGLUT and VMAT appear to share exo- and endocytosis dynamics. However, there may be a separate class of VMAT-specific vesicles that exhibit slower exocytosis dynamics.

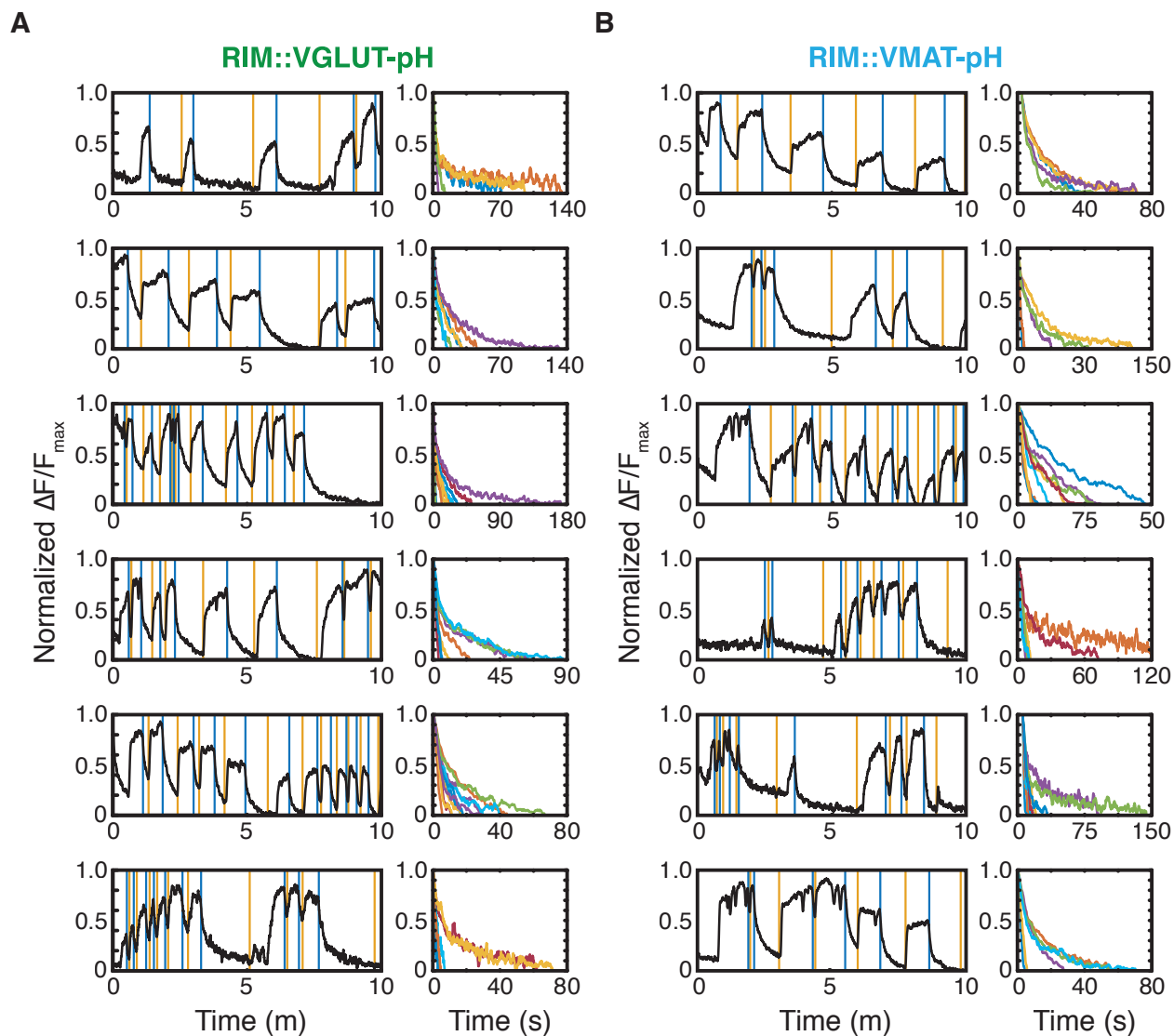


**Figure 4-8. Representative inferred endocytosis events extracted from spontaneous pHluorin dynamics. Supplement to Figure 4-2 and 4-10.**

(A) Example processed traces from VGLUT-pH corresponding to those shown in 4-2C.  
 (B) Example processed traces from VMAT-pH corresponding to those shown in 4-2C.  
 (A) and (B). Left panels: example processed traces, smoothed by 10-frame (2-s) binning and normalized by dividing by the maximum. Blue vertical lines indicate the beginning of an endocytosis event. Orange vertical lines indicate the termination of an endocytosis event. Right panels: All inferred endocytosis events pulled from each trace, individually normalized by dividing by their maxima. Note that x-axes vary.

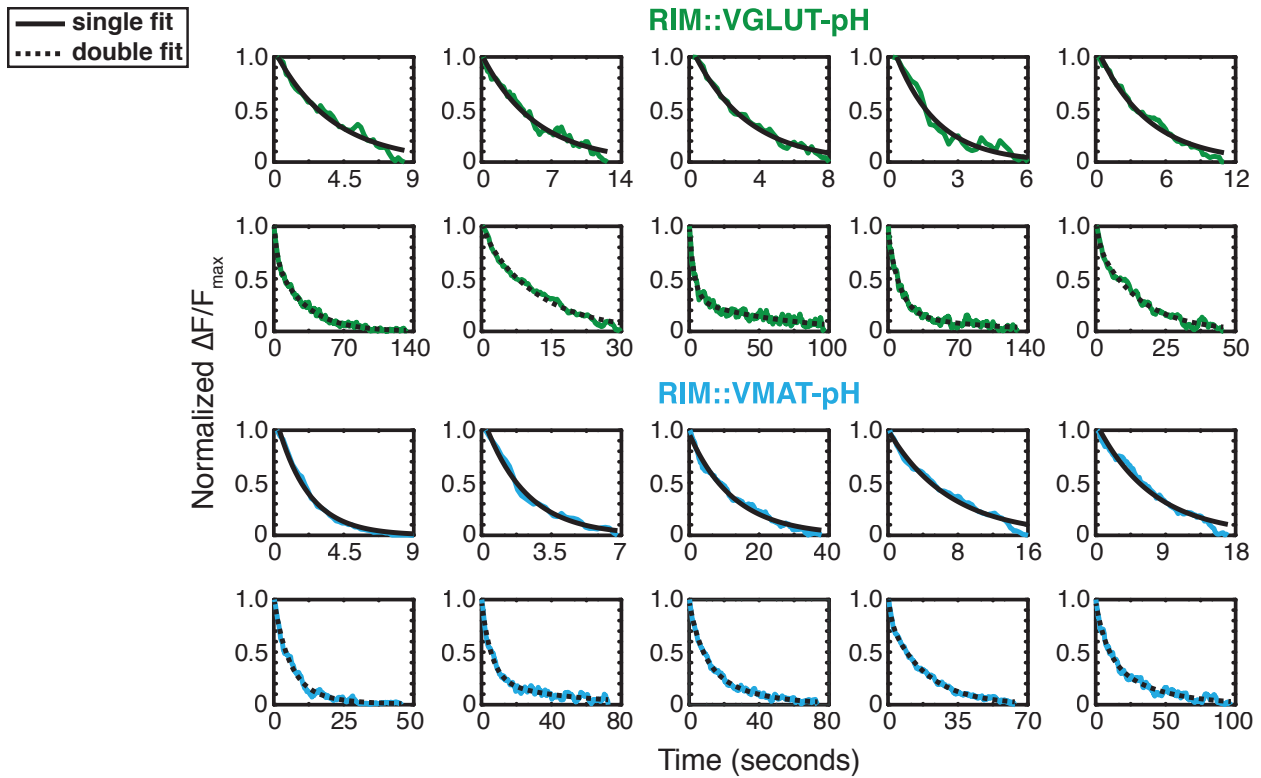


**Figure 4-9. Representative inferred endocytosis events fitted to single and double exponentials. Supplement to Figure 4-7.**

Examples of inferred endocytosis events that best fit to single (solid) and double (dashed) exponentials. For each sensor, the top line (five traces) shows events best fit by a single exponential, and the second line (five traces) shows events best fit by a double exponential. Example single fits shown have an AICp value of  $<0.1$  and double fits shown have an AICp value of  $>0.9$ .

See Methods & Appendices for further details.

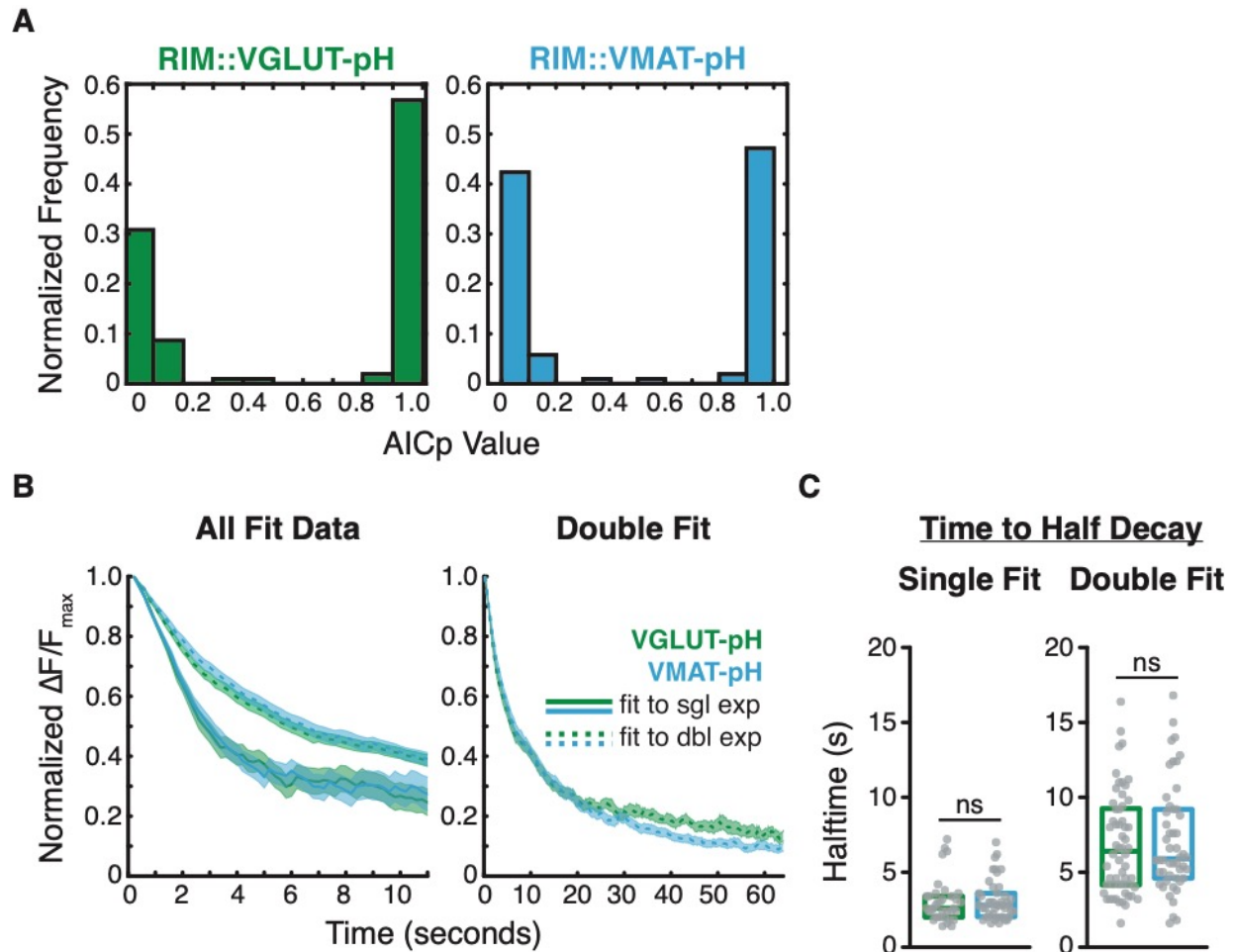


**Figure 4-10. VGLUT-pH and VMAT-pH may share endocytosis dynamics.**

**(A)** Histogram of AICp values for endocytosis curves from RIM::VGLUT-pH (left) and RIM::VMAT-pH (right) normalized by probability. AICp values  $< 0.5$  indicate that the data better fit a single exponential while AICp values  $> 0.5$  indicate that the data better fit a double exponential (see Methods).  $n = 104$  from 17 and 26 assays.

**(B)** The mean of the data from all curves that best fit either a single exponential (solid lines) or double exponential (dashed lines), aligned to their normalized minima. Shading indicates the standard error of the mean. X-axes encompass time points up until the mean time at which curves reach their minima for data best fit to single exponentials (left) and double exponentials (right). Left: both classes of data plotted together. Right: Only data that best fit the double exponential, shown over a longer timescale.

**(C)** The time point at which a curve reached half the maximum value of the curve. Left: halftimes of curves that best fit a single exponential. Right: halftimes of curves that best fit a double exponential, including both classes of events. Each gray dot is a single event from 17 (VGLUT-pH) or 26 (VMAT-pH) assays. Outliers were excluded from this analysis (see Methods).

## Discussion

### *RIM exo- and endocytosis dynamics follow RIM calcium dynamics*

Previous imaging of VGLUT-pH dynamics in ASH and AWC<sup>ON</sup> sensory neurons showed that glutamate exo- and endocytosis dynamics in these neurons that resembled changes in calcium dynamics in response to sensory stimuli, albeit with a slower time course than calcium signals (Ventimiglia & Bargmann, 2017). My results indicate that similarly, RIM VGLUT-pH and RIM VMAT-pH dynamics are consistent with the activity patterns of RIM inferred from calcium dynamics and may represent vesicle exocytosis and endocytosis. First, the pHluorin signals are strongly bimodal, with distinct high- and low-fluorescence states. These may correspond to the high- and low- calcium states that are thought to represent correlates of reversal and forward locomotion states, respectively (Gordus et al., 2105; Kato et al., 2015). Second, the durations of these states and their interspersion resembles those previously observed in spontaneous calcium signals, and those that I observed in RIM axons. At higher resolution, RIM pHluorin signals rise and fall more slowly than RIM axonal calcium; this is consistent with the slower timescales of exocytosis, endocytosis, and vesicle reacidification compared to calcium flux, and also consistent with pHluorin studies in other neurons (Onoa et al., 2010, Silm et al., 2019, Ventimiglia & Bargmann, 2017). Therefore, I hypothesize that RIM VGLUT-pH and RIM VMAT-pH signals can be used to infer glutamate and tyramine release from the RIM axon.

In this work, I have validated the use of VMAT-pH in *C. elegans* and showed that VMAT-pH dynamics occur on similar timescales as VGLUT-pH dynamics. By extracting and analyzing on and off events for all three sensors, I provide evidence that RIM glutamate release and RIM tyramine release are consistent with RIM axonal calcium dynamics. Analysis of VGLUT-pH and VMAT-pH dynamics in calcium channel mutants, among others, may confirm and extend the understanding of the relationship between VGLUT, VMAT, and calcium flux in RIM.

### *The nature of RIM co-transmission during off-food foraging*

My results from Chapter 2 show that RIM glutamate and RIM tyramine both regulate reversal behavior during local search, suggesting that both neurotransmitters are released from RIM during this behavior. In this chapter I have shown that RIM glutamate and RIM tyramine share exo- and endocytosis dynamics, suggesting that they may be co-released and providing further evidence that they are released at the same time. In addition to affecting reversal behavior through its release from RIM, RIM glutamate may affect reversal behavior through presynaptic mechanisms associated with co-release, such as vesicular synergy (Aguilar et al., 2017, El Mestikawy et al., 2011, Hnasko and Edwards, 2012, Vaaga et al., 2014). Imaging VMAT-pH dynamics in RIM glu KO animals (and imaging VGLUT-pH dynamics in *tdc-1* mutants) may indicate whether presynaptic mechanisms affect neurotransmitter release from RIM.



## Future Directions

### *Is RIM tyramine released from a distinct, slow class of vesicles?*

My results suggest that RIM glutamate and RIM tyramine are released at the same time and may be released from overlapping vesicles, with tyramine being released from a distinct class of vesicles that have slower exocytosis dynamics compared to RIM glutamate exocytosis. Indeed, biogenic amines are known to be released from dense-core-like vesicles that have slower dynamics than those of classical small clear vesicles (Bruns and Jahn, 1995, Fei and Krantz, 2009 Krantz et al., 2000, Thureson-Klein, 1983, Waites et al., 2001). Analysis of mutants required for classical vesicle release and dense core vesicle release, such as UNC-13 (MUNC-13) and UNC-31 (CAPS), respectively, may confirm this finding (Dittman, 2019, Speese et al., 2017). Additionally, limiting analysis to particular time points during exocytosis and endocytosis and exploring other models for curve fitting may reveal other classes of vesicles that are yet to be seen through my preliminary analyses.

### *Linking pHluorin dynamics to behavior*

While my data suggest RIM glutamate and RIM tyramine are released under the same conditions in immobilized worms, it is yet to be determined whether these spontaneous pHluorin dynamics relate to RIM activity during off-food foraging behavior. While pHluorin imaging is not possible in freely moving worms, simultaneous co-imaging of pHluorin and genetically encoded calcium indicators in immobilized worms in conjunction with calcium imaging in freely moving worms may help to bridge this gap. Additionally, if synaptic protein mutants affect RIM pHluorin dynamics in immobilized worms, testing these mutants for behavioral deficits could indicate that they are behaviorally relevant.

### *The biological relevance of pHluorin variability across neurons*

In previous work imaging VGLUT-pH in *C. elegans*, the fluorescence changes in ASH and AWC<sup>ON</sup> neurons were much smaller than those observed in this study, even though VGLUT-pH was imaged under conditions that cause robust calcium changes (Ventimiglia & Bargmann, 2017). It is possible that differences in pHluorin fluorescence across neurons is associated with differences in the size of the endogenous readily-releasable vesicle pools of these neurons. Analysis of pHluorin dynamics in more neuron types and in mutants that regulate vesicle pool dynamics may reveal whether pHluorin fluorescence is a relevant measure of vesicle pool size in intact *C. elegans* (Alabi and Tsien, 2012).

## CHAPTER 5: Perspectives

### Summary

In this thesis I have used genetic manipulations, behavioral analyses, and both manipulations and observations of neural activity to dissect the diverse synaptic outputs of the interneuron RIM. I have revealed a role for RIM glutamate in spontaneous reversal behavior and have shown that RIM glutamate and RIM tyramine differentially regulate spontaneous reversals. Using direct optogenetic stimulation of RIM I have shown that RIM chemical synapses are essential regulators of reversal behavior.

Additionally, I have shown that RIM gap junctions and RIM chemical synapses have dual functionality, albeit in different ways. RIM chemical synapses generally work to decrease reversal frequency. However, they also increase reversal length and speed. RIM gap junctions inhibit reversals when RIM is hyperpolarized but promote reversals upon RIM depolarization.

Lastly, I used vesicular transporter pHluorin fusions to investigate the nature of RIM co-transmission. By extracting putative exo- and endocytosis events from spontaneous pHluorin dynamics I showed that RIM tyramine and RIM glutamate are likely released at the same time and share release and retrieval dynamics. My results suggest that RIM tyramine may additionally be released from distinct vesicles with slower release dynamics.

I conclude the diverse synaptic outputs of RIM allow it to organize multiple parameters of *C. elegans* reversal behavior during off-food foraging. I have also shown that RIM is a dual-functional node of the *C. elegans* locomotor circuitry, stabilizing both forward states and reversal states.

### How common are dual-function neurons?

Distinct neural populations are generally considered to promote a particular behavior or inhibit that behavior, but not to do both. However, it is possible that dual functionality is a common mechanism by which brains reorganize behavior modules to vary behavior with stimuli, behavioral states, and network states. It may also be a way in which brains generate behavioral variation while maintaining behavioral fidelity.

It is possible that the interconnectedness of the *C. elegans* nervous system increases dual functionality. However, dual functionality may also exist in larger nervous systems. Co-transmission of mammalian nervous systems sometimes occurs when different projections from a single neural population release different neurotransmitters onto different targets (Hnasko and Edwards, 2012, Vaaga et al., 2014). This could provide a mechanism for dual functionality in larger brains. While the study of mammalian co-transmission has focused on gross behavioral observations, such as general increase in

locomotion, and has often been studied in the context of pharmacologically-induced behaviors (Gras et al., 2008, Gaisler-Salomen et al., 2009, Mingote et al., 2017), more detailed study of endogenous behaviors and an increase in the diversity of behaviors studied may reveal a role for mammalian co-transmission in neuronal dual functionality.

Nevertheless, dual functionality does not depend on co-transmission, and could also manifest through other mechanisms, such as antagonistic mechanisms similar to that which I speculate exists between RIM and AIB. For instance, activation of a neural population may promote or inhibit a particular behavior dependent on the relative activities of multiple downstream targets.

Higher order dual functionality seems to exist in mammalian nervous systems and has recently been observed in the context of approach-avoidance conflict behavior. In this system, innate fear leads to avoidance behavior, but competing appetitive stimuli can incentivize mice to switch from avoidance to approach behavior (Miller et al., 2019). The medial amygdala is active during both of the behavioral states associated with avoidance and approach. When innate fear dominates over appetitive stimuli dopamine signaling to the medial amygdala is low, and a pathway from the medial amygdala to the bed nucleus of the stria terminalis is preferentially activated. Activation of this pathway promotes avoidance. However, appetitive stimuli increase dopamine release onto the medial amygdala, causing preferential activation of a second pathway from the medial amygdala to the ventromedial hypothalamus. Preferential activation of this pathway leads to approach behavior. Thus, the medial amygdala exhibits a dual functionality, promoting either approach or avoidance depending on behavioral state. However, the medial amygdala is upstream of the motor circuits that ultimately organize the complex locomotor patterns associated with approach and avoidance. It is yet to be seen whether downstream neurons more closely associated with these motor states also exhibit dual functionality.

In *C. elegans*, the interneuron AIA has recently been shown to be a dual-function neuron, having opposing effects on speed depending on the animal's behavioral state. Optogenetic activation of AIA increases crawling speed during dwelling and decreases crawling speed during roaming, providing evidence that *C. elegans* interneurons can both be dual functional and have state dependent effects on behavior (Ji et al., 2020). Unlike RIM, AIA is not thought to release more than one neurotransmitter, and the gap junctions it makes are with sensory neurons, not other interneurons.

Whether synaptic diversity is a common mechanism that allows bidirectional control over behavior is yet to be seen. Nevertheless, further functional and genetic dissection of synaptic outputs along with detailed behavioral analyses will facilitate a better understanding of how behavior is organized across contexts and nervous systems.

## METHODS

### Nematode Culture

Animals were grown at room temperature (21-22°C on the laboratory bench) or in a 20°C incubator on nematode growth media (NGM; 51.3 mM NaCl, 1.7% agar, 0.25% peptone, 1 mM CaCl<sub>2</sub>, 12.9 μM cholesterol, 1 mM MgSO<sub>4</sub>, 25 mM KPO<sub>4</sub>, pH 6) plates seeded with 200 μL of an *E. coli* OP50 bacterial liquid culture (Brenner, 1974). This OP50 liquid culture was obtained by picking a single OP50 colony into 100 mL of sterile LB and growing it on the bench top at room temperature for 48 hours without shaking or overnight in an incubator at 37°C without shaking, and subsequently storing it at 4°C. A the Bristol N2 strain was used as wild-type. All experiments were performed on young adult hermaphrodites, picked as L4 larvae the evening before an experiment.

We generated transgenic animals by microinjecting a transgene derived from the wild-type strain N2, a fluorescent co-injection marker (*myo-2p::mCherry*, *myo-3p::mCherry*, *elt-2p::nGFP*, *elt-2p::mCherry*), and empty pSM vector to reach a final DNA concentration of 100 ng/μL. When needed transgenes were integrated into the genome at random through exposure to ultraviolet radiation. Unless noted all mutant strains and strains containing integrated transgenes were backcrossed into wild-type to reduce background mutations. See Appendix for strain details.

### Off-food foraging Assay

Off-food foraging assays were performed and analyzed following López-Cruz et al. 2019. For all foraging assays, *E. coli* OP50 liquid culture used for generating homogeneous food lawns was grown at room temperature for almost all experimental sessions and used within 2 weeks of culturing. Homogeneous bacterial food lawns were grown by seeding NGM plates with a thin uniform OP50 bacterial lawn about 16 hours before the beginning of the assay. Lawns covered the entire plate and worms were constrained using filter paper soaked in 20 mM CuCl<sub>2</sub>. 20 adult hermaphrodites were habituated on this homogenous food lawn for 45 minutes prior to recording. 12-15 animals were then transferred to an unseeded standard NGM plate, cleaned of *E. coli* and transferred to a large (~80 cm<sup>2</sup>) unseeded NGM assay plate and restricted to the field of view using filter paper soaked in 20 mM CuCl<sub>2</sub>. Assay recordings began within 5-6 minutes from food removal to capture local search. We performed a minimum of 6 assays over two days for each experimental strain with control strains assayed in parallel. Animals were recorded for 45 minutes as previously described using a 15 MP PL-D7715 CMOS video camera (Pixelink). Frames were acquired at 3 fps using Streampix software (Norpix). We used 4 cameras to image 4 assays in parallel. For uniform illumination of the imaging plates we used identical LED backlights (Metaphase Technologies) and polarization sheets.

Animals were tracked using custom MATLAB software without manually linking tracks (López-Cruz et al. 2019, Pokala et al., 2014). We quantified reorientation frequencies by counting the number of times a worm did a particular reorientation during a 5-minute time bin, using only worms we could track for the entirety of the bin. Unless otherwise stated, mean reorientation frequencies were calculated over 5 minutes during

local search and divided by 5 to find the reorientation frequency per minute. For distributions of reversal length and speed we included all reversals tracked during the 45-minute assay. Reversal length is the pathlength of the animal in terms of the length of the animal. Reversal speed is the speed in mm/s and is an average of the mean and median of the centroid speed for the frames of the reversal, except for Figures 2-6D-E, 2-7A-B and 3-8D-E where the mean speed was calculated over a 4-minute time bin.

### **Behavioral Optogenetic Manipulations**

We activated neurons optogenetically using the red-shifted channel rhodopsin ReaChR (Lin et al., 2013). We cloned ReaChR into the pSM vector and used the *tdc-1* promoter to drive expression in RIM and RIC. Animals were stimulated during the off-food foraging assay described above and assays were performed following López-Cruz et al. Experimental animals were treated with 12.5  $\mu$ M all-trans retinal overnight and during habituation on homogeneous food lawns. Control animals were placed on overnight and habituation lawns made in parallel that did not contain retinal. We used a 525 nm a Solis HighPower LED (ThorLabs) controlled with custom MATLAB software to deliver optogenetic stimuli. For light titration experiments, we used a 5% duty cycle and delivered a light-pulse train of 2 pulses of  $\sim 5 \mu\text{W}/\text{mm}^2$  light, 2 pulses of  $\sim 25 \mu\text{W}/\text{mm}^2$  light, and 2 pulses of  $\sim 45 \mu\text{W}/\text{mm}^2$  light for 20 s each with a 100 s interpulse interval. These stimuli were delivered both 2 min into the assay and 32 min and 20 s into the assay to capture the local search and global search states, respectively. For all other experiments we used a 50% duty cycle and  $\sim 45 \mu\text{W}/\text{mm}^2$  light, with animals receiving 5 pulses of light with a 100 s interpulse interval during local search (2 min into the assay) and global search (30 min and 20 s into the assay). Recording hardware and software is identical to that of off-food foraging assays without optogenetic stimulation except that the optogenetic set up is only parallelized to accommodate 2 recordings at once.

For behavioral quantification, tracks were aligned around light pulses and tracks that were complete over the times being analyzed were used. Quantifications in Table 3-1 were made using the findpeaks() function in MATLAB.

### **Generating pHluorin Constructs**

We generated VMAT-pH by inserting super-ecliptic pHluorin into the first luminal loop of CAT-1 using the positioning described in Onoa et al., 2010: We aligned CAT-1 and rat VMAT2 based on homology using Protein BLAST and subsequently inserted pHluorin between arginine residue 99 and serine residue 100 (Onoa et al. described the VMAT2 insertion sites as glycine residue 113 and glycine residue 114, but based off of our alignment the residues are glycine residue 96 and glycine residue 97). We surrounded pHluorin with the optimal serine-glycine-threonine 5' and 3' linkers used by Onoa et al.:

5' linker: GSGGTGSTSGGSGGTGG

3' linker: SGGTGGSGGTGGSGGTGGSGGTG

We cloned our construct into the pSM vector by amplifying *cat-1* cDNA and the pHluorin gene from plasmids available in the lab using Phusion polymerase (New England Biolabs Inc.) and the following primers, followed by ligating them using restriction enzymes and T4 DNA Ligase from New England Biolabs Inc.

*cat-1* cDNA primers

NheI\_F1L: AGGAGAGCTAGCatgtcgtacattcttgattggatcagtacctatcggaacaatagg

KpnI\_R1L: AATATAGGTACCtctccaactgggccgatcgggttctcgtccaatcaatatcagc

KpnI\_F2L: AGGAGAGGTACCagtgagaggagaaaggagtcggacagaaaaatc

SacI\_R2L: AGGAGAGAGCTCctaaaatgcactgggtgcagagtacatattgtttgctgg

pHluorin primers

KpnI\_F1:

AGGAGAGGTACCggtacaggaggaacaggatcaacatcaggaggatcaggaggaacaggaggaatggga

agtaaaggagaagaactttc

KpnI\_R1:

ATAGGTACCtctgttctctctgatcctcctgttctctctgatcctcctgttctctctgatcctcctgttctctctgaaccggtt  
tgtatagttcatcc

We drove expression of VMAT-pH in RIM and RIC with the *tdc-1* promoter. We generated our VGLUT-pH construct by swapping the pDV47 *sra-6* promoter with the *tdc-1* promoter (Ventimiglia & Bargmann, 2017).

### Imaging pHluorin

We recorded pHluorin dynamics using epifluorescent microscopy optimized for pHluorin as in Ventimiglia and Bargmann 2017: All imaging was conducted on a Zeiss Axiovert 100TV wide-field microscope. Images were acquired through a 100x 1.4NA Zeiss APOCHROMAT objective onto an Andor ixon+ DU-987 EMCCD camera. Camera settings: 14-bit EM-GAIN enable digitizer (3 MHz). Baseline clamped. Overlapped recording mode. 0.3  $\mu$ S vertical clock speed. Binning = 1. Images were cropped to fit around the head of animal. Most experiments used a pre-amplifier gain of 5x. Illumination: Lumencore SOLA-LE solid-state LED lamp. Illumination input was passed through a 1.3 ND filter. Narrow bandwidth blue light illumination (484-492 nm) was produced using the CHROMA 49904-ET Laser Bandpass filter set (%T 90>).

Animals were cleaned of *E. coli* by crawling on an unseeded NGM plate, picked into *S. basal* buffer, and restrained in a microfluidic chip as described in Chronis, et al. 2007. Chips were flooded with 1 mM levamisole in *S. basal* to further prevent movement during acquisition.

### Extracting inferred pHluorin exo- and endo-cytosis events

I found the time derivative over 3 time points for data binned over 10 frames (2 s). I then chose parameters, including the change in time derivative and the amount of time over which the change should occur, that would best pull out on and off events, confirmed by eye. For VGLUT-pH and RIM::GCaMP, 2-3 non-responding traces were removed due to false event detection.

### **Fitting pHluorin Data**

Data were fit following Ventimiglia and Bargmann, 2017. Analyses were done in MATLAB. To fit to exocytosis data  $a \cdot (1 - \exp(-x/\tau))$  was used to a single exponential and  $a_1 \cdot (1 - \exp(-x/\tau_1)) + a_2 \cdot (1 - \exp(-x/\tau_2))$  was used to fit to a double exponential. For endocytosis:  $a \cdot \exp(-x/\tau)$ ; was used to fit to a single exponential and  $a_1 \cdot \exp(-x/\tau_1) + a_2 \cdot \exp(-x/\tau_2)$  was used to fit to a double exponential.

$AIC_c = n \cdot \log(SS/n) + 2 \cdot K + (2 \cdot K \cdot (K+1))/(n-K-1)$ ;  $n$  = number of data points,  $K$  = number of parameters, and  $SS$  = is the sum of the square of the vertical distances of the points from the curve.

$AIC_p = \exp(-.5 \cdot (AIC_c \text{ from double fit} - AIC_c \text{ from single fit})) / (1 + (\exp(-.5 \cdot (AIC_c \text{ from double fit} - AIC_c \text{ from single fit}))))$ ; Such that numbers close to 0 are best fit to single exponentials and numbers close to 1 are best fit to double exponentials.

Since extraction and fitting are imperfect, outliers were removed from halftime plots using nonlinear regression via the ROUT method in GraphPad Prism.

### **Statistical Analyses**

All statistical analyses were conducted in GraphPad Prism except for Kolmogorov Smirnov test, which was done using MATLAB. P values tend to be very low for the Kolmogorov Smirnov test when  $n$  is high, so the effect size was calculated for all distribution comparisons. Effect sizes of distributions are the D statistic of that test, which is the maximum distance between the empirical cumulative distributions of the data. For a summary of all  $n$  values in distributions, see Appendix B. For all significant  $p$  values not associated with distributions see Appendix C.

### **On-food foraging Assay**

*E. coli* OP50 liquid culture used for generating habituation and assay lawns was grown overnight at room temperature within one month of the assay and stored at 4°C. All bacterial lawns were seeded 14-16 hours before the start of the assay. Animals were habituated for a minimum of 40 minutes on a 50  $\mu$ L OP50 lawn, transferred to an unseeded standard NGM plate to be cleaned of food, and then individual animals were transferred outside of the assay lawn and allowed to crawl into the lawn. Assays were performed on NGM plates containing custom, laser-cut wells as described in Stern, Kirst, and Bargmann 2017, with 6 individual wells with a 10 mm diameter, allowing for worms to be tracked individually on bacterial lawns. Assay lawns were made by putting down 12  $\mu$ L of OP50 into each well and then immediately taking up 8  $\mu$ L. 60-minute video recordings were captured as described in Stern, Kirst, and Bargmann 2017: The imaging system consists of an array of six 8.8 MP USB3 cameras (Pointgrey, Flea3) and 35 mm high-resolution objectives (Edmund optics) mounted on optical construction rails (Thorlabs). Each camera images up to six individuals, capturing movies at 3 fps with a spatial resolution of  $\sim 10$   $\mu$ m. For uniform illumination of the imaging plates we used identical LED backlights (Metaphase Technologies) and polarization sheets. Movies from the cameras were captured using commercial software (FlyCapture,

Pointgrey) and saved on two computers (3 cameras per computer; each computer has a 4 core Intel i7 processor and 64 GB RAM). This system was duplicated such that 72 animals can be imaged during a single experimental session.

Animals were tracked using custom MATLAB software by Elias Scheer (unpublished). The first 20 minutes of data were excluded from analysis to minimize effects from picking. Roaming and dwelling states were found using a Hidden Markov Model as in Flavell et al. 2013 (Elias Scheer, unpublished). Only reversals that both began on food and after worms had been entirely inside the lawn for 2 frames were counted to eliminate reversals provoked by a lawn-boundary stimulus. Reversal length was determined based on how far the centroid of the animal moved during the reversal.



## **APPENDIX A: Effects of RIM chemical synapses during on-food foraging.**

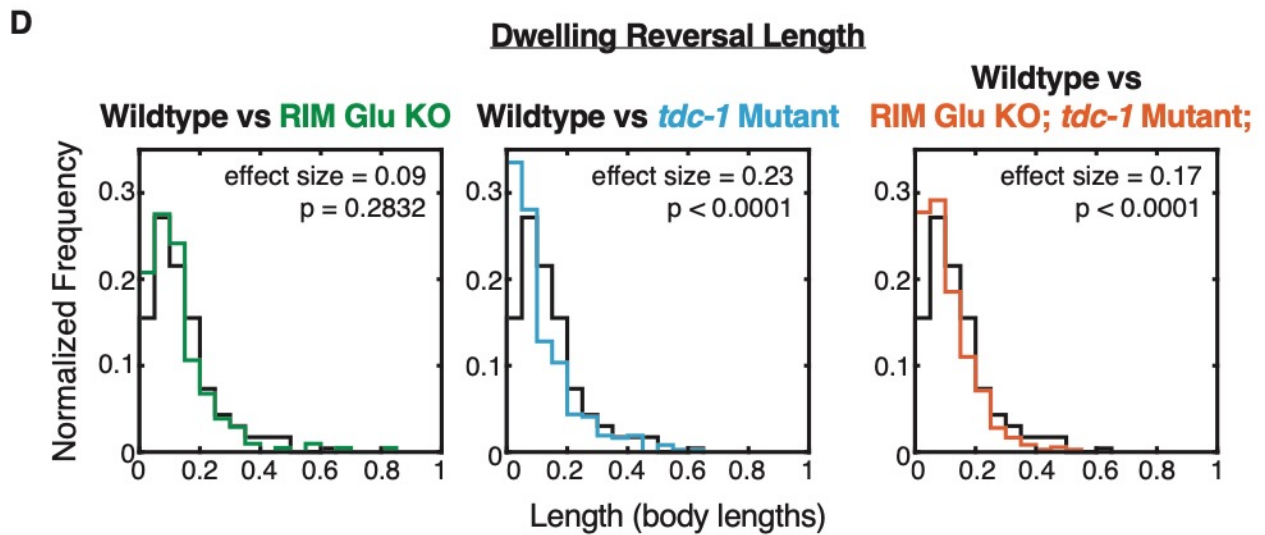
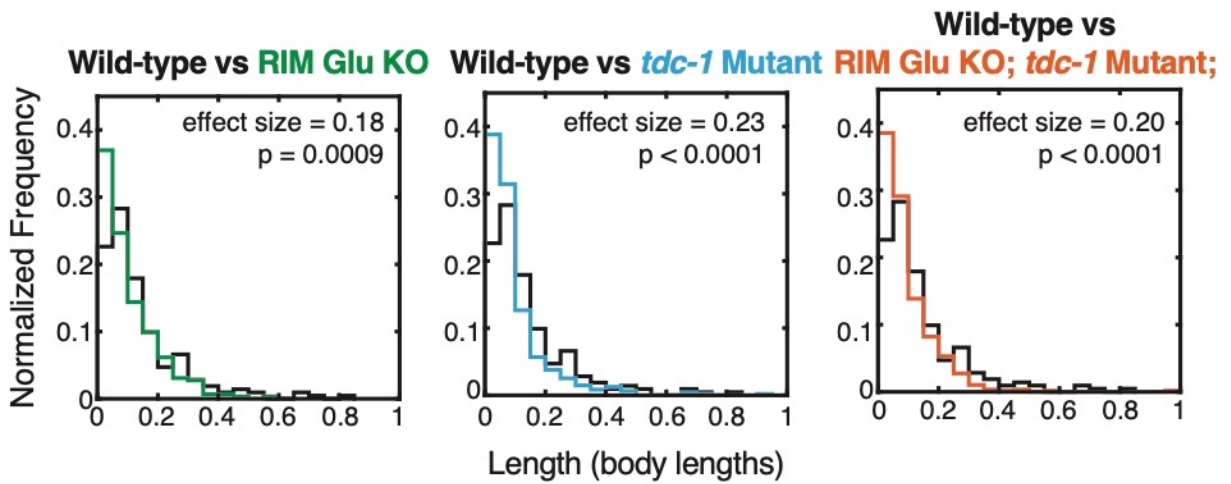
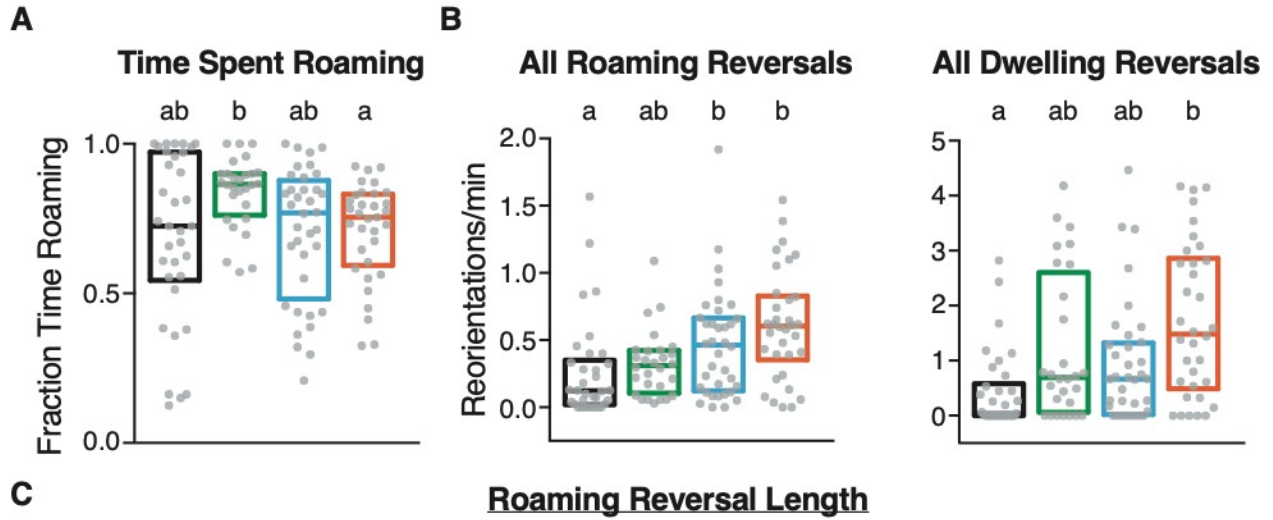
RIM ablation increases short reversals on and off of food, and experiments indicating that RIM activity decreases during reversals and RIM activation inhibits reversals were conducted on thin lawns of bacteria (Gray et al., 2005, Piggott et al., 2011).

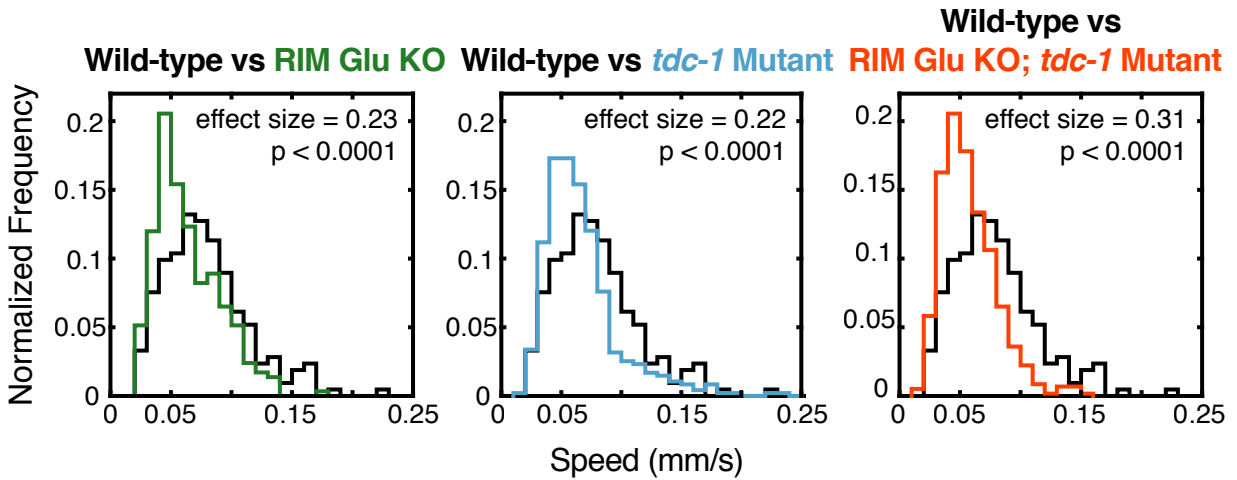
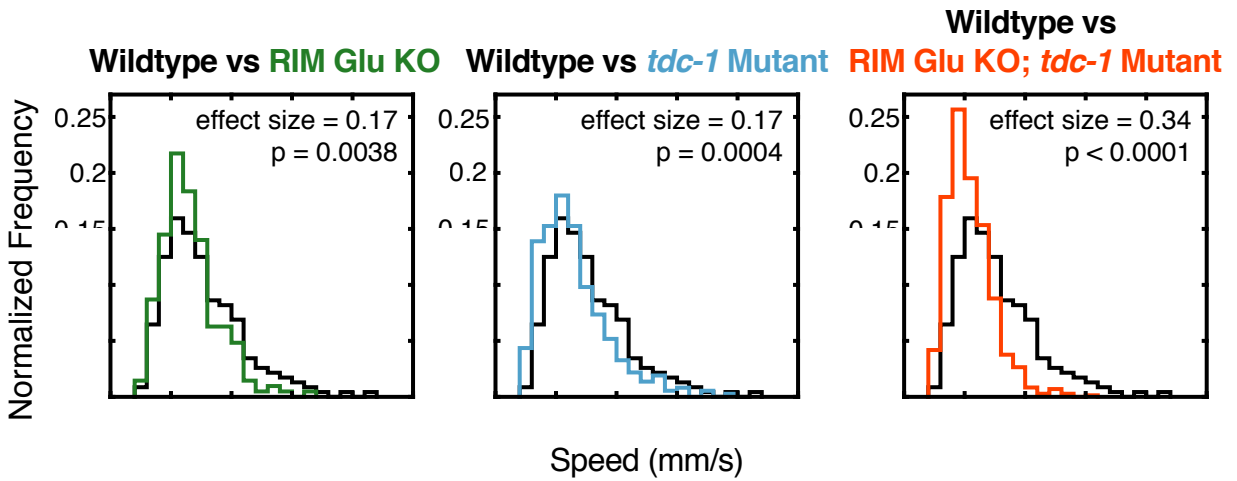
Additionally, RIM chemical synapses have been implicated in maintaining the on-food roaming behavioral state (Flavell et al., 2003). In collaboration with Elias Scheer, I performed preliminary experiments to clarify the effects of RIM's chemical synapses on on-food behavioral states and reversal behavior.

I habituated worms on bacterial food lawns grown identically to those used during the assay for ~40-60 minutes and tracked individual worms crawling on small bacterial lawns for 40 minutes using custom MATLAB software written by Elias (see Methods for details). I tested wild-type animals in parallel with RIM glu KO animals, *tdc-1* mutants, and double RIM glu KO; *tdc-1* mutants. I found that RIM chemical synapses had little effect on time spent roaming, with all deficient animals spending the same percent time roaming as wild-type (Figure A-1A). I also analyzed how RIM chemical synapses effect reversal frequency on food. Double RIM glu KO; *tdc-1* mutants had increased reversal frequency during both roaming and dwelling, and *tdc-1* mutants alone had increased reversals during roaming only. RIM chemical synapses decreased reversals during both roaming and dwelling. In contrast to off-food foraging, RIM glu KO alone did not affect on food reversal frequency.

I also did some preliminary analysis to determine if chemical outputs from RIM regulate reversal length and speed on food. Reversal length and speed do not change across behavioral states (data not shown). Tyramine has small effects on increasing reversal length during both roaming and dwelling, shifting length distributions slightly to the left compared to wildtype (Figure A-1C,D). Glutamate does not have effects on reversal length during either behavioral state. Both neurotransmitters have small effects on increasing reversal speed during roaming, but no effects during dwelling (Figure A-1E,F). In line with off-food results, RIM glu KO; *tdc-1* mutants were slower than animals lacking either neurotransmitter alone. I did not analyze whether forward speed was affected.

While preliminary, these results suggest that RIM is active on food and RIM chemical synapses may regulate some of the same reversal parameters they do off of food. Further experiments are needed to determine if RIM plays a role in the change in reversal behavior that occurs across food contexts.



**E****Roaming Reversal Speed****F****Dwelling Reversal Speed**

**Figure Appendix A-1. RIM chemical outputs may modulate on-food foraging states and reversals.**

Black = wild-type; green = RIM glu KO; blue = tdc-1 mutants; orange = RIM glu KO; tdc-1 mutants

- (A)** Fraction of time spent in the roaming state during 40-minutes of recording.
  - (B)** Frequency of all reversals during roaming (left) and dwelling (right).
  - (C)** Distributions of reversal length of all reversals during roaming over entire 40-minute recording normalized by probability.
  - (D)** Distributions of reversal length of all reversals during dwelling over entire 40-minute recording normalized by probability.
  - (E)** Distributions of reversal speed of all reversals during roaming over entire 40-minute recording normalized by probability.
  - (F)** Distributions of reversal speed of all reversals during dwelling over entire 40-minute recording normalized by probability.
- (A)** and **(B)** Each gray dot is a single animal. Boxes indicate mean and interquartile range. Different letters indicate statistical significance using a Kruskal-Wallis test with Dunn's multiple comparisons test.
- (C)** through **(F)** p is the significance of the difference of each experimental group compared to wildtype based on the Kolmogorov-Smirnov test, effect size is the D statistic.

**APPENDIX B. Table n of distributions and scatter plots.**

Transgene and genotype	Figure	All Reversals	Reversal Omegas	Long Reversal Omegas	Reversal Upsilons	Uncoupled Reversals
<u>Foraging</u>						
RIM::nFLP; wild-type	2-2, 2-8, 2-10	8851	3738	<i>3528</i>	1420	3693
RIM::nFLP; edited eat-4	2-2, 2-8, 2-10	13419	5471	<i>4719</i>	2242	5706
RIM::nFLP; tdc-1	2-2, 2-8, 2-10	11949	3051	<i>1914</i>	2677	6221
RIM::nFLP; edited eat-4; tdc-1	2-2, 2-8, 2-10	9282	2024	<i>1400</i>	1638	5620
wild-type (WT)	2-4	2985	<i>1100</i>	<i>962</i>		
pelt-2::nGFP; WT	2-4	3366	<i>1320</i>	<i>11121</i>		
pelt-2::nGFP; edited eat-4	2-4	3008	<i>1145</i>	<i>920</i>		
pelt-2::nGFP; RIM::nFLP; WT	2-4	3078	<i>1107</i>	<i>972</i>		
wild-type (WT)	2-5	3139	<i>1372</i>	<i>1006</i>		
tbh-1	2-5	1935	<i>1006</i>	<i>811</i>		
wild-type (WT)	2-6	3584	<i>1402</i>	<i>1095</i>		
ptdc-1::Tetanus toxin	2-6	6268	<i>1207</i>	<i>539</i>		
coel::GFP	3-8	2355	<i>1032</i>	<i>913</i>		
RIM::unc-1(n494)	3-8	5062	<i>1342</i>	<i>1101</i>		
wild-type (WT)		6308	<i>2819</i>	<i>2036</i>		
RIM::EAT-4::pHluorin		5627	<i>2388</i>	<i>1806</i>		
RIM::CAT-1::pHluorin		5382	<i>2442</i>	<i>1694</i>		
<u>Optogenetics</u>						
RIM::nFLP; RIM::ReaChR; wild-type	3-6			Local search = 85; Global search = 64		
RIM::nFLP; RIM::ReaChR; edited eat-4	3-6			Local search = 51; Global search = 52		
RIM::nFLP; RIM::ReaChR; tdc-1	3-6			Local search = 61; Global search = 46		
RIM::nFLP; RIM::ReaChR; edited eat-4; tdc-1	3-6			Local search = 64; Global search = 46		
RIM::ReaChR	3-10			Local search = 67; Global search = 54		
RIM::ReaChR; RIM::unc-1(n494)	3-10			Local search = 39; Global search = 25		
RIM::nFLP; RIM::ReaChR; wild-type	3-7	<i>8110</i>	<i>2491</i>	2167		
RIM::nFLP; RIM::ReaChR; edited eat-4	3-7	<i>6681</i>	<i>2397</i>	1889		
RIM::nFLP; RIM::ReaChR; tdc-1	3-7	<i>7636</i>	<i>1398</i>	970		
RIM::nFLP; RIM::ReaChR; edited eat-4; tdc-1	3-7	<i>7550</i>	<i>1257</i>	751		
ptdc-1::ReaChR::SL2::GFP; myo-3::mCherry	3-11	<i>7809</i>	<i>2064</i>	1729		
RIM::ReaChR; RIM::unc-1(n494)	3-11	<i>7194</i>	<i>1205</i>	915		

Italics indicate data not shown in any figure.

## APPENDIX C. p-Values of statistically significant data.

p Values of statistically significant data				
Figure; Panel	Comparison	Summary	Adjusted p Value	Test
2-2A; left	WT vs RIM glu KO	****	<0.0001	Kruskal-Wallis; Dunn's correction
2-2A; left	WT vs tdc-1	****	<0.0001	Kruskal-Wallis; Dunn's correction
2-2A; left	WT vs RIM glu KO; tdc-1	***	0.001	Kruskal-Wallis; Dunn's correction
2-2A; middle	WT vs RIM glu KO	****	<0.0001	Kruskal-Wallis; Dunn's correction
2-2A; middle	RIM glu KO vs tdc-1	**	0.0011	Kruskal-Wallis; Dunn's correction
2-2A; middle	RIM glu KO vs RIM glu KO;tdc-1	****	<0.0001	Kruskal-Wallis; Dunn's correction
2-2A; right	WT vs RIM glu KO	***	0.0006	Kruskal-Wallis; Dunn's correction
2-2A; right	WT vs tdc-1	****	<0.0001	Kruskal-Wallis; Dunn's correction
2-2A; right	WT vs RIM glu KO; tdc-1	****	<0.0001	Kruskal-Wallis; Dunn's correction
2-2A; right	RIM glu KO vs tdc-1	***	0.0004	Kruskal-Wallis; Dunn's correction
2-4A; left	WT vs elt-2p::elt-2; WT	**	0.0021	Mann-Whitney
2-6A; left	WT vs tdc-1p::tetanus toxin	**	0.007	Mann-Whitney
2-6A; right	WT vs tdc-1p::tetanus toxin	***	0.0002	Mann-Whitney
2-6D	WT vs tdc-1p::tetanus toxin	***	0.0002	Mann-Whitney
2-6E	WT vs tdc-1p::tetanus toxin	**	0.0047	Mann-Whitney
2-7A	WT vs tdc-1	****	<0.0001	Kruskal-Wallis; Dunn's correction
2-7A	WT vs RIM glu KO; tdc-1	****	<0.0001	Kruskal-Wallis; Dunn's correction
2-7A	RIM glu KO vs tdc-1	***	0.0001	Kruskal-Wallis; Dunn's correction
2-7A	RIM glu KO vs RIM glu KO;tdc-1	****	<0.0001	Kruskal-Wallis; Dunn's correction
2-7B	WT vs tdc-1	*	0.0114	Kruskal-Wallis; Dunn's correction
2-7B	WT vs RIM glu KO; tdc-1	****	<0.0001	Kruskal-Wallis; Dunn's correction
2-7B	RIM glu KO vs tdc-1	****	<0.0001	Kruskal-Wallis; Dunn's correction
2-7B	tdc-1 vs RIM glu KO; tdc-1	*	0.0111	Kruskal-Wallis; Dunn's correction
2-7C; Reverse	WT vs tdc-1	***	0.0005	Friedman; Dunn's correction
2-7C; Reverse	WT vs RIM glu KO; tdc-1	****	<0.0001	Friedman; Dunn's correction
2-7C; Reverse	RIM glu KO vs RIM glu KO;tdc-1	****	<0.0001	Friedman; Dunn's correction
2-7C; Forward	WT vs RIM glu KO; tdc-1	***	0.0002	Friedman; Dunn's correction
2-7C; Forward	RIM glu KO vs RIM glu KO;tdc-1	**	0.0031	Friedman; Dunn's correction
2-8B; left	WT vs RIM glu KO	*	0.0274	Kruskal-Wallis; Dunn's correction
2-8B; left	WT vs tdc-1	*	0.0395	Kruskal-Wallis; Dunn's correction
2-8B; left	RIM glu KO vs tdc-1	****	<0.0001	Kruskal-Wallis; Dunn's correction
2-8B; left	RIM glu KO vs RIM glu KO;tdc-1	****	<0.0001	Kruskal-Wallis; Dunn's correction
2-8B; right	WT vs tdc-1	****	<0.0001	Kruskal-Wallis; Dunn's correction
2-8B; right	WT vs RIM glu KO; tdc-1	****	<0.0001	Kruskal-Wallis; Dunn's correction
2-8B; right	RIM glu KO vs tdc-1	****	<0.0001	Kruskal-Wallis; Dunn's correction
2-8B; right	RIM glu KO vs RIM glu KO;tdc-1	****	<0.0001	Kruskal-Wallis; Dunn's correction
2-8D	WT vs RIM glu KO	****	<0.0001	Kruskal-Wallis; Dunn's correction

2-8D	RIM glu KO vs tdc-1	****	<0.0001	Kruskal-Wallis; Dunn's correction
2-8D	RIM glu KO vs RIM glu KO;tdc-1	****	<0.0001	Kruskal-Wallis; Dunn's correction
2-8E; left	WT vs RIM glu KO; tdc-1	****	<0.0001	Kruskal-Wallis; Dunn's correction
2-8E; left	RIM glu KO vs RIM glu KO;tdc-1	****	<0.0001	Kruskal-Wallis; Dunn's correction
2-8E; right	WT vs RIM glu KO	*	0.0368	Kruskal-Wallis; Dunn's correction
2-8E; right	RIM glu KO vs RIM glu KO;tdc-1	**	0.0015	Kruskal-Wallis; Dunn's correction
2-9B; left	WT vs RIM glu KO	*	0.0177	Kruskal-Wallis; Dunn's correction
2-9B; left	RIM glu KO vs tdc-1	**	0.0032	Kruskal-Wallis; Dunn's correction
2-9B; left	RIM glu KO vs RIM glu KO;tdc-1	****	<0.0001	Kruskal-Wallis; Dunn's correction
2-9B;right	WT vs RIM glu KO; tdc-1	*	0.0443	Kruskal-Wallis; Dunn's correction
2-9B;right	RIM glu KO vs RIM glu KO;tdc-1	***	0.001	Kruskal-Wallis; Dunn's correction
2-9C	WT vs RIM glu KO	****	<0.0001	Kruskal-Wallis; Dunn's correction
2-9C	WT vs tdc-1	****	<0.0001	Kruskal-Wallis; Dunn's correction
2-9C	WT vs RIM glu KO; tdc-1	**	0.0034	Kruskal-Wallis; Dunn's correction
2-9D; left	WT vs RIM glu KO; tdc-1	****	<0.0001	Kruskal-Wallis; Dunn's correction
2-9D; left	RIM glu KO vs tdc-1	****	<0.0001	Kruskal-Wallis; Dunn's correction
2-9D; left	RIM glu KO vs RIM glu KO;tdc-1	*	0.02	Kruskal-Wallis; Dunn's correction
2-9D; middle	WT vs RIM glu KO; tdc-1	*	0.0368	Kruskal-Wallis; Dunn's correction
2-9D; middle	RIM glu KO vs RIM glu KO;tdc-1	**	0.0015	Kruskal-Wallis; Dunn's correction
2-9D; right	WT vs RIM glu KO	***	0.0004	Kruskal-Wallis; Dunn's correction
2-9D; right	WT vs tdc-1	****	<0.0001	Kruskal-Wallis; Dunn's correction
2-9D; right	WT vs RIM glu KO; tdc-1	***	0.0008	Kruskal-Wallis; Dunn's correction
3-4C	5: LS vs GS	**	0.002	Mann-Whitney
3-4G; left	Local Search: 5 vs 25	**	0.0019	Kruskal-Wallis; Dunn's correction
3-4G; left	Local Search: 5 vs 45	****	<0.0001	Kruskal-Wallis; Dunn's correction
3-4G; right	Global Search: 5 vs 25	**	0.0013	Kruskal-Wallis; Dunn's correction
3-4G; right	Global Search: 5 vs 45	****	<0.0001	Kruskal-Wallis; Dunn's correction
3-5F; left	Local Search: 5 vs 25	*	0.0357	Kruskal-Wallis; Dunn's correction
3-5F; left	Local Search: 5 vs 45	**	0.0024	Kruskal-Wallis; Dunn's correction
3-5F; right	Global Search: 5 vs 45	**	0.0013	Kruskal-Wallis; Dunn's correction
3-8A; left	WT vs RIM gap junction KD	**	0.0022	Mann-Whitney
3-8A; middle	WT vs RIM gap junction KD	**	0.0022	Mann-Whitney
3-8A; right	WT vs RIM gap junction KD	**	0.0022	Mann-Whitney
3-9B	WT vs RIM gap junction KD	*	0.0411	Mann-Whitney
3-10B; left	WT vs RIM gap junction KD	****	<0.0001	Mann-Whitney
4-7C; right	VGLUT-pH vs VMAT-pH	**	0.0062	Mann-Whitney
A-1A	RIM glu KO vs RIM glu KO; tdc-1	*	0.0240	Kruskal-Wallis; Dunn's correction
A-1B; left	WT vs tdc-1	*	0.0107	Kruskal-Wallis; Dunn's correction
A-1B; left	WT vs RIM glu KO; tdc-1	****	<0.0001	Kruskal-Wallis; Dunn's correction
A-1B; right	WT vs RIM glu KO; tdc-1	***	0.0002	Kruskal-Wallis; Dunn's correction

## APPENDIX D. List of Strains.

Strain Name	Transgene, genotype, etc.	Figures	Notes
CX17882	ptdc-1::nFLP; wild-type; elt2p::nGFP	2-2, 2-3, 2-7, 2-8, 2-9, 2-10	
CX17881	ptdc-1::nFLP; edited eat-4; elt2p::nGFP	2-2, 2-3, 2-7, 2-8, 2-9, 2-10	
CX17883	ptdc-1::nFLP; tdc-1(n3419); elt2p::nGFP	2-2, 2-3, 2-7, 2-8, 2-9, 2-10	
CX17884	ptdc-1::nFLP; edited eat-4; tdc-1(n3419); elt2p::nGFP	2-2, 2-3, 2-7, 2-8, 2-9, 2-10	
CX0007	wild-type (WT)	2-4	
CX18118	pelt-2::nGFP; WT	2-4	Original strain used in experiments lost.
NA	pelt-2::nGFP; edited eat-4	2-4	Strain used in experiments lost.
CX0001	wild-type (WT)	2-5, 2-6	
MT9455	tbh-1(n3247)	2-5	
CX14993	ptdc-1::Tetanus toxin::SL2::mCherry	2-6	
CX17546	coel::GFP	3-8, 3-9	
CX14853	ptdc-1::unc-1(n494)::SL2::mCherry; coel::GFP	3-8, 3-9	
CX17442	ptdc-1::EAT-4::pHluorin; coel::dsred	4-2, 4-3, 4-5, 4-6, 4-7, 4-8, 4-9, 4-10	
CX17443	ptdc-1::CAT-1::pHluorin; coel::dsred	4-2, 4-3, 4-5, 4-6, 4-7, 4-8, 4-9, 4-10	
CX16665	ptdc-1::GCAMP3.0; coel::dsred	4-4	
CX17885	ptdc-1::nFLP; wild-type; ptdc-1::ReaChR::SL2::GFP; myo-3::mCherry	3-4, 3-5, 3-6, 3-7	
CX17886	ptdc-1::nFLP; edited eat-4; ptdc-1::ReaChR::SL2::GFP; myo-3::mCherry	3-6, 3-7	
CX17887	ptdc-1::nFLP; tdc-1(n3419); ptdc-1::ReaChR::SL2::GFP; myo-3::mCherry	3-6, 3-7	
CX17888	ptdc-1::nFLP; edited eat-4; tdc-1(n3419); ptdc-1::ReaChR::SL2::GFP; myo-3::mCherry	3-6, 3-7	
CX17694	ptdc-1::ReaChR::SL2::GFP; myo-3::mCherry	3-1, 3-2, 3-3, 3-10, 3-11	
CX17694 x CX14853	tdc-1::unc-1(n494)::SL2::mCherry; coel::GFP; ptdc-1::ReaChR::SL2::GFP; myo-3::mCherry	3-10, 3-11	



## REFERENCES

- Ache, J. M., Polsky, J., Alghailani, S., et al. Neural basis for looming size and velocity encoding in the *Drosophila* giant fiber escape pathway. *Current Biology* 29, 1073-1081 (2019).
- Aguilar, A., Dunn, M., Mingote, S., et al., Neuronal depolarization drives increased dopamine synaptic vesicle loading via VGLUT. *Neuron* 95(5), 1074-1088 (2017).
- Alabi, A. A. & Tsien, R. W. Synaptic Vesicle Pools and Dynamics. *Cold Spring Harb Perspect Biol* 4. a013680 (2012).
- Alkema, M. J., Hunter-Ensor, M., Ringstad, N., & Horvitz, H. R. Tyramine functions independently of octopamine in the *Caenorhabditis elegans* nervous system. *Neuron* 46, 247-260 (2005).
- Ardiel, E. L., McDiarmid, T. A., Timbers, T. A., et al., CaMK (CMK-1) and O-GlcNAc transferase (OGT-1) modulate mechanosensory responding and habituation in an interstimulus interval-dependent manner in *Caenorhabditis elegans*. *bioRxiv* 115972 (2018).
- Baidya M., Genovez M., Torres M., & Chao M.Y. Dopamine Modulation of Avoidance Behavior in *Caenorhabditis elegans* Requires the NMDA Receptor NMR-1. *PLoS ONE* 9(8), e102958 (2014).
- Bargmann, C. I., Thomas, J. H., & Horvitz, H. R. Chemosensory cell function in the behavior and development of *Caenorhabditis elegans*. *Cold Spring Harb Symp Quant Biol* 55, 529-538 (1990).
- Ben Arous, J., Laffont, S., & Chatenay, D. Molecular and sensory basis of a food related two-state behavior in *C. elegans*. *PLoS ONE* 4(10), e7584 (2009).
- Berger, A. J., Hart, A. C., & Kaplan, J. M. G<sub>s</sub>-Induced Neurodegeneration in *Caenorhabditis elegans*. *J. Neurosci.* 18(8), 2871–2880 (1998).
- Bhattacharya, A., Aghayeva, U., Berghoff, E. G., & Hobert, O. Plasticity of the Electrical Connectome of *C. elegans*. *Cell* 176, 1174–1189 (2019).
- Brenner, S. The genetics of *Caenorhabditis elegans*. *Genetics* 77(1), 71-94 (1974).
- Brockie, P. J., Madsen, D. M., Zheng, Y., Mellem, J., & Maricq, A. V. Differential Expression of Glutamate Receptor Subunits in the Nervous System of *Caenorhabditis elegans* and Their Regulation by the Homeodomain Protein UNC-42. *J. Neurosci.* 21(5), 1510-1522 (2001).

Bruns, D. & Jahn, R. Real-time measurement of transmitter release from single synaptic vesicles. *Nature* 375(6544), 62-65 (1995).

Burendei, B., Shinozaki, R., Watanabe, M., et al., Cryo-EM structures of undocked innexin-6 hemichannels in phospholipids. *Science Advances* 6(7), eaax3157 (2020).

Burnstock, G., Do some nerve cells release more than one neurotransmitter? *Neuroscience* 1, 239-248 (1976).

Burnstock, G. Cotransmission. *Curr Opin Pharmacol.* 4(1), 47-52 (2004).

Calhoun, A. J., Chalasani, S. H., & Sharpee, T. O. Maximally informative foraging by *Caenorhabditis elegans*. *eLife* 3, e04220 (2014).

Chalasani, S. H., Chronis, N., Tsunozaki, M., et al. Dissecting a circuit for olfactory behaviour in *Caenorhabditis elegans*. *Nature* 450, 63–70 (2007).

Chalfie, M., Sulston, J. E., White, J. G., et al. The neural circuit for touch sensitivity in *Caenorhabditis elegans*. *J Neurosci.* 5(4), 956-964 (1985).

Chao, M. Y., Komatsu, H., Fukuto, H. S., Dionne, H. M., & Hart, A. C. Feeding status and serotonin rapidly and reversibly modulate a *Caenorhabditis elegans* chemosensory circuit. *Proc Natl Acad Sci U S A* 101(43), 15512-15517 (2004).

Chen, B., Liu, Q., Ge, Q., Xie, J., & Wang, Z-W. UNC-1 Regulates Gap Junctions Important to Locomotion in *C. elegans*. *Current Biology* 17, 1334-1339 (2007).

Choi, S., Taylor, K. P., Chatzigeorgiou, M., et al. Sensory Neurons Arouse *C. elegans* Locomotion via Both Glutamate and Neuropeptide Release. *PLoS Genet.* 11(7), e1005359 (2015).

Chronis, N., Zimmer, M. & Bargmann, C. Microfluidics for in vivo imaging of neuronal and behavioral activity in *Caenorhabditis elegans*. *Nat Methods* 4, 727–731 (2007).

Cook, S.J., Jarrell, T.A., Brittin, C.A., et al. Whole-animal connectomes of both *Caenorhabditis elegans* sexes. *Nature* 571, 63–71 (2019).

Croll, N. A. Components and patterns in the behaviour of the nematode *Caenorhabditis elegans*. *J. Zool., Lond.* 176, 159-176 (1975).

Dillon, J., Franks, C. J., Murray, C., et al. Metabotropic glutamate receptors: modulators of context-dependent feeding behaviour in *C. elegans*. *Journal of Biological Chemistry* 290(24), 15052-15065 (2015).

Dittman, J. S. Unc13: A multifunctional synaptic marvel. *Curr Opin Neurobiol.* 57,17-25 (2019).

Duerr, J. S., Frisby, J. L., Gaskin, J., et al. The cat-1 gene of *Caenorhabditis elegans* encodes a vesicular monoamine transporter required for specific monoamine-dependent behaviors. *J Neurosci.* 19(1), 72-84 (1999).

Donnelly, J.L., Clark, C.M., Leifer, A.M., et al. Monoaminergic Orchestration of Motor Programs in a Complex *C. elegans* Behavior. *PLoS Biol.* 11(4), e1001529 (2013).

Duistermars, B. J., Pfeiffer, B. D., Hoopfer, E. D., & Anderson, D. J. A Brain Module for Scalable Control of Complex, Multi-motor Threat Displays. *Neuron* 100, 1474–1490 (2018).

Ezcurra, M., Tanizawa, Y., Swoboda, P., & Schafer, W. R. Food sensitizes *C. elegans* avoidance behaviours through acute dopamine signalling. *EMBO J.* 30(6), 1110–1122 (2011).

Faisal, A. A., Selen, L. P., & Wolpert, D. M. Noise in the nervous system. *Nat Rev Neurosci.* 9, 292-303 (2008).

Fei H., & Krantz ,D.,E. Vesicular Neurotransmitter Transporters. In: Lajtha A., Mikoshiba K. (eds) *Handbook of Neurochemistry and Molecular Neurobiology.* Springer, Boston, MA (2009)

Flavell, S. W., Pokala, N., Macosko, E. Z., et al. Serotonin and the neuropeptide PDF initiate and extend opposing behavioral states in *C. elegans*. *Cell* 154(5), 1023-1035 (2013).

Fontanini, A. & Katz, D. B. 7 to 12 Hz activity in rat gustatory cortex reflects disengagement from a fluid self-administration task. *J. Neurophysiol.* 93(5), 2832-40 (2004).

Fontanini, A. & Katz, D. B. Behavioral states, network states, and sensory response variability. *J. Neurophysiol.* 100(3), 1160-8 (2008).

Fortin, G. M., Bourque, M. J., Mendez, J. A., et al. Glutamate corelease promotes growth and survival of midbrain dopamine neurons. *J. Neurosci.* 32(48), 17477-91 (2012).

Fu, J., Zhang, H., Huang, W., et al., AIM interneurons mediate feeding suppression through the TYRA-2 receptor in *C. elegans*. *Biophysics Reports* 4, 17-24 (2018).

Fujiwara, M., Sengupta, P., & McIntire, S. L. Regulation of body size and behavioral state of *C. elegans* by sensory perception and the EGL-4 cGMP-dependent protein kinase. *Neuron* 36(6), 1091-102 (2002).

Gaisler-Salomon, I. Miller, G. M., Chuhma, N., et al. Glutaminase-deficient mice display hippocampal hypoactivity, insensitivity to pro-psychotic drugs and potentiated latent inhibition: relevance to schizophrenia. *Neuropsychopharmacology* 34(10), 2305-22 (2009).

Garcia-Rill, E., Heister, D. S., Ye, M., Charlesworth, A., & Hayer, A. Electrical coupling: Novel mechanisms for sleep-wake control. *Sleep* 30(11), 1405-1414 (2007).

Ghosh, D. D., Sanders, T., Hong, S., et al. Neural Architecture of Hunger-Dependent Multisensory Decision Making in *C. elegans*. *Neuron* 92(5), 1049-1062 (2016).

Ghosh, R., Mohommadi, A., Kruglyak, L., & Ryu, W. S. Multiparameter behavioral profiling reveals distinct thermal response regimes in *Caenorhabditis elegans*. *BMC Biol* 10, 85 (2012).

Ghosh, R., Bloom, J. S., Mohamaddi, A., et al. Genetics of Intraspecies Variation in Avoidance Behavior Induced by a Thermal Stimulus in *Caenorhabditis elegans*. *Genetics* 200(4), 1327-90 (2015).

Gjorgjieva, J. Biron, D., & Haspel, G. Neurobiology of *Caenorhabditis elegans* Locomotion: Where Do We Stand? *Bioscience* 64(6), 476-486 (2014).

Gordus, A., Pokala, N., Levy, S., Flavell, S. W. & Bargmann, C. I. Feedback from network states generates variability in a probabilistic olfactory circuit. *Cell* 161, 215–227 (2015).

Gras, C., Amilhon, B., Lepicard, E., M., et al., The vesicular glutamate transporter VGLUT3 synergizes striatal acetylcholine tone. *Nat Neurosci.* 11(3), 292-300 (2008).

Gray, J. M., Hill, J. J., & Bargmann, C. I. A circuit for navigation in *Caenorhabditis elegans*. *Proc Natl Acad Sci U S A* 102(9), 3184-3191 (2005).

Guo, Z. V., Hart, A. C., & Ramanathan, S. Optical interrogation of neural circuits in *Caenorhabditis elegans*. *Nat Methods* 6(12), 891-6 (2009).

Hapiak, V., Summers, P. Ortega, A. et al. Neuropeptides Amplify and Focus the Monoaminergic Inhibition of Nociception in *Caenorhabditis elegans*. *J Neurosci.* 33(35), 14107-14116 (2013).

- Harris, G., Mills, H., Wragg, R., et al. The Monoaminergic Modulation of Sensory-Mediated Aversive Responses in *Caenorhabditis elegans* Requires Glutamatergic/Peptidergic Cotransmission. *J Neurosci.* 30(23), 7889-7899 (2010).
- Hart, A. C., Sims, S., & Kaplan, J. M. Synaptic code for sensory modalities revealed by *C. elegans* GLR-1 glutamate receptor. *Nature* 378, 82–85 (1995).
- Hart, A. C., Kass, J., Shapiro, J. E., & Kaplan, J. M. Distinct signaling pathways mediate touch and osmosensory responses in a polymodal sensory neuron. *J Neurosci.* 19(6), 1952-1958 (1999).
- Hills, T., Brockie, P. J. & Maricq, A. V. Dopamine and Glutamate Control Area-Restricted Search Behavior in *Caenorhabditis elegans*. *J. Neurosci.* 24, 1217–1225 (2004).
- Hnasko, T. S., Chuhma, N., Zhang, H., et al. Vesicular glutamate transport promotes dopamine storage and glutamate corelease in vivo. *Neuron* 65(5), 643-56 (2010).
- Hnasko, T. S., & Edwards, R. H. Neurotransmitter corelease: mechanism and physiological role. *Annu Rev Physiol.* 74, 225-43 (2012).
- Hori, S., Oda, S., Suehiro, Y., Iino, Y., & Mitani, S. OFF-responses of interneurons optimize avoidance behaviors depending on stimulus strength via electrical synapses. *PLoS Genet* 14(6), e1007477 (2018).
- Hoopfer, E. D., Jung, Y., Inagaki, H. K., Rubin, G. M., Anderson, D. J. P1 interneurons promote a persistent internal state that enhances inter-male aggression in *Drosophila*. *Elife* 4, e11346 (2015).
- Huang, K-M., Cosman, P., & Schafer, W. R. Machine vision based detection of omega bends and reversals in *C. elegans*. *Journal of Neuroscience Methods.* 158, 323-36 (2006).
- Iino, Y. & Yoshida, K. Parallel Use of Two Behavioral Mechanisms for Chemotaxis in *Caenorhabditis elegans*. *J. Neurosci.* 29, 5370–5380 (2009).
- Jang, H., Levy, S., Flavell, S. W., et al. Dissection of neuronal gap junction circuits that regulate social behavior in *Caenorhabditis elegans*. *Proc. Natl. Acad. Sci.* 114, E1263–E1272 (2017).
- Ji, N., Madan, G. K., Fabre, G. I., et al. A neural circuit for flexible control of persistent behavioral states. *bioRxiv* 2020.02.04.934547 (2020).

- Jin, X. Pokala, N., & Bargmann, C. I. Distinct Circuits for the Formation and Retrieval of an Imprinted Olfactory Memory. *Cell* 164, 632–643 (2016).
- Jung, Y., Kennedy, A., Chiu, H., Mohammad, F., Claridge-Chang, A., & Anderson, D. J. Neurons that Function within an Integrator to Promote a Persistent Behavioral State in *Drosophila*. *Neuron* 2, 322-333 (2020).
- Kagawa-Nagamura, Y., Gengyo-Ando, K., Ohkura, M., & Nakai, J. Role of tyramine in calcium dynamics of GABAergic neurons and escape behavior in *Caenorhabditis elegans*. *Zoological Lett.* 4, 19 (2018).
- Kang, C. & Avery, L. Systemic regulation of starvation response in *Caenorhabditis elegans*. *Genes Dev* 23(1), 12-17 (2009).
- Kaplan, J. M. & Horvitz, H. R. A dual mechanosensory and chemosensory neuron in *Caenorhabditis elegans*. *Proc Natl Acad Sci U S A* 90(6), 2227-31 (1993).
- Kaplan, H. S., Nichols, A. L. A., & Zimmer, M. Sensorimotor integration in *Caenorhabditis elegans*: a reappraisal towards dynamic and distributed computations. *Philos Trans R Soc Lond B Biol Sci.* 373(1758), 20170371 (2018).
- Kato, S., Kaplan, H. S., Schrödel, T. et al. Global Brain Dynamics Embed the Motor Command Sequence of *Caenorhabditis elegans*. *Cell* 163, 656–669 (2015).
- Katz, M. Corson, F., Keil, W., et al. Glutamate spillover in *C. elegans* triggers repetitive behavior through presynaptic activation of MGL-2/mGluR5. *Nat Commun.* 10(1), 1882 (2019).
- Krantz, D., E., Waites, C., Oorschot, V., et al. A Phosphorylation Site Regulates Sorting of the Vesicular Acetylcholine Transporter to Dense Core Vesicles. *J Cell B* 149(2): 379–396 (2000).
- Lee, R. Y., Sawin, E. R., Chalfie, M., Horvitz, H. R., Avery, L. EAT-4, a homolog of a mammalian sodium-dependent inorganic phosphate cotransporter, is necessary for glutamatergic neurotransmission in *Caenorhabditis elegans*. *J Neurosci.* 19(1), 159-67 (1999).
- Lee, H., Kim, D. W., Remedios, R., et al. Scalable control of mounting and attack by *Esr1+* neurons in the ventromedial hypothalamus. *Nature* 509(7502), 627-32 (2014).
- Li, W., Kang, L., Piggott, B. J., Feng, Z., & Xu, X. Z. The neural circuits and sensory channels mediating harsh touch sensation in *Caenorhabditis elegans*. *Nat Commun.* 2, 315 (2011).

Li, Z., Li, Y., Yi, Y., et al. Dissecting a central flip-flop circuit that integrates contradictory sensory cues in *C. elegans* feeding regulation. *Nat Commun.* 3, 776 (2012).

Li, A., Guthman, E. M., Doucette, W. T., & Restrepo, D. Behavioral Status Influences the Dependence of Odorant-Induced Change in Firing on Prestimulus Firing Rate. *J Neurosci.* 37(7), 1835–1852 (2017).

Lin, J. Y., Knutsen, P. M., Muller, A., Kleinfeld, D., & Tsien, R. Y. ReaChR: a red-shifted variant of channelrhodopsin enables deep transcranial optogenetic excitation. *Nat Neurosci.* 6(10), 1499-508 (2013).

Liu, P., Chen, B., Mailler, R., & Wang Z-W. Antidromic-rectifying gap junctions amplify chemical transmission at functionally mixed electrical-chemical synapses. *Nature Communications* 8, 14814 (2017).

López-Cruz, A., Sordillo, A., Pokala, N., Liu, Q., et al. Parallel Multimodal Circuits Control an Innate Foraging Behavior. *Neuron* 102(2), 407-419 (2019).

Maricq, A. V., Peckol, E., Driscoll, M., & Bargmann, C. I. Mechanosensory signalling in *C. elegans* mediated by the GLR-1 glutamate receptor. *Nature* 378, 78-81 (1995).

Miesenböck, G., De Angelis, D. A., & Rothman, J. E. Visualizing secretion and synaptic transmission with pH-sensitive green fluorescent proteins. *Nature* 394, 192-5 (1998).

Mingote, S., Chuhma, N., Kalmbach, A., et al. Dopamine neuron dependent behaviors mediated by glutamate cotransmission. *Elife* 6, e27566 (2017).

Ohnishi, N., Kuhara, A., Nakamura, F., Okochi, Y., & Mori, I. Bidirectional regulation of thermotaxis by glutamate transmissions in *Caenorhabditis elegans*. *EMBO J.* 30(7), 1376-88 (2011).

Ölveczky, B. P., Andalman, A. S., & Fee, M. S. Vocal Experimentation in the Juvenile Songbird Requires a Basal Ganglia Circuit. *PLoS Biol* 3(5), e153 (2005).

Onoa, B., Li, H., Gagnon-Bartsch, J. A., Elias, L. A., & Edwards, R. H. Vesicular monoamine and glutamate transporters select distinct synaptic vesicle recycling pathways. *J Neurosci.* 30(23), 7917-27 (2010).

Oshima, A., Tani, K., & Fujiyoshi, Y. Atomic structure of the innexin-6 gap junction channel determined by cryo-EM. *Nat Commun.* 7, 13681 (2016).

Pan, P-Y. & Ryan, T. A. Looser coupling of calcium entry and exocytosis in mid-brain dopamine neurons allows Calbindin to control release probability. *Nat Neurosci.* 15(6), 813–815 (2012).

Park, E. C., & Horvitz, H. R. Mutations with dominant effects on the behavior and morphology of the nematode *Caenorhabditis elegans*. *Genetics* 113(4), 821-52 (1986).

Pereda, A. E., Curti, S., Hoge, G., et al., Gap junction – mediated electrical transmission: regulatory mechanisms and plasticity. *Biochim Biophys Acta*. 1828(1), 134-146, (2013).

Pereira, L., Kratsios, P., Serrano-Saiz, E., et al. A cellular and regulatory map of the cholinergic nervous system of *C. elegans*. *Elife* 4, e12432 (2015).

Pierce-Shimomura, J. T., Morse, T. M. & Lockery, S. R. The fundamental role of pirouettes in *Caenorhabditis elegans* chemotaxis. *J. Neurosci.* 19, 9557–69 (1999).

Piggott, B. J., Liu, J., Feng, Z., Wescott, S. A., & Xu, X. Z. The neural circuits and synaptic mechanisms underlying motor initiation in *C. elegans*. *Cell* 147(4), 922-33 (2011).

Pirri, J. K., McPherson, A. D., Donnelly, J. L., Francis, M. M., & Alkema, M. J. A tyramine-gated chloride channel coordinates distinct motor programs of a *Caenorhabditis elegans* escape response. *Neuron* 62(4), 526-38 (2009).

Pokala, N., Liu, Q., Gordus, A., & Bargmann, C. I. Inducible and titratable silencing of *Caenorhabditis elegans* neurons in vivo with histamine-gated chloride channels. *Proc Natl Acad Sci U S A* 111(7), 2770-5 (2014).

Ranken, C. H., & Wicks, S. R. Mutations of the *Caenorhabditis elegans* brain-specific inorganic phosphate transporter eat-4 affect habituation of the tap-withdrawal response without affecting the response itself. *J Neurosci.* 20(11), 4337-44 (2000).

Sawin, E. R., Ranganathan, R., Horvitz, H. R. *C. elegans* locomotory rate is modulated by the environment through a dopaminergic pathway and by experience through a serotonergic pathway. *Neuron* 26(3), 619-31 (2000).

Seo, C., Guru, A., Jin, M. et al. Intense threat switches dorsal raphe serotonin neurons to a paradoxical operational mode. *Science* 363(6426), 538-542 (2019)

Serrano-Saiz, E., Poole, R. J., Felton, T., et al. Modular control of glutamatergic neuronal identity in *C. elegans* by distinct homeodomain proteins. *Cell* 155, 659-673 (2013).

Serrano-Saiz, E., Pereira, L., Gendrel, M., et al. A Neurotransmitter Atlas of the *Caenorhabditis elegans* Male Nervous System Reveals Sexually Dimorphic Neurotransmitter Usage. *Genetics* 206(3),1251-1269 (2017).



Silm, K., Yang, J., Marcott, P. F., et al., Synaptic Vesicle Recycling Pathway Determines Neurotransmitter Content and Release Properties. *Neuron* 102(4), 786-800 (2019).

Sherer, L. M., Catudio Garrett, E., Morgan, H. R. et al. Octopamine neuron dependent aggression requires dVGLUT from dual-transmitting neurons. *PLOS Genetics* 16(2), e1008609 (2020).

Schiavo, G., Benfenati, F., Poulain, B. et al. Tetanus and botulinum-B neurotoxins block neurotransmitter release by proteolytic cleavage of synaptobrevin. *Nature* 359(6398), 832-5 (1992).

Shtonda, B. B. & Avery, L. Dietary choice behavior in *Caenorhabditis elegans*. *J Exp Biol.* 209, 89-102 (2006).

Smith, M. & Pereda, A. E. Chemical synaptic activity modulates nearby electrical synapses. *PNAS* 100(8), 4849-4854 (2003).

Speese, S., Petrie, M., UNC-31 (CAPS) Is Required for Dense-Core Vesicle But Not Synaptic Vesicle Exocytosis in *Caenorhabditis elegans*. *J Neurosci.* 27(23), 6150-6162 (2017).

Steuer Costa, W., Van der Auwera, P., Glock, C. et al. A GABAergic and peptidergic sleep neuron as a locomotion stop neuron with compartmentalized Ca<sup>2+</sup> dynamics. *Nat Commun* 10, 4095 (2019).

Stephens, G. J., Johnson-Kerner, B., Bialek, W., & Ryu, W. S. Dimensionality and Dynamics in the Behavior of *C. elegans*. *PLoS Comput Biol* 4(4): e1000028.

Taylor, S. R., Santpere, G., Reilly, M. et al. Expression profiling of the mature *C. elegans* nervous system by single-cell RNA-Sequencing. *bioRxiv* 737577 (2019).

Thureson-Klein, A. Exocytosis from large and small dense cored vesicles in noradrenergic nerve terminals. *Neuroscience* 10(2), 245-259 (1983).

Trudeau, L. E., & El Mestikawy, S. Glutamate Cotransmission in Cholinergic, GABAergic and Monoamine Systems: Contrasts and Commonalities. *Front Neural Circuits* 12, 113 (2018).

Tsalik, E. L., & Hobert, O. Functional mapping of neurons that control locomotory behavior in *Caenorhabditis elegans*. *J Neurobiol.* 56(2), 178-97 (2003).

Turek, M., Lewandrowski, I., & Bringmann, H. An AP2 transcription factor is required for a sleep-active neuron to induce sleep-like quiescence in *C. elegans*. *Curr Biol.* 23(22), 2215-2223 (2013).

- Vaaga, C. E., Borisovka, M., & Westbrook, G. L. Dual-transmitter neurons: functional implications of co-release and co-transmission. *Curr Opin Neurobiol.* 29, 25-32 (2014).
- Ventimiglia, D. & Bargmann, C. I. Diverse modes of synaptic signaling, regulation, and plasticity distinguish two classes of *C. elegans* glutamatergic neurons. *Elife* 6, e31234 (2017).
- Wakabayashi, T., Kitagawa, I. & Shingai, R. Neurons regulating the duration of forward locomotion in *Caenorhabditis elegans*. *Neurosci. Res.* 50, 103–111 (2004).
- Wakabayashi, T., Sakata, K., Togashi, T. et al. Navigational choice between reversal and curve during acidic pH avoidance behavior in *Caenorhabditis elegans*. *BMC Neurosci* 16, 79 (2015).
- Waites, C. L., Mehta, A., Tan, P. K., et al. An Acidic Motif Retains Vesicular Monoamine Transporter 2 on Large Dense Core Vesicles. *J Cell Biol.* 52(6), 1159–1168 (2001).
- Wittenburg, N. & Baumeister, R. Thermal avoidance in *Caenorhabditis elegans*: An approach to the study of nociception. *Proc Natl Acad Sci U S A.* 96(18), 10477–10482. (1999).
- White, J. G., Southgate, E., Thomson, J. & Brenner, S. The structure of the nervous system of the nematode *Caenorhabditis elegans*. *Philos. Trans. R. Soc. B* 314,1–340 (1986).
- Whittaker, V.,P, Dowdall M., J., & Boyne, A., F. The storage and release of acetylcholine by cholinergic nerve terminals: recent results with non-mammalian preparations. *Biochem Soc Symp* 36, 49-68 (1972).
- Womelsdorf, T., Fries, P., Mitra, P. P., & Desimone, R. Gamma-band synchronization in visual cortex predicts speed of change detection. *Nature* 439(7077), 733-6 (2006).
- Wragg, R. T., Hapiak, V., Miller, S. B., et al. Tyramine and octopamine independently inhibit serotonin-stimulated aversive behaviors in *Caenorhabditis elegans* through two novel amine receptors. *J Neurosci.* 27(49), 13402-12 (2007).
- Wu, H. G., Miyamoto, Y. R., Gonzalez Castro, L. N., Ölveckzy, B. P., & Smith, M. A. Temporal structure of motor variability is dynamically regulated and predicts motor learning ability. *Nat Neurosci.* 17(2), 312–321 (2014).
- Zhang, M., Wang, X., & Goldberg, M. E. A spatially nonselective baseline signal in parietal cortex reflects the probability of a monkey's success on the current trial. *Proc Natl Acad Sci U S A* 111(24), 8967-72 (2014).

Zhao, B., Khare, P., Feldman, L., & Dent, J. A. Reversal frequency in *Caenorhabditis elegans* represents an integrated response to the state of the animal and its environment. *J Neurosci.* 23(12), 5319-28 (2003).

Zou, W., Fu, J., Zhang, H., et al. Decoding the intensity of sensory input by two glutamate receptors in one *C. elegans* interneuron. *Nat Commun.* 9(1), 4311 (2018).